Alma Mater Studiorum - University of Bologna

DEIS - DEPARTMENT OF ELECTRONICS, COMPUTER SCIENCE AND SYSTEMS

PhD Course in Electronics, Computer Science and Telecommunications

Cycle XXIII - ING-INF/01

Parallel Modeling of the Electric Field Distribution in the Brain

Candidate:
DE MARCO TOMMASO

Tutor:
Chiar.mo Prof. Ing. ROBERTO GUERRIERI

PhD Course Coordinator:
Chiar.mo Prof. Ing. PAOLA MELLO

Final Examination Year 2011

Abstract

The term "Brain Imaging" identifies a set of techniques to analyze the structure and/or functional behavior of the brain in normal and/or pathological situations. These techniques are largely used in the study of brain activity. In addition to clinical usage, analysis of brain activity is gaining popularity in others recent fields, i.e. Brain Computer Interfaces (BCI) and the study of cognitive processes. In this context, usage of classical solutions (e.g. fMRI, PET-CT) could be unfeasible, due to their low temporal resolution, high cost and limited portability. For these reasons alternative low cost techniques are object of research, typically based on simple recording hardware and on intensive data elaboration process. Typical examples are ElectroEncephaloGraphy (EEG) and Electrical Impedance Tomography (EIT), where electric potential at the patient's scalp is recorded by high impedance electrodes. In EEG potentials are directly generated from neuronal activity, while in EIT by the injection of small currents at the scalp.
To retrieve meaningful insights on brain activity from measurements, EIT and EEG relies on detailed knowledge of the underlying electrical properties of the body. This is obtained from numerical models of the electric field distribution therein. The inhomogeneous and anisotropic electric properties of human tissues make accurate modeling and simulation very challenging, leading to a tradeoff between physical accuracy and technical feasibility, which currently severely limits the capabilities of these techniques. Moreover elaboration of data recorded requires usage of regularization techniques computationally intensive, which influences the application with heavy temporal constraints (such as BCI).
This work focuses on the parallel implementation of a work-flow for EEG and EIT data processing. The resulting software is accelerated using multi-core GPUs, in order to provide solution in reasonable times and address requirements of real-time BCI systems, without over-simplifying the complexity and accuracy of the head models.

List of abbreviations

BCI	Brain Computer Interface
BEM	Boundary Elements Method
BiCG	BiConiugate Gradient Method
CSF	CerebroSpinal Fluid
CSI	Central Nervous System Imaging
CT	Computerized Tomography
CUDA	Compute Unified Device Architecture
DP	Double Precision unit
DTI/DTMRI	Diffusion Tensor MRI
EEG	ElectroEncephaloGraphy
EIT	Electrical Impedance Tomography
EPSP	Excitatory Post-Synaptic Potential
ERP	Event Related Voltage Potential
FA	Fractional Anisotropy
FDM	Finite Difference Method
FEM	Finite Elements Method
fMRI	Functional Magnetic Resonance Images
FOCUSS	FOCal Undetermined System Solver
FPS	Frames Per Second
FVM	Finite Volume Method
GPU	Graphical Processing Unit
GM	Gray matter
IPSP	Inhibitory Post-Synaptic Potential
ISA	Isolated Skull Approach
LORETA	Low-resolution electromagnetic tomography
LSQR	Least SQuared Residuals Method

LU	Lower-Upper triangular matrix factorization
MN	Minimum Norm
MRI	Magnetic Resonance Images
PC	Personal Computer
PET	Positron Emission Tomography
PSP	Post-Synaptic Stimuli
SFU	Special Function Unit
SIMD	Single Instruction Multiple Data
SIMT	Single Instruction Multiple Threads
sLORETA	Standardized Low-resolution electromagnetic tomography
SM	Streaming Multiprocessor
SP	Stream Processors
SSLOFO	Standardized Shrinking LORETA-FOCUSS
T	Tesla
TFLOP	Tera floating point operations
TMI	Triangular Matrix Inversion
TPC	Texture Processing Clusters
WM	White matter
WMN	Weighted Minimum Norm

Contents

List of Figures

List of Tables

Introduction

The term "Brain Imaging" identifies a set of techniques to analyze the structure and/or functional behavior of the brain in normal and/or pathological situations. The neuro-biological analysis of cognitive processes indicates that even the most complex functions of the brain are localized to specific combinations of regions. Localization has great clinical importance and explains why certain syndromes are characteristic of diseases in specific regions of the brain, making brain imaging a powerful instrument for the diagnosis and treatment of central nervous system diseases, and in general, in the study of brain activity and in patients' monitoring. Analysis of brain activity it is gaining popularity in others recent fields, i.e. Brain Computer Interfaces (BCI) and the study of cognitive processes. BCIs are communication systems interfacing human brain with external devices, e.g. computers or actuators, where user's commands are evaluated starting from the analysis of the estimated brain activity of the subject. The study of cognitive processes is instead based on applying external stimuli to the patients, which could be of visual, auditory or somatosensory nature, and analyze the corresponding brain activity response.

In this context, usage of classical brain imaging solutions based on the application of magnetic fields (e.g. fMRI) or nuclear medicine (e.g. PET-CT) could be unfeasible. Although they are able to provide brain activity images with high spatial resolution, they suffer from low temporal resolution, which is of primary importance in BCI systems. Other disadvantages are their great area occupation and intrinsic high costs, which practically make them a prerogative of hospitals and advanced research centers. This limits their usage in BCI or monitoring systems where hardware portability and high temporal resolution are required, and a certain level of freedom of moving has to be guaranteed to the patient, especially for long period data acquisition. Collateral effects due to strong magnetic fields or X-ray exposure involved make impossible their usage for continuous monitoring of the patients.

For these reasons alternative low cost techniques are object of research, typically based on simple recording hardware (e.g. from data collected from high impedance extra cranial electrodes) and on intensive data elaboration process. Typical examples are ElectroEncephaloGraphy (EEG) and Electrical Impedance Tomography (EIT). In EEG voltage distribution on the subject's scalp generated by brain electrical activity is recorded by passive high impedance electrodes; data acquired are elaborated to provide an estimate of the active area inside the brain. In EIT a set of electrodes injects small currents on the subject's scalp and the resulting voltage distribution is recorded by a second set of high impedance electrodes; data acquired are elaborated to provide an estimate of the impedance distribution inside the head. Both in EEG and EIT, in contrast with the relative simplicity of the acquisition hardware, data elaboration demands for heavy computational load. First of all, it is necessary to obtain a numerical model of subject head; considering head tissues as a non-homogeneous conductive medium, this is equivalent to solve the Poisson' s equation for the potential inside it (the so-called *Forward Problem*). Due to the complexity of the domain, analytical solutions are not feasible, and one needs to rely on numerical solvers. Finding a numerical solution is a heavy computational task due to the need to provide anatomically sound models. The complexity of the numerical solution is a function of the spatial resolution of the model and the ability to capture non-ideal behavior such as tissue non-uniformity, complex anisotropic conductivity distribution and realistic electrode models able to take into account electrical effects given by the contact between skin and electrodes plates. The availability of an accurate, fast and reliable forward problem simulation tool is mandatory to be able to design and configure at best the acquisition instrumentation, maximizing the amount of information detectable during usage. Furthermore, electrodes data elaboration results to be an under-determined problem (the so-called *Inverse Problem*), where complex brain activation maps (conductivity distribution for EIT) need to be evaluated from measures on a relatively few points, moreover performed at the scalp surface. This problem is addressed by taking into account a-priori informations with appropriate regularization techniques. However, the spatial resolution results to be lower than classical solution like fMRI.
EEG and EIT are therefore a class of Brian Imaging techniques complementary to classical solution, providing high temporal resolution with low-cost and portable acquisition hardware at the cost of a lower spatial resolution. Algorithmic work-flow results in an heavy computational task, whose performances influence the accuracy and complexity of the numerical model and their application to environments with heavy temporal constraints, like *real-time* elaboration in BCI. Given this trade-off between complexity and

accuracy, state of the art models often rely on simplifications and/or sacrifice spatial resolution to reduce the complexity and therefore, the solution time, to acceptable levels. These challenges can be solved using multi-core computing platform; advances in scientific computing in fact have led to the development of high performances and low cost architectures, which can be successfully applied to the introduced computational intensive problems. An example is represented by Graphical Processing Unit (GPU), multi-core graphic cards programmable by the user which allow to obtain high performance supercomputing with standard low cost desktop PCs.

This work focuses on the parallel implementation of a work-flow for EEG and EIT data processing. The resulting software is accelerated using NVIDIA® multi-core GPUs, in order to provide solution in reasonable times and address requirements of real-time BCI systems, without introducing simplification in the complexity and accuracy of the head models.
This work is organized as follows: in Chapter 1 the most diffused Brain Imaging techniques are presented, focusing on their field of application and on the bio-electrical nature of neuronal activity which is at the base of EEG recording. Chapter 2 presents the developed EEG algorithmic work-flow, focusing on the *Inverse Problem* solution with the usage of regularization techniques to obtain high quality images. In Chapter 3 the developed EIT algorithmic work-flow is presented, focusing on the formulation of an high resolution head model based on a Finite Volumes Formulation. In Chapter 4 the implementation of some crucial EIT and EEG computational kernels on GPU is presented, focusing on the performances obtained. Then results are discussed in Chapter 5, and achieved conclusions are presented.

The main activity in this work has been carried out in the context of the *Central Nervous System Imaging* project (CSI). This is an ENIAC (European Nanoelectronics Initiative Advisory Council) project aiming "to achieve substantial advances in state-of-the-art medical 3D-imaging platforms by focusing on the diagnosis and therapy of serious diseases of the central nervous system and brain".

Chapter 1

Brain Imaging: Methods and Applications

Brain Imaging comprises a set of techniques to analyze the structural or functional behavior of the brain in normal or pathological situations. Neurobiological analysis of cognitive processes indicates that even the most complex functions of the brain are localized at specific regional patterns. Localization has great clinical importance as it explains why certain syndromes are characteristic of disease in specific regions of the brain [1]. This makes brain imaging a powerful tool in diagnosis and treatment of central nervous system diseases and general study of brain activity.
In this scope, it is important to highlight that while classical solutions (e.g. fMRI) are reserved to hospitals and advanced research centers because of their high cost and large size, alternative low cost techniques are subject to research. These are typically based on simple recording hardware (e.g. high impedance extra cranial electrodes), but a compute intensive data elaboration process. However, advances in scientific computing have led to development of architectures featuring high performance at low cost, which can be used in different research fields and applications. A typical example is the Graphic Processing Units (GPUs) [2], a programmable multi-core architecture which allows high performance computing in a standard low cost desktop pc, as will be shown in Chapter 4.
In brain imaging, this computational power allows the development of alternative techniques where the reduced complexity and size of the acquisition system is balanced by compute intensive data processing, also within *real time* constraints. A typical example of this trend is the recent development in the field of *Brain-Computer Interfaces* (BCI), which interpret human brain activity from real-time measurements picked up by portable recording hardware (Chapter 1.2.3).

1.1 Brain imaging techniques overview

In the scope of this discussion, brain imaging techniques can be classified in two different groups: electromagnetic-based and biopotential-based solutions. These two groups are very different in the complexity of the acquisition hardware:

- electromagnetic-based solutions, also known as anatomical imaging techniques, rely on the application of strong electromagnetic fields or X-ray emissions to the patient's head, and the measurement of changes in the field distribution given by the presence of head tissues,
- biopotential-based solutions rely on measurements of electric potentials at the surface of the head by non-invasive electrodes.

Obviously, first solutions have a great impact in terms of cost and area occupation than the second one, which instead require a relatively simple acquisition hardware (high impedance electrodes). However, biopotential solutions require computationally intensive post-processing and elaboration of acquired data, which require a high-performance computing platform.
Electromagnetic-based techniques provide images with very high spatial resolution, defined by the size of the smallest detectable volume (the so-called *voxel*); each *voxel* corresponds directly to each pixel of the resulting images. In contrast, they suffer of a low temporal resolution which restricts traditional systems to static images. More advanced electromagnetic techniques, like fMRI, are able to achieve higher temporal resolution, but its usage remains limited to hospital environments. What is more, the strength of the magnetic fields involved during an fMRI acquisition does not allow continuous monitoring of the patient. This however is necessary in the treatment of pathologies like epilepsy, where occurrence of attacks is often unknown. In these cases, biopotential solutions are preferred because they are able to capture signals with resolution also higher than 1 MHz, without particular limitations on the acquisition period.
These aspects make biopotential-based brain imaging a reasonable choice for the development of biomedical solutions which are not only referred to the diagnosis and/or study of brain pathologies but also to the realization of more complex interactions between the patient and external hardware, like Brain Computer Interfaces.

1.1.1 Electromagnetic-based solutions

The first three-dimensional brain imaging techniques were the *X-ray computerized tomography* (CT scanning) and the *magnetic resonance imaging*

(MRI), invented in the 1970s and 1980s respectively. These techniques are still used as diagnostic methods because they provide an high spatial resolution; a modern MRI provides images composed of pixels (*voxels*) of $1mm^3$. The level of detail achieved by these techniques make them an optimal choice for morphological description of head tissues; moreover they also allow identification of internal lesions and malformations. However, they are able to provide only static images and their usage is limited in specific centers for the high costs.

CT scanning is based on the electro-magnetic properties of the tissues. A X-ray tube which emits beams of X-ray is placed around the head and rotates around it. A set of X-ray detectors are placed on the opposite side such that they can capture the resulting electromagnetic field, which is influenced by the structures and the densities of the pervaded head tissues. Data detected are then elaborated using mathematical models in order to obtain a three dimensional reconstruction of the subject's head.

MRI scanning is based on application of strong variable magnetic fields to the subject's head. The basics of this technique are now quickly described. Normally, at each proton there is a small magnetic field produced by its rotation around a random axis which differs from each one. Consequently, the total magnetic field is zero. A first constant magnetic field is applied to the subject, which forces all the protons to align their axes with the direction of the magnetic field. This causes the generation of a "physiological" field, which can be detected by the MRI instrumentation. After this, a second magnetic field consisting of radio frequency pulses is applied. This is because nuclei of certain atoms, for example hydrogen ones (protons), can be made to resonate if a radio frequency pulse is applied to them in a magnetic field. This process consists in a wobbling of the proton around its axes (*precession*). When the pulses are turned off, protons stop wobbling and return in the original position with a relaxation process defined by two time constants, T1 and T2, which are finally measured by the MRI instrumentation. In particular, magnetic behavior of protons (and consequently the variations induced by them) differs according to the belonging tissue; for example protons in fat behave differently from protons in water. In addition, the relaxation process (T1 and T2) differs depending on the belonging tissue (fat or water), and whether water is intracellular or extracellular, in the blood, or in cerebral spinal fluid. The collected data are organized in 3D images where luminosity levels represent the parameters measured (typically T1 or T2).
Magnetic resonance imaging is also capable of localizing activity in the three-dimensional volume of the brain. This is achieved using gradient-magnetic

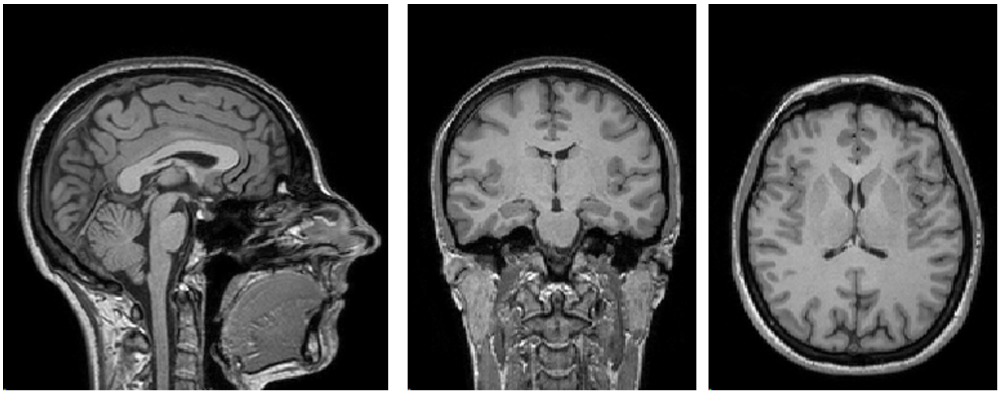

Figure 1.1: *MRI slices of the head obtained along different directions of space; each slice represents an ideal plane intersecting the head in a sagittal, coronal and horizontal direction respectively.*

fields where the strength of the field changes gradually along an axis. Applying gradients along three axes subdivides the tissue: one magnetic gradient is used to excite a single "slice" of the subject's head, two more gradients subdivide that slice into rows and columns, as shown in fig. 1.1.
Besides the very low temporal resolutions of this technique, MRI images have a very high spatial resolution; a modern MRI achieves voxel resolutions of 1mm^3 generating magnetic fields of 3 T, but there are studies that aim to use fields up to 7 T [3] and 9.4 T on human subjects, which would allow resolutions better than 0.05mm^3 [4].

Others brain imaging techniques are based on magnetic resonance, like MRI. One of these is the **Diffusion Tensor MRI** (DTI), which allows to obtain images representing the diffusion coefficient of water in the tissues. In particular, DTI images allow to detect and map the fibrous structure of the tissues, which it is particularly relevant for example for brain white matter or in the mapping of the connectivity between neurons [5].

Functional MRI (fMRI) instead allow to obtain functional imaging of the brain maintaining the high spatial resolution typical of the electro-magnetic techniques. This is based on the same principles of static MRI, but it is able to detect variations of oxygen concentration in the blood. When neurons are activated, the supply of blood to the active region increases. For reasons that are still unclear, the delivery of oxygenated hemoglobin to the region is greater than local oxygen consumption, resulting in a greater proportion of

oxygenated to deoxygenated hemoglobin, which causes a local variation of the magnetic properties that can be detected with the MRI process previously described. *f*MRI is so be used to examine the activation of the brain regions during cognitive tasks, but with a temporal resolution less than 1Hz [6].

1.1.2 Biopotential-based solutions

Recording of the electric voltages on the scalp with passive electrodes is a procedure used in medicine in the first decades of 1900. Recorded signals are plotted on a standard chart (*electroencephalogram*) as shown on fig. 1.2 and visually examined by the physicians. Moreover, in the last years al-

Figure 1.2: *Electroencephalogram. Each traces is the temporal trend of the voltage recorded at each electrode.*[1]

gorithmic solutions to elaborate data recorded by the electrodes have been presented, with the goal to provide brain imaging techniques avoiding the high cost of electromagnetic-based solutions. This trend is supported by the development of more capable computer architectures in the last years, thus providing the computational resources necessary to compute brain activity

[1]Source: `http://www2.massgeneral.org/childhoodepilepsy/medical/diagnosis-popup_general.htm`

maps from recorded electrode potentials.
Biopotential-based solutions are able to achieve high temporal resolution, but on the downside they suffer from poorer spatial resolution than MRI images. This is essentially owed to the electrical properties of the skull, which is acting as a barrier for propagation of the electric field. Despite this, biopotential solutions remain interesting since they can be used in different contexts for their relative low costs and "simplicity" of the acquisition hardware. However, they are also applicable in medical routines when high temporal resolution is necessary (eventually coupled with MRI analysis) like in patient monitoring, avoiding the limitations on acquisition times and side effects of a standard fMRI.

Electroencephalography (EEG) is a brain imaging techniques based on recordings of potential differences on the scalp using passive electrodes. These potentials originate from the activity of the neurons in the gray matter (cerebral cortex), causing an electric field to propagate to the scalp. As previously introduced, electric field propagation is limited by the electrical properties of skull, resulting in potential differences on the scalp of only few μV [7] which limit the spatial resolution of the method.

Electrical Impedance Tomography (EIT) is based on injection of small currents (less than 1 mA at frequency starting from 1 KHz) at the scalp surface using active electrodes, as illustrated in fig. 1.3. A set of passive electrodes measures the potential differences caused by the induced electric fields. Data detected are then elaborated in order to obtain an impedance distribution map on the brain, which indicates the presence of particular pathologies like epileptic foci, local ischemia and lesions [8].

Both EEG and EIT require computationally heavy data processing. To begin with, computational work-flow can be divided in two separate problems. The first is the so-called *Forward Problem*, which requires the definition and computation of a mathematical model that describes the morphology and electrical properties of target head volume. In particular, the Forward Problem defines the relationship between sources of the electric field in the head volume (neural activity for EEG, current injections for EIT) and the voltages measured by the scalp electrodes. This task has to consider both the morphology and electrical properties of the most relevant head tissues (scalp, skull, white matter, gray matter, CSF) and the perturbations introduced by the electrodes. It results into a large linear system whose solution requires long computation times; for example in EIT Borsic et al. pointed out that the solution to the forward problem accounts for 95% of the total EIT com-

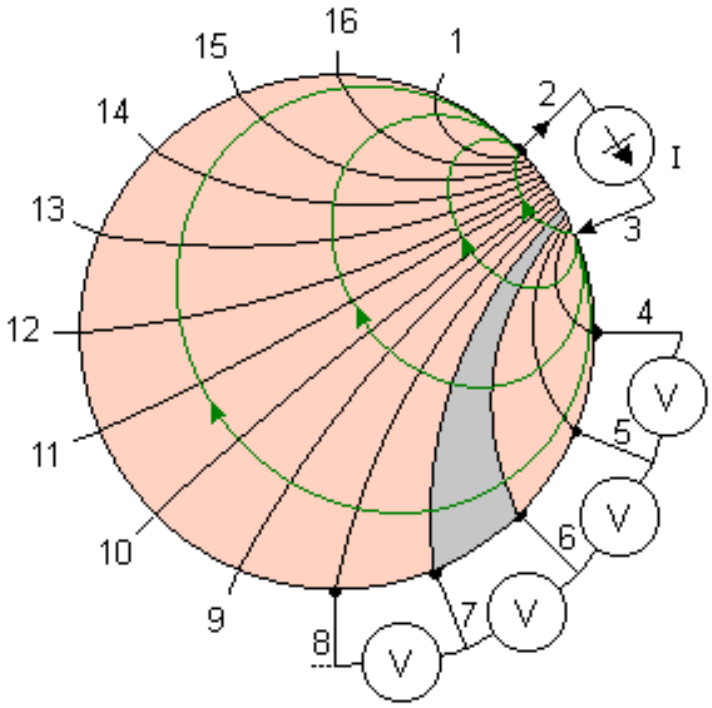

Figure 1.3: *In EIT small currents are injected in the target volume by active electrodes (2,3); potential differences at the surface are measured by passive electrodes. Then data are elaborated to reconstruct the impedance distribution inside the volume.*[2]

putation cost [9].

The successive step, the so-called *Inverse Problem*, comprises the estimation of the electric source distribution and/or local parameter variations according to the measured data from the electrodes and the electric model of the system provided by the Forward Problem. This problem is often ill-posed, making it necessary to constraint the solution space with *a-priori* information and/or iterative refinement.
More details about the computational issues of EEG and EIT work-flow will be explained in the following chapters.

1.2 Applications

Brain imaging is a research field with possible applications in many areas. To date, intensive usage is found in clinical praxis for diagnosis of brain disorders,

[2]Source: [10]

but also in research centers studying brain functionality and non-muscular control of external devices.

1.2.1 Brain pathologies

At the moment, electromagnetic solutions are widely used in medicine while biopotential based solutions are still subject of study. EEG imaging is just used in the diagnosis of particular pathologies, like detection and localization of epileptic foci [11]. In case of intractable epilepsy, surgery is required to remove the affected portion(s) of the brain. Consequently, continuous monitoring and analysis using brain imaging techniques (typically EEG) is necessary in order to accurately identify the area to extract. This can be combined with invasive procedures, like surgical implant of intra-cranial electrodes in the subject brain. However, other brain imaging techniques (as the EIT) able to improve localization performance of EEG could help to avoid this invasive treatment. For this purpose, several studies show how EIT could theoretically be used to detect epileptic foci, and others pathologies like brain lesions and local ischemia [8][12][13].

1.2.2 Cognitive processes

As well as for diagnosis and treatment of pathology, brain imaging is also used for study of the brain functionality. In particular, being EEG non-invasive and painless, it is used to study cognitive processes of the brain, e.g. memory, attention and perception. These studies are based on identification of Event Related Voltage Potentials (ERPs) in neural activity [14]. ERPs are voltage variations induced in the subject's brain by external stimuli, and are used to detect brain regions involved in different cognitive tasks (attention, memory, language processing). ERPs dynamics are not detectable by standard fMRI, so EEG is preferred for its higher temporal resolution.

1.2.3 Brain Computer Interfaces

A Brain Computer Interface (BCI) is a communication system interfacing the human brain to external devices, like computers or actuators. User commands are formed by recognizing brain activity with brain imaging techniques, typically EEG or invasive electrodes surgically positioned on the cerebral cortex. BCIs are often designed to assist, augment or repair human cognitive or sensory-motor functions; particular attention is paid to the

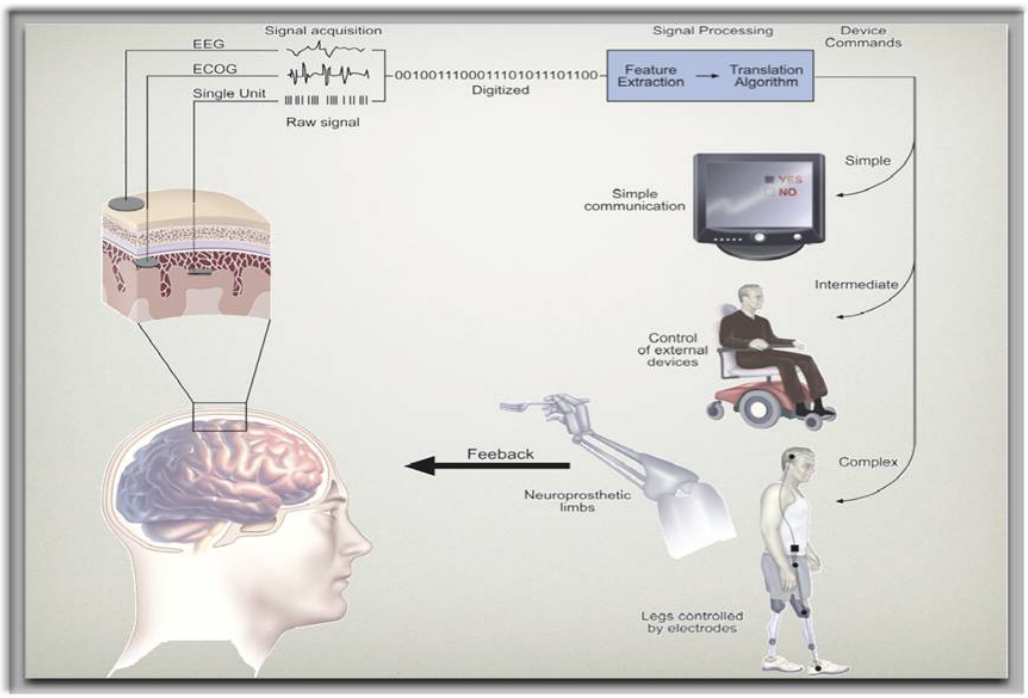

Figure 1.4: *BCI neurofeedback. Voltages measured by electrodes are sent to a computer. Data are interpreted to compute actuators commands. Feedback is closed by the subject's perception of actuator actions or movements.*[3]

the realization of prostheses controlled by BCI in order to replace damaged human functions like hearing, sight and movement (fig. 1.4).

1.3 The physics of brain activity

In this section, an overview of brain cells is presented, focused on the electrical aspects related to brain activity. Electrical aspects of brain activity are directly connected only with EEG brain imaging, but a preliminary overview about the brain cells is necessary to understand the contents of this work. Unlike EEG, the gross of brain imaging methods relies on the analysis of phenomenas connected with brain activity and not with the activity itself: for example fMRI is based on recording variations of oxygen concentration in blood, EIT on the other hand detects impedance variations related to brain activity.

[3]Source: `http://www.etsu.edu/cas/bcilab/pictures/Leuthardt.jpg`

1.3.1 Neurons and glial cells

Cells found in the human brain can be classified into two main groups:

- neurons (or nerve cells), of which there are about 10^{10} in a normal human brain,
- glial cells, of which there are typically 10-50 times more than neurons.

Glial cells surround the cell bodies, axons, and dendrites of neurons. As far as it is known, glia are not directly involved in information processing, but they are responsible for other physiological functions, such as production of myelin used for electrical insulation of neuron axons [1].
Neurons are cells responsible for cognitive functionalities like perception, though, language etc. They are electrically excitable and connected together in a complex network. Neurons are located in the brain external layers (gray matter), in the cerebellum and in the most internal brain regions.
Different types of neurons exists and their structure can be described in three main parts (fig. 1.5):

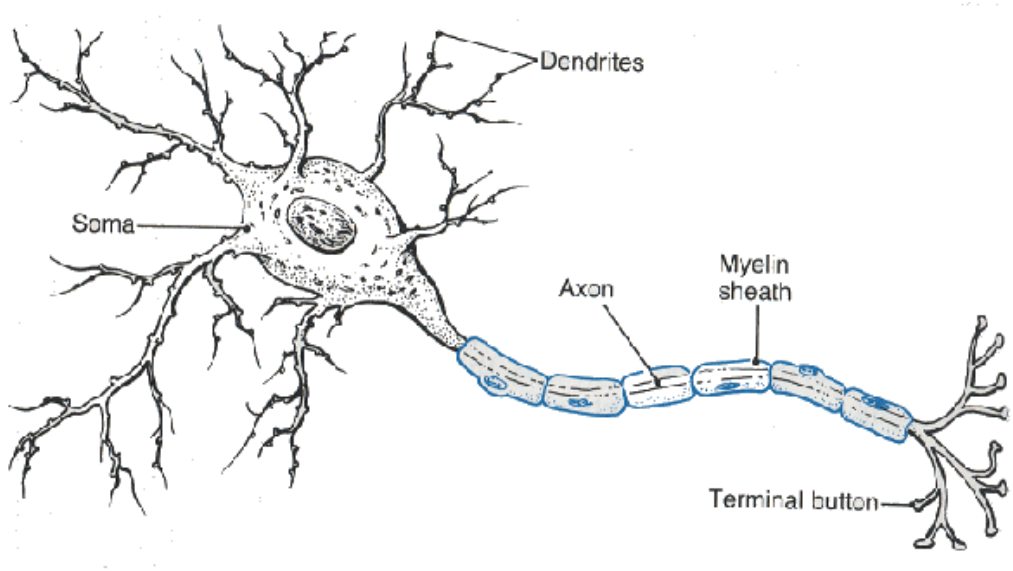

Figure 1.5: *The neuron structure is composed of soma, dendrites and axon. Glial cells electrically insulate the axon.*[4]

[4]Source: `http://www2.cedarcrest.edu/academic/bio/hale/bioT_EID/lectures/tetanus-neuron.gif`

1. the cell body, also called *soma*, which contain the nucleus;
2. numerous short processes, called *dendrites*, which connect the soma with other neurons and receive electrical stimuli. From an electrical point of view, these are the input ports of the cell (a cortical neuron can receive impulse from ten to hundred thousands neurons [7]);
3. the axon, a single long nerve where electrical impulses generated by the neuron are propagated towards others neurons (or muscles). Electrically it can be considered as a transmission wire [15].

Connections with the others cells are provided by particular terminal structures at the end of the axon (*synapses*), which convert electrical information into a chemical signal, which is sent to the connected neurons dendrites. Equivalently, synapses are also located on the dendrites, which receive chemical signals and convert them into electrical signals. This process relies on particular molecules, called *neurotransmitters*.

1.3.2 Neuronal electrical activity: the membrane potential

The neuron's task is to receive signals, process them and transmit resulting signals. Signals received by the dendrites can be of two different types: *excitatory*, which favor activation of the neuron, and *inhibitory*, which compromises activation [16].
At rest condition, electrical configuration of the neuron is characterized by a potential difference of about -70 mV between the intracellular and extracellular fluid [10]. This is due to the action of the cell membrane, which is able to maintain a different concentration of charged ionic concentration across it. As shown in fig. 1.6, the neuron's membrane consists of a double impermeable phospholipid layer of macromolecoles (*ionic channels*) able to alternatively enable or disable ionic flux across the membrane. This *selective permeability* allow the neuron to maintain a disequilibrium of ionic concentration between intra- and extracellular space, resulting in the aforementioned rest potential. When a neuron passes into active state, the ionic channel activation pattern changes, leading to a massive passage of ions equalizing ionic concentration. This causes a potential depolarization (potential difference at membrane decrease to -40 mV) which travels along the axon as an impulse. This depolarization is also referred to as excitatory post-synaptic potential (EPSP).
On the other hand, when an active neuron receives inhibitory stimuli, a different ionic channel activation pattern leads to changes in the ionic concentra-

tion that result in a hyperpolarization, which increases membrane potential difference. This potential change is also called an inhibitory post-synaptic potential (IPSP).

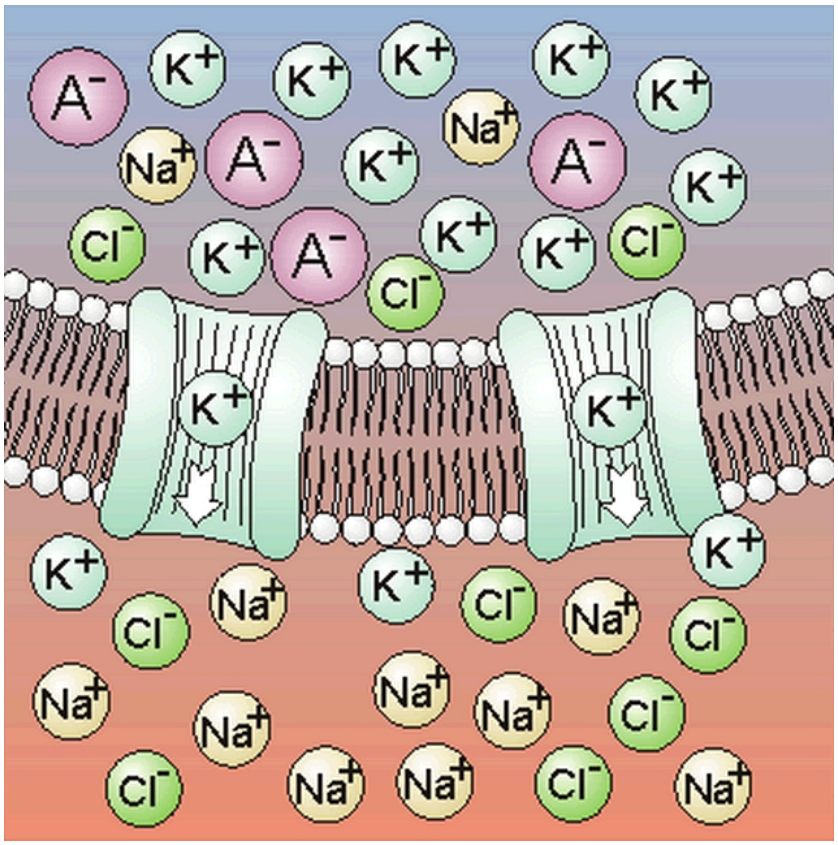

Figure 1.6: *Patch of neuronal membrane in rest state. Different concentrations of positive and negative ions lead to a stable potential difference. The situation is maintained by the closure of ionic channels. In case of neuron activation, channels open allowing passage of positive ions, resulting in voltage depolarization.*[5]

[5]Source: [10]

Chapter 2

EEG Source Imaging

Electroencephalography (EEG) is a monitoring technique commonly applied in neuroscience research and clinical routine to explore human brain behavior. EEG is based on the measurement and mapping of electrical activity produced by the brain as it is being recorded by electrodes placed on the scalp. The recorded data then are plotted into a standard chart (*electroencephalogram*) and (visually) examined by the physicians.
However, in the past years brain imaging techniques have been presented based on the elaboration of data recorded by EEG, in order to avoid high costs of electromagnetic-based solutions, e.i. fMRI. Aim of this new field of application, known as EEG source imaging, is to provide functional images of neuronal activity in the human cerebral cortex (gray matter), in particular for the localization of active areas at each time-frame (*source localization*).
As for EIT, EEG source imaging is characterized by an acquisition hardware, which is relatively simple and portable (high impedance electrodes) and by an intensive task of post-processing of acquired data (*EEG inverse problem*). This introduces severe computation requirements, which could limit the high temporal resolution provided by the measurement instrumentation. Difficulties arise particularly when the problem needs to be solved under real-time constraints, as required by modern BCI applications.
To retrieve meaningful insights from these measurements, EEG brain imaging relies on detailed knowledge of the morphology of the subject head volume, which determines the scalp voltage distribution due to brain activity. This is obtained from numerical models of the electric field propagation in the head, whose computation is very time-consuming and computationally intensive (*EEG forward problem*).
In this Chapter, EEG computational issues are being presented and discussed, showing the benefits introduced by multi-core computing devices in the computation of subject specific EEG forward model, and in the EEG

inverse problem computation under real-time constraints.

2.1 Physiological nature of EEG

As introduced in Chapter 1.3, EEG brain imaging is a technique based on the estimation of cerebral activity, starting from the recording of potentials directly generated by neuronal activity. For this reason, a short overview of the physiological nature of EEG is outlined in the following paragraph.

2.1.1 Neuronal activity

Neurons are electrically excitable cells, whose activity consists essentially in the switching between two states (Chapter 1.3.2):

- a rest state, where neurons are in a stationary electrical condition characterized by a constant potential difference across its cellular membrane given by different ion concentration,

- an active state, where neuron transmit along its axon impulses (*action potentials*) at a particular frequency (*firing rate*) exploiting a precise activation pattern for the ionic channels aimed to balance ionic disequilibrium across the membrane.

When in an active state, the instigated behavior causes an electric field, propagating in the surrounding (conductive) medium, that is supported by an extracellular current density flowing between the axon extremities. Electric field generated results in a potential distribution through the head, which can be theoretically recorded by passive electrodes placed on the scalp. However the time course of the action potential is too short (0.3 ms) to be detected from EEG electrodes, although it can be large in amplitude (70-110 mV) [17][18].
Transition between the two states is due to the occurrence of post-synaptic stimuli (PSP). As introduced in Chapter 1.3.2, PSP are stimuli sent by connected neurons at the dendrites; they flow towards the soma and along the axon, eventually determining a change of the neuron state. Differently from active potentials, PSP have a large time course (10-20 ms), although a lower amplitude (0.1-10 mV), which make them detectable by EEG electrodes [16].

2.1.2 Limits of electric field detection from the scalp: the pyramidal cells

In reality, the morphology of the head and the different order of magnitude between the electrical source (neurons) and the recording device (finite size electrodes) makes it impossible to detect activity of a single neuron swith EEG. In fact, an electric field generated by a single neuron is too weak to be detectable by scalp electrodes, which are large and remote. Furthermore the propagation of electric fields (and of associated current densities) between the scalp and the brain is strongly limited by the skull, as it is more resistive than other head tissues,thus, provoking a considerable shunting effect on the current flow. What is more, the resulting field produced by randomly-oriented neurons can be considered practically null, because all the contributes tend to cancel each other out.

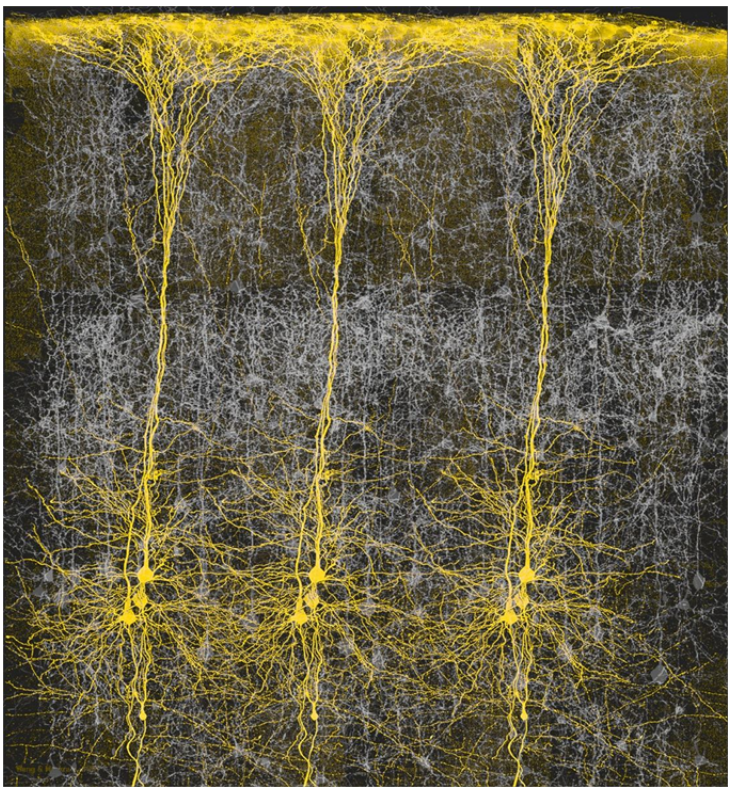

Figure 2.1: Pyramidal cells in brain cortex. Neurons are placed perpendicularly to the cortex surface; their activation is synchronous, resulting in a global electric field that is detectable from the scalp surface.[1]

[1]Source: "Neocortex": IBM / Ecole Polytechnique Federale de Lausanne (EPFL)

Given these limits, EEG electrodes can only detect summed activities of a large number of neurons that are coherently oriented along a common direction and synchronously electrically active [16]. These conditions are verified for a particular class of neurons located in the gray matter: the pyramidal cells. As shown in fig. 2.1 pyramidal cells are a type of neurons located in the gray matter aligned perpendicularly at the brain surface. These cells have an activity locally synchronous, which results in a global electric field detectable by extra-cranial electrodes in the order of μV [7], so three orders of magnitude smaller than the amplitude of the sources of a single neuron (mV).
EEG sources space results thus composed by a discretization of the gray matter in *voxels* elementary cubic volumes enclosing pyramidal neurons networks.

2.2 EEG applications

EEG is a technique that provides a high temporal resolution; in fact,the neural activity detectable is concentrated at low frequencies (at max 30 Hz). Typical EEG waveforms are localized at specific frequencies (*rhythms*) and are indicative of the patient's state (deeply sleep, light sleep, awake and others):

- Delta rhythm: 0.5-4 Hz,
- Theta rhythm: 4-8 Hz,
- Alpha rhythm: 8-13 Hz,
- Beta rhythm: 13-30 Hz.

Classical EEG analysis is based on the empiric examination of electroencephalograms and the spectral analysis of the basic rhythms, which finds application especially in subject monitoring, as in diagnosis of epilepsy [19]; for example fig. 2.2 shows as an epileptic foci causes a characteristic periodic waveform at 3 Hz.
EEG is also used to measure event-related potentials (Chapter 1.2.2). Here brain waves are triggered by an external stimulus which could be of visual, auditory and somatosensory nature. EEG brain imaging instead find more field of applications in presurgical treatment, neurofeedback and BCI (Chapter 1.2).
In the presurgical treatment of epilepsy it has been proven as a high resolution EEG source imaging is a valuable noninvasive functional neuroimaging

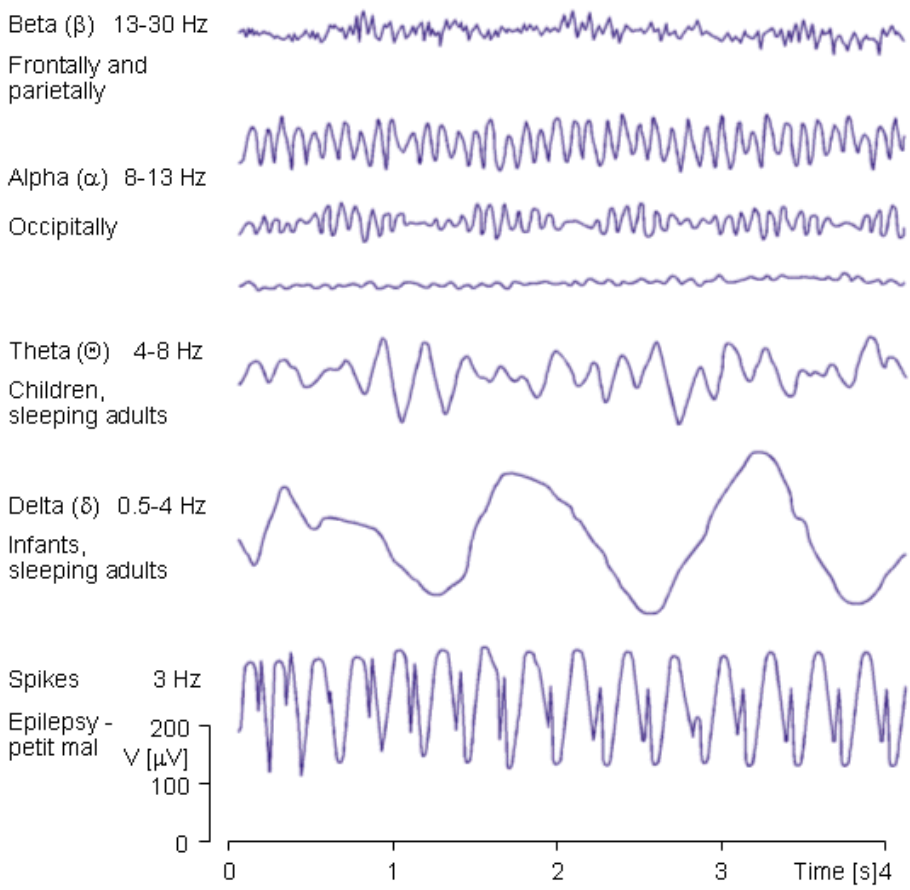

Figure 2.2: *EEG rhythms. All EEG brain rhythms are at frequency less than 30 Hz. Periodic wave at the bottom is generated by an epileptic foci.*[2]

technique [20]. The speed, ease, flexibility, and low costs of this technique warrant its use in clinical practice.

EEG is also used in neurofeedback application, where brain activation maps of the patient are computed and shown to him in real time. This creates a direct interaction between the subject and his neural activity, allowing him to try to modify his cerebral activity. Advantages of EEG-based neurofeedback training have been proven by some studies as in the cases of severe palsies [21], in treating psychological disorders such as attention deficit/hyperactivity disorder(ADHD) [22], neurological disorders [23] as weel as in the improvement and the influencing of improve cognitive performances in healthy subjects [24][25].

EEG application in BCI is a field that is particularly rich, both in medical

[2]Source: [10]

[26] and non-medical solutions [27], where first commercial devices have been recently announced [28].

2.3 EEG Forward and Inverse Problem

As introduced in Chapter 1.1.2, the EEG computational workflow can be divided into two tasks: forward problem and inverse problem.
A forward problem is defined as the determination of the voltage distribution in the volume under analysis, given its electrical properties (local conductivity) and the sources (active voxels) distribution in the gray matter (fig. 2.3). Head volume in EEG data elaboration can be managed as concentric compartments structure, where compartments are defined by the principle head tissues (brain, skull, skin), enclosing the electrical sources volume. Due to the complexity of the domain, analytical solutions are not feasible, and one needs to rely on numerical solvers. Computational resources that are required by a realistic head model are high, thus, simplified head geometries based on concentric spherical shells are often used; however, the limits of this approach in respect to realistic head model are proven [29][30], also in medical usage [31]. What is more, several studies demonstrate that EEG data elaboration is influenced not only by approximations on the compartments surface, by also by irregularities on them like varying thickness, irregular curvatures and holes in the skull [32].

The inverse problem, on the other hand, is defined as the estimation of the

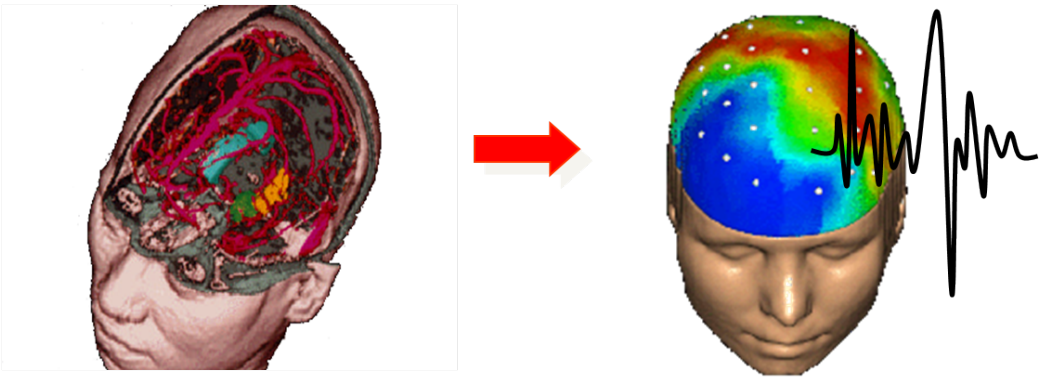

Figure 2.3: *The EEG Forward problem defines the relationship between the voxels's activation inside the brain volume (known its head morphology and conductivity distribution) and the resulting voltage at the electrodes.*[3]

[3]Graphics: *Wellcome trust centre for neuroimaging.*

electrical sources distribution inside the gray matter, given the electrodes measurements and the relationship between the voltage and voxels distribution defined by the forward problem (fig. 2.4). Given the relative small number of passive electrodes, generally from 32 to 256 (512 electrodes configuration are object of research) in proportion to the voxels number (in our work-flow around 200.000, corresponding to a discretization of gray matter with a resolution of around 1.4x1.4x1.4 mm), this problem is ill-posed and with many solutions. So an estimation is necessary that takes into account a-priori informations in order to select the more realistic and physiologically correct solution among the others. The mathematically inverse problem is so defined by an overdetermined system (more unknowns than equations), which can be solved with a numerical approach based on functional minimization coupled with regularization techniques.

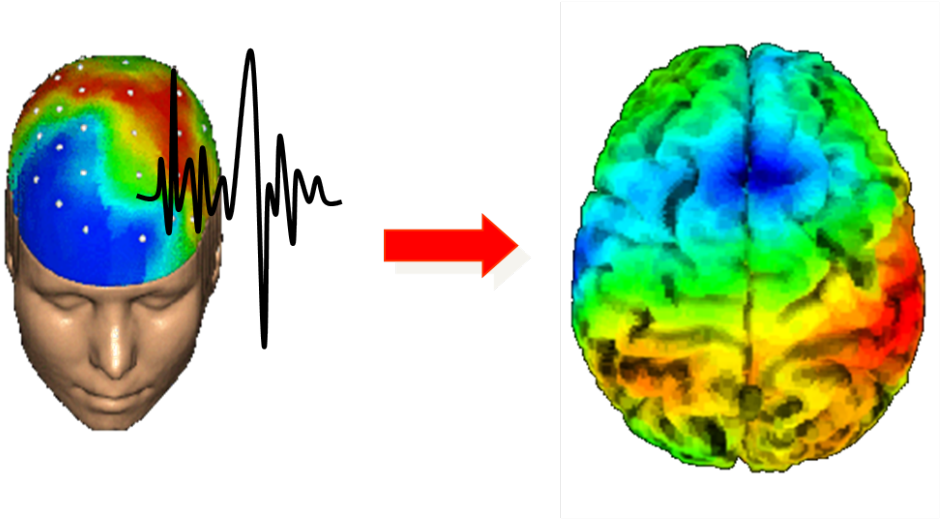

Figure 2.4: *EEG inverse problem. Electrodes potentials are elaborated to localize active voxels inside the brain.*

2.4 EEG Forward Problem: main issues

Plonsey et al. have shown that propagation of electric field in the brain is considerably faster than neuron activation [33]. At each moment in time all the fields are triggered by the active electric sources, which are considerably slower than propagation effects. Consequently, mathematical formulation of the EEG forward problem can be based on Maxwell's equation in quasi-static conditions, neglecting magnetic effects. Head volume can be considered as

a conductive medium, with real local conductivity σ, and the total current flowing on it can be expressed as the sum of currents generated by neural activity sources, *impressed currents* $\boldsymbol{J_m}$, and of ohmic currents given by the generated electric field $\boldsymbol{E}$:

$$\boldsymbol{J}(\boldsymbol{r}) = \boldsymbol{J}_m(\boldsymbol{r}) + \sigma(\boldsymbol{r})\boldsymbol{E}(\boldsymbol{r}) \tag{2.1}$$

2.4.1 Electric source modeling: current dipole

As anticipated by eq. 2.1, the electric source in EEG can be modeled in terms of current density vectors. Considering extracellular space around neurons, total ohmic current flowing across the surface of a finite volume is zero, because there are no electrical sources on it, so:

$$\nabla \cdot \boldsymbol{J} = 0 \tag{2.2}$$

Instead, considering a small volume centered on the top of an active neuron, divergence of currents becomes:

$$\nabla \cdot \boldsymbol{J}(\boldsymbol{r}_1) = \nabla \cdot \boldsymbol{J}_m(\boldsymbol{r}_1) = I \tag{2.3}$$

where $\boldsymbol{r}_1$ is the position of the volume and I the injected volumetric current density. Dually, for a small volume centered on the bottom of the neuron and considering the conservation of charge principle:

$$\nabla \cdot \boldsymbol{J}(\boldsymbol{r}_2) = \nabla \cdot \boldsymbol{J}_m(\boldsymbol{r}_2) = -I \tag{2.4}$$

where $\boldsymbol{r}_2$ is the position of the volume at the bottom of the neuron.
Active neurons can be so modeled as to be current dipoles (fig. 2.5), with a source injecting I and a sink draining it; the divergence of the associated current density is:

$$\nabla \cdot \boldsymbol{J}(\boldsymbol{r}) = I\delta(\boldsymbol{r} - \boldsymbol{r}_1) - I\delta(\boldsymbol{r} - \boldsymbol{r}_2) \tag{2.5}$$

A current dipole associated to a pyramidal cell can be managed with a classical formulation in terms of moment dipole. Taking a current source and current sink as punctual entity with a distance a between them, they can be considered as a current dipole located at position $\boldsymbol{r_{dip}}$ (usually taken on the middle between source and sink) and oriented along the direction $\boldsymbol{e_a}$ from the sink to the source. A moment dipole $\boldsymbol{d}$ can be associated:

$$\boldsymbol{d} = I \cdot a \cdot \boldsymbol{e_a} \tag{2.6}$$

This formulation can be generalized into a voxel volume constituted by a

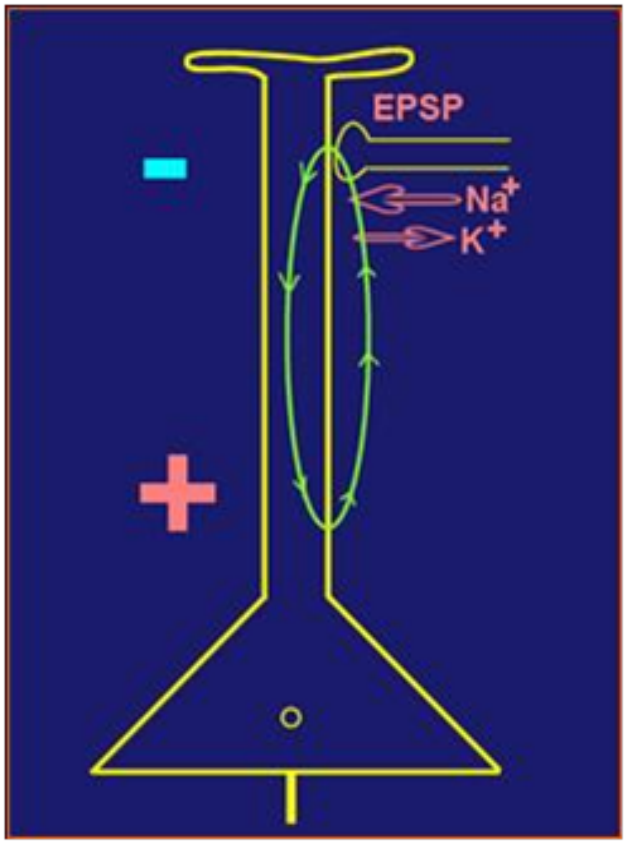

Figure 2.5: *Current dipole model of a pyramidal neuron.*[4]

set of pyramidal neurons with the same orientation and synchronous activation [10]. Considering a small cortex voxel of N pyramidal cells of volume V_k modeled as current dipoles with moment $\boldsymbol{d_l}$, an *impressed current density* $\boldsymbol{J}^i$ can be associated, given by average of all contributes:

$$\boldsymbol{J}^i = \frac{\sum_{l=1}^{N} d_l}{\sum_{l=1}^{N} V_l} = \frac{\boldsymbol{D}}{V} \tag{2.7}$$

So, considering distances between cells inside a voxel negligible in regard to the head size, a voxel can be considered as a unique current dipole moment $\boldsymbol{D}$ and current density $\boldsymbol{J}^i$.

[4]Source: R.D. Pascual-Marqui, The KEY Institute for Brain-Mind Research

2.4.2 Forward problem formulation

Considering a conductive head volume with a set of voxels modeled as current dipoles, the divergence of the total current density of eq. 2.1 on the volume is zero, because the total flux across any closed surface is null:

$$\nabla \cdot \boldsymbol{J} = -I_m + \nabla \cdot (\sigma \boldsymbol{E}) = 0 \tag{2.8}$$

where $\boldsymbol{J}_m(\boldsymbol{r})$ is replaced by $-I_m$. I_m is a volumetric current density inside the volume and take into account contribute of the internal sources. Under quasi-stationary conditions, the electric field $\boldsymbol{E}$ can be expressed only as the gradient of electric potential φ; eq. 2.8 can be thus rewritten:

$$\nabla \cdot (\sigma \boldsymbol{E}) = I_m \;\Rightarrow\; \nabla \cdot (\sigma \nabla \varphi) = -I_m \tag{2.9}$$

Hence, the EEG forward problem is expressed by a Poisson problem in a conductive medium with an internal source given by I_m. Boundary conditions are simply given by imposing continuity of the potential across the interfaces of the volume compartments (brain-skull and skull-skin) and current flux null at the skin external surface (i.e. no currents flowing outside the head).
Given the complexity of the head volume, the Poisson problem is solved with a numerical method, which requires a discretization of the problem variables considering N_E recording electrodes and N_V sources (voxels). Taking a vector $\boldsymbol{\Phi}$ of the electrode potentials of length N_E, and a vector $\boldsymbol{J}$ given by the current dipole sources of length N_V, where each element $\boldsymbol{J}_i$ is a three element vector defined by the i-th current dipole components (D_x,D_y,D_z), the EEG forward model can be algebraically formulated:

$$\boldsymbol{\Phi} = \boldsymbol{K}\boldsymbol{J} \tag{2.10}$$

where $\boldsymbol{K}$ (*lead field matrix*) is a N_ExN_Vx3 matrix given by the solution of the Poisson problem. Generic element K_{ij} determines the contribute to the potential at i-th electrode given by the dipole components at the j-th voxel. This is influenced only by geometry and the conductivity distribution of the volume.

2.4.3 Numerical implementation: main issues and state of the art

Several EEG Forward problem implementations are present in literature, based on different numerical methods and various variants. The methods that are being used the most are Boundary Element Method(BEM) [34][35],

Finite Element Method (FEM) [36] and Finite Difference Method (FDM) [37]. FDM and FEM implementation require a volumetric discretization of the volume as for Finite Volume Method (FVM) used in our EIT implementation (Chapter 3.4.4). Volume results so composed by a volumetric grid of points, where the problem 2.9 is locally applied. This leads to a large sparse square system which must be solved with N_E different right end terms to obtain the lead field matrix $\boldsymbol{K}$ [38]. Given the sizes of the problem (equal to the number of grid nodes), each solution requires complex solvers as iterative algorithms, so derivation of $\boldsymbol{K}$ becomes a critic time consuming step.
Instead, the BEM requires a simpler head model based on surface meshes; the volume is divided into concentric compartments representing principle tissues (brain, skull, skin), and the solution of the problem 2.9 is locally computed at each element of the meshes. This makes BEM implementation computationally less intensive than FEM or FDM because the number of elements of surface meshes is obviously smaller than volumetric ones. BEM also results directly in the searched matrix $\boldsymbol{K}$. However, the BEM work-flow requires the inversion of a large dense square matrix, whose dimensions are equal to the total number of elements of the surface meshes; this step in particular turns out to be very critical and time-consuming. However, once the matrix is inverted, only a matrix multiplication is needed to obtain the scalp potentials. This limited computational load is an attractive feature when solving the inverse problem, where a large number of forward evaluations needs to be performed. For this reasons BEM is largely used, and present in commercial solution [39] and EEG toolbox [40].
Despite these consideration, BEM is penalized in regard to FEM and FDM because it is not capable of anisotropic conductivity, which as it will be explained in chapter 3.4.3, has a considerable influence on the current distribution inside the head.

2.5 EEG Forward Problem: Boundary Element implementation

BEM implementation provides a solution to the EEG forward problem on the points at the interfaces between head tissues. The head has to be modeled as a compartmental volume enclosing the electric sources (current dipoles). Each compartment represents an head tissue and is considered isotropic.

2.5.1 Domain setting

Head volume is defined starting from high resolution MRI scans. MRI images are segmented using *freesurfer* [41][42], an open-source automatic segmentation and surface extraction tool for MRI images. This tool performs a graphical elaboration of the images using a-priori brain atlas, resulting in equivalent segmented images where each pixel is classified according to the belonging tissue. Then, volumes enclosing pixels of the same regions are tessellated with triangulated meshes, thus defining brain, skull and skin surfaces. Each mesh consists of about 3500 triangles, resulting in about a total number of about 10000 elements (fig. 2.6).
MRI pixels belonging to gray matter are taken as source voxels distribution, which results in about 200000 voxels (fig. 2.7).
At each compartment is associated a real conductivity value, given the low frequency of EEG. In particular we have used typical values present in literature: $0.3 S/m$ for brain, $0.006 S/m$ for skull and $0.4 s/m$ for skin (Table 3.1).

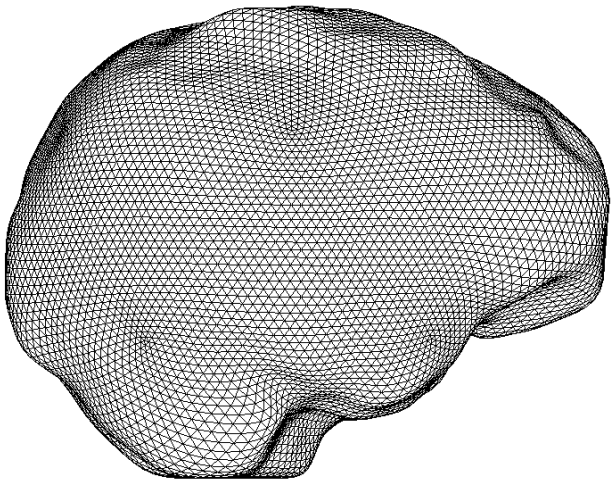

Figure 2.6: *Triangular mesh of the brain computed by freesurfer performing MRI segmentation and surface tesselation.*

2.5.2 Numerical model

BEM numerical model implemented is based on formulation given by [34][35]. Considering a current source located at position $\boldsymbol{r_0}$ in an inhomogeneous con-

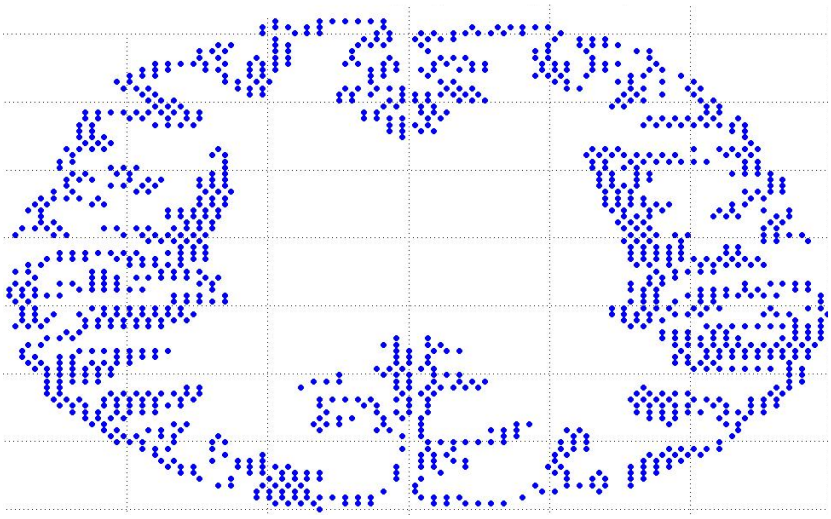

Figure 2.7: *Voxels distribution in a gray matter slice.*

ductor constituted by N compartments separated by $S_j, j = 1, ..., N$ surfaces, voltage φ at position $\boldsymbol{r} \in S_k$ can be evaluated as:

$$\bar{\sigma}_k \varphi(\boldsymbol{r}) = \sigma_0 \varphi_\infty(\boldsymbol{r}) + \frac{1}{4\pi} \sum_{j=1}^{N} \Delta\sigma_j \iint_{S_j} \varphi(\boldsymbol{r}) \hat{\boldsymbol{n}}(\boldsymbol{r}) \frac{\boldsymbol{r} - \boldsymbol{r_0}}{|\boldsymbol{r} - \boldsymbol{r_0}|^3} \, \mathrm{d}S \qquad (2.11)$$

where $\varphi_\infty(\boldsymbol{r})$ is the potential generated by the current source in an infinite homogeneous medium with conductivity σ_0, $\Delta\sigma_j$ the difference between the outer and the inner conductivity at interface S_j, $\hat{\boldsymbol{n}}$ the unit versor normal to S_j and $\bar{\sigma}_k$ the average conductivity across the surface S_k (fig. 2.8). The potential on surface S_k results given by two contributors: the first takes into account the electric source considering ideal situation of an unlimited isotropic medium, while the second considers effects induced by the real geometries of the volume, evaluating potential variations at the interfaces between isotropic compartments, corresponding to discontinuities in the conductivity distribution.
Integral of eq. 2.11 can be approximated in this so discretized domain as the sum on each triangle of the surfaces, resulting:

$$\begin{aligned} \bar{\sigma}_k \varphi(\boldsymbol{r}) =& \sigma_0 \varphi_\infty(\boldsymbol{r}) + \\ & \frac{1}{4\pi} \sum_{j=1}^{N} \Delta\sigma_j \sum_{i=1}^{N_{S_j}} \iint_{\Delta S_{i,j}} \varphi(\boldsymbol{r}) \hat{\boldsymbol{n}}(\boldsymbol{r}) \frac{\boldsymbol{r} - \boldsymbol{r_0}}{|\boldsymbol{r} - \boldsymbol{r_0}|^3} \, \mathrm{d}S \end{aligned} \qquad (2.12)$$

where $\Delta S_{i,j}$ is the i-th triangle of surface S_j. Eq. 2.12 can not be solved analytically; an approximated solution can be obtained defining φ on surface

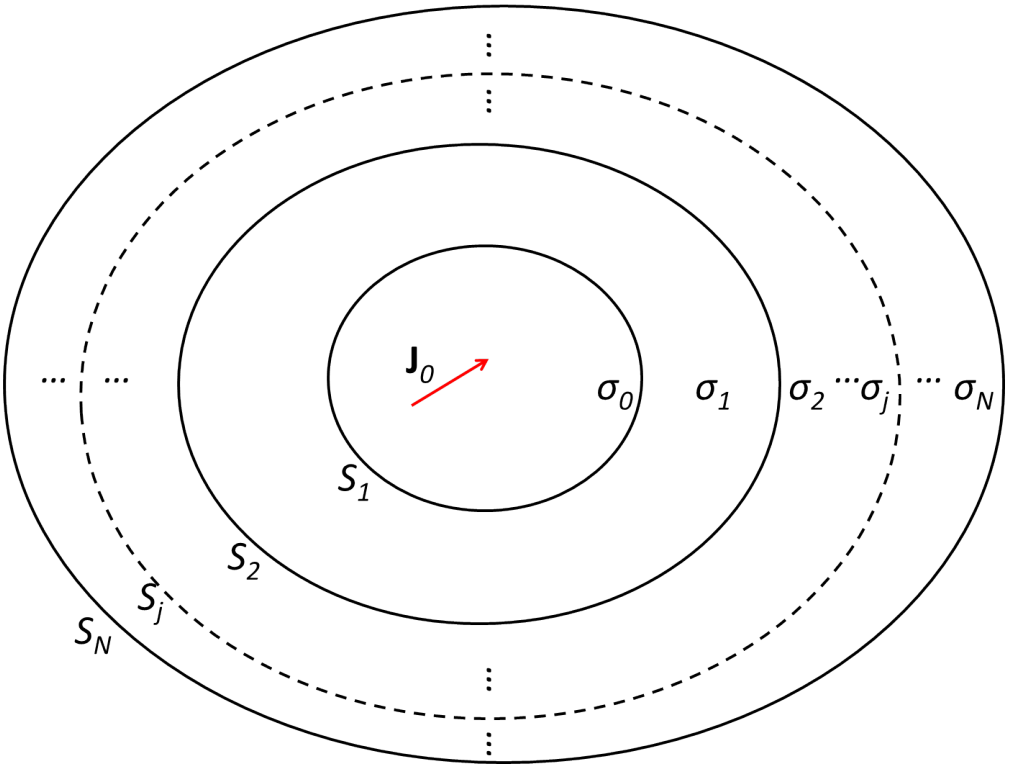

Figure 2.8: *Generic volume organized in homogeneous isotropic compartments. Red arrows is a generic current source in the innermost compartments.*

S_j as a linear combinations of N_{S_j} basis functions:

$$\tilde{\varphi}^j(\boldsymbol{r}) = \sum_{l=1}^{N_{S_j}} \varphi_l^j h_l(\boldsymbol{r}) \tag{2.13}$$

Substituting eq. 2.13 in eq. 2.12 results into:

$$\begin{aligned}\bar{\sigma}_k\varphi(\boldsymbol{r}) =& \sigma_0\varphi_\infty(\boldsymbol{r}) + \\ & \frac{1}{4\pi}\sum_{j=1}^{N}\Delta\sigma_j\sum_{i=1}^{N_{S_j}}\sum_{l=1}^{N_{S_j}}\varphi_l^j\iint_{\Delta S_{i,j}} h_l(\boldsymbol{r})\hat{\boldsymbol{n}}(\boldsymbol{r})\frac{\boldsymbol{r}-\boldsymbol{r_0}}{|\boldsymbol{r}-\boldsymbol{r_0}|^3}\,\mathrm{d}S.\end{aligned} \tag{2.14}$$

This equation can be more easily written in terms of matrices as:

$$\boldsymbol{\Phi} = \boldsymbol{\Phi_0} + \boldsymbol{C}\boldsymbol{\Phi} \tag{2.15}$$

where $\boldsymbol{\Phi}$ is the unknown vector of the coefficients φ_l^j of eq. 2.14, $\boldsymbol{\Phi_0}$ is the discretization of the first term while matrix $\boldsymbol{C}$ of the second. $\boldsymbol{C}$ coefficients

are determined only by the surfaces geometry and conductivity values once the set of basis functions $h_l(\boldsymbol{r})$ is chosen.
The potentials are defined up to an additive constant; this ambiguity can be removed by deflation, substituting $\boldsymbol{C}$ with its deflated version [43].
Finally, given an identity matrix $\boldsymbol{I}$ of N_txN_t size, with N_t as the total number of triangles on all surfaces, the linear relationship between potentials and a current source is:

$$\boldsymbol{\Phi} = (\boldsymbol{I} - \boldsymbol{C})^{-1}\boldsymbol{\Phi_0} = \boldsymbol{A}^{-1}\boldsymbol{\Phi_0}. \tag{2.16}$$

The discretitazion of the problem derives from the assumption of surfaces defined by meshes done by planar triangular elements. In particular $\boldsymbol{\Phi}$ and $\boldsymbol{\Phi_0}$ in our implementation are vectors of the potential evaluated on the centroid of each triangle of the meshes. $\boldsymbol{A}$ is a real dense square matrix N_txN_t, so considering the size of meshes involved ($N_t \approx 10000$), its inversion is a critical step of the BEM formulation and highly time-consuming.

Constant basis functions

The selection of $h_l(\boldsymbol{r})$ influences directly the computational load necessary to obtain matrix $\boldsymbol{C}$. A common choice is to consider constant potentials at each triangle' s surface. So considering a generic triangle ΔS_l, this results in a set of constant basis functions:

$$h_l(\boldsymbol{r}) = \begin{cases} 1 & \boldsymbol{r} \in \Delta S_l \\ 0 & \boldsymbol{r} \notin \Delta S_l. \end{cases} \tag{2.17}$$

With constant basis functions, the integral of eq. 2.14 results to be the measure of the solid angle Ω given by the oriented i-*th* planar triangle $\Delta S_{i,j}$ belonging to the surface S_j and centered at the point $\boldsymbol{r} - \boldsymbol{r_0}$:

$$\Omega = \iint_{\Delta S_{i,j}} \hat{\boldsymbol{n}}(\boldsymbol{r}) \frac{\boldsymbol{r} - \boldsymbol{r_0}}{|\boldsymbol{r} - \boldsymbol{r_0}|^3} \, \mathrm{d}S. \tag{2.18}$$

Ω can be algebraically computed using the *Oosterom and Strackee* formula, which for a triangular surface defined by vertexes $\boldsymbol{a}, \boldsymbol{b}, \boldsymbol{c}$ asserts that :

$$tan(\frac{1}{2}\Omega) = \frac{|\boldsymbol{abc}|}{abc + (\boldsymbol{a}\cdot\boldsymbol{b})c + (\boldsymbol{a}\cdot\boldsymbol{c})b + (\boldsymbol{b}\cdot\boldsymbol{c})a} \tag{2.19}$$

Isolated skull approach (ISA)

The head model used in our forward problem formulation involves 3 layers: scalp, skull and brain with conductivities $\sigma_1, \sigma_2, \sigma_3$ and surfaces S_1, S_2, S_3 respectively . As previously introduced, the skull conductivity is lower than

the one of the brain and the scalp. Defining β as the ratio between skull and brain conductivity ($\beta = \sigma_2/\sigma_3$), solution of eq. 2.14 is affected by high numerical errors for small β ($\beta < 0.1$). To avoid this problem, an Isolated Skull Approach (ISA) is used [44]. Eq. 2.15 can be split into blocks refering to each compartments:

$$\begin{pmatrix} \boldsymbol{\varphi}_1 \\ \boldsymbol{\varphi}_2 \\ \boldsymbol{\varphi}_3 \end{pmatrix} = \begin{pmatrix} \boldsymbol{C}_{11} & \boldsymbol{C}_{12} & \boldsymbol{C}_{13} \\ \boldsymbol{C}_{21} & \boldsymbol{C}_{22} & \boldsymbol{C}_{23} \\ \boldsymbol{C}_{31} & \boldsymbol{C}_{32} & \boldsymbol{C}_{33} \end{pmatrix} \begin{pmatrix} \boldsymbol{\varphi}_1 \\ \boldsymbol{\varphi}_2 \\ \boldsymbol{\varphi}_3 \end{pmatrix} + \begin{pmatrix} \boldsymbol{\varphi}_{01} \\ \boldsymbol{\varphi}_{02} \\ \boldsymbol{\varphi}_{03} \end{pmatrix} \tag{2.20}$$

With this partition of the problem, it is evident as, if $\beta << 1$ (like conductivity ratio across S_3), the potential $\boldsymbol{\varphi}_3$ is much greater than $\boldsymbol{\varphi}_1$ and $\boldsymbol{\varphi}_2$ causing numerical errors in the matrix solution. Using the ISA approach, an alternative $\boldsymbol{\varphi}_3^{'}$ is computed on S_3 considering a head volume where the same brain conductivity σ_3 is associated to each layer (brain, skull, skin):

$$\boldsymbol{\varphi}_3^{'} = \boldsymbol{C}_{33}\boldsymbol{\varphi}_3^{'} + \boldsymbol{\varphi}_{03}^{'} \;\Rightarrow\; \boldsymbol{\varphi}_3^{'} = (\boldsymbol{A}_{33})^{-1}\boldsymbol{\varphi}_{03}^{'} \tag{2.21}$$

Using $\boldsymbol{\varphi}_3^{'}$ as source terms, problem 2.20 can be so modified:

$$\boldsymbol{\varphi}_0^{'} = \begin{pmatrix} \boldsymbol{\varphi}_{01}^{'} \\ \boldsymbol{\varphi}_{02}^{'} \\ \boldsymbol{\varphi}_{03}^{'} \end{pmatrix} = \begin{pmatrix} \beta\boldsymbol{\varphi}_{01} \\ \beta\boldsymbol{\varphi}_{02} \\ \beta\boldsymbol{\varphi}_{03} - \frac{2\sigma_2}{\sigma_2+\sigma_3}\boldsymbol{\varphi}_{03}^{'}. \end{pmatrix} \tag{2.22}$$

Solving problem 2.20 with these modified source terms leads to a solution in the form of:

$$\boldsymbol{\varphi}^{'} = \boldsymbol{A}^{-1}\boldsymbol{\varphi}_0^{'} = \begin{pmatrix} \beta\boldsymbol{\varphi}_1 \\ \beta\boldsymbol{\varphi}_2 \\ \beta\boldsymbol{\varphi}_3 - \boldsymbol{\varphi}_3^{'} \end{pmatrix} \tag{2.23}$$

where finally $\boldsymbol{\varphi}$ can be derived from the computed $\boldsymbol{\varphi}^{'}$.
The ISA approach, as showed in [44], allows the reduction of numerical inaccuracies in computation of the model. However it increases the computational load of the algorithm because it requires two forward problem solutions, one to solve pr. 2.21 and one for pr. 2.23.

Lead field matrix: electric sources and electrodes selection

Eq. 2.11 requires the computation of vector potentials $\boldsymbol{\varphi}_0$ given by the electric source considering ideal situation of an unlimited isotropic medium with homogeneous conductivity σ_0. Considering a voxel modeled as current dipole with moment $\boldsymbol{D}$ located at $\boldsymbol{r}_{dip}$, the potential in an infinite homogeneous medium is:

$$\varphi(\boldsymbol{r}) = \frac{\boldsymbol{D}(\boldsymbol{r} - \boldsymbol{r_{dip}})}{2\pi\sigma_0 \left|\boldsymbol{r} - \boldsymbol{r_{dip}}\right|^3} \tag{2.24}$$

with $\boldsymbol{D} = \boldsymbol{J}V$ as showed in eq. 2.7 (for simplicity in the notation $\boldsymbol{J}^i$ is now replaced in the rest of the work with $\boldsymbol{J}$).
Considering N_V voxels, because the electric field of more sources can be calculated as the sum of fields generated by each single source, the potential at each triangle of the meshes φ_0 is given by the sum of all voxels contribute to the centroids indicating each triangle:

$$\boldsymbol{\varphi}_0 = \boldsymbol{GJ} \tag{2.25}$$

where $\boldsymbol{G}$ is N_txN_Vx3 matrix where each column is a 3 vector expressing contributors of each voxel at each centroid. Placing eq. 2.25 into eq. 2.16 yields:

$$\boldsymbol{\Phi} = (\boldsymbol{I} - \boldsymbol{C})^{-1}\boldsymbol{GJ} = \boldsymbol{A}^{-1}\boldsymbol{GJ}. \tag{2.26}$$

In order to select only potentials on the electrodes, eq.2.26 is premultiplicated by a matrix $\boldsymbol{D}$ of N_exN_t elements, which simply selects rows corresponding to electrodes points:

$$\boldsymbol{\Phi} = \boldsymbol{D}(\boldsymbol{I} - \boldsymbol{C})^{-1}\boldsymbol{GJ} = \boldsymbol{DA}^{-1}\boldsymbol{GJ} = \boldsymbol{KJ} \tag{2.27}$$

Finally it results in the desired lead field matrix $\boldsymbol{K}$ of the EEG forward problem (eq. 2.10).

2.5.3 BEM parallel multi-core implementation

The BEM formulation requires computationally intensive matrix operations; however, the highest computational load required is concentrated in the inversion of a large, dense matrix (eq. 2.27). It is well-established that the dense matrix inversion is a critic algebraic operation, and often it is preferred to avoid it, preferring the usage of different linear system solvers or ad-hoc algorithms, which exploit properties of the matrix (e.g. symmetric matrix). This is not always possible, as in our case. However, we were able to drastically reduce computation times using our GPU-accelerated solver to compute general matrix inversion. With a dense matrix 10000x10000, our solver allow inverse matrix computation in less than 30 s, so with a speed-up of 60x respect to a CPU general purpose solution. Its design will be outlined in Chapter 4.2.2.

2.6 EEG Inverse Problem: main issues

The EEG inverse problem is based on measurement and mapping of electrical activity produced by the brain as recorded by electrodes placed on the

scalp. Mathematically inverse problem is defined by the inversion of the lead field matrix $\boldsymbol{K}$ in eq. 2.10 in order to provide current density distribution $\boldsymbol{J}$ on the N_V cortex voxels given the voltage measurements on N_E electrodes. Unfortunately, direct inversion of $\boldsymbol{K}$ is not possible, because it is a N_ExN_Vx3 matrix; moreover $N_V >> N_E$ resulting thus in an highly underdetermined problem. However, good results can be achieved using appropriate estimators; a rich literature exists of methods to solve EEG inverse problem using linear estimator, exploiting directly properties of $\boldsymbol{K}$.
Linear estimators are simples but characterized by a low spatial resolution; what often happens is that the resulting image has a high level of smoothing, although good results can be achieved on localization of brain source activity. A more focused activity map can be obtained using non-linear estimator; however, the computational load required increases largely. The computational issue is a critical aspect in the EEG inverse problem, e.g. in neurofeedback and complex brain-computer interface (BCI) applications, where real-time constraints are required.

2.6.1 State of the art

The EEG inverse problem addresses the estimation of the source distribution inside the head based on *a-priori* informations, which allows to select a specific and realistic solution between the others.
One of the first solver presented is the Minimum Norm (MN) solution [45]. Considering the EEG forward problem 2.27, MN is based on the minimization of the functional F:

$$F(\boldsymbol{J}) = \|\boldsymbol{\Phi} - \boldsymbol{K}\boldsymbol{J}\|_2 \tag{2.28}$$

This formulation only searches a 3D current distribution with minimum intensity on the volume. This choice, although plausible from a physic point of view (minimum norm is the solution of many complex physic systems, as energy distribution) is not necessarily physiologically valid. There is no proof in fact that cerebral activity is based on minimum norm distribution. In addition this algorithm privileges smoothed solutions, where energy is spanned on many voxels, instead of focused solution. Consequently it favors superficial sources, because less activity is required in superficial voxels to obtain the measured scalp voltage distribution, which leads to physiologically wrong results. To compensate this effect different solutions have been proposed based on the usage of weighting strategies (Weighted Minimum Norm, WMN), e.g. given by the norm of the columns of $\boldsymbol{K}$ [46], or by the covariance data matrix [47]. These algorithms allow to overcome underestimation of deep sources, but it is important to highlight that they are purely

mathematical techniques, so as they are based on assumptions they are not physiologically proven.
A well-known WMN method is LORETA (Low-resolution electromagnetic tomography) [48], which is based on the minimization of the Laplacian of the weighted current density vector. This constraint is physiologically justified from experimental data showing that the activity of neighboring neurons in the cerebral cortex is highly correlated. However, in real implementations the low EEG spatial resolution makes it impracticable to use voxel densities high enough to justify this constraint, which generally leads to over-smoothed solutions. Currently, one of most widely used methods is the standardized LORETA (sLORETA) [39] which estimates the current density distribution by minimizing a cost function defined by a zero order Tikhonov-Philips regularization instead of a classic L2-norm. Additionally, the solution is scaled according to an estimate of its variance. This way, it is possible to detect single active voxels with zero localization error in a noise-free environment. Unfortunately, both LORETA and sLORETA generate source distributions with low spatial resolution. A promising method for enhancing the resolution is the FOCal Undetermined System Solver (FOCUSS) [49]. FOCUSS is an iterative non-linear WMN method performing recursive adjustments to the weighting matrix until most elements are close to zero, thus achieving a localized solution. In this case though, the final solution depends to some degree on the assumed initial current distribution.

2.7 EEG inverse problem: numerical implementation

In our framework we have implemented an accelerated version of sLORETA algorithm to solve EEG inverse problem. Images generated by this solver have a high smoothness level, so in order to provide more focused solutions we apply non-linear FOCUSS estimator onto them. FOCUSS is an iterative method whose convergence is guaranteed only with a correct initialization; at this scope the initial solution is provided by sLORETA, which is able to provide blurred images, but with zero-localization error in noise-free environment. This procedure is also known in literature as Standardized Shrinking sLORETA-FOCUSS (SSLOFO) [50].
SSLOFO algorithm is now described. Being composed by two distinct algorithms, sLORETA and FOCUSS are separately presented.

2.7.1 sLORETA

Considering the EEG forward problem formulation 2.27, voxels' current densities $\boldsymbol{J}$ estimation from electrodes potential vector $\boldsymbol{\Phi}$ is performed by a zero-order Tikhonov-Philips regularization. This consists of the solution of the following minimum problem:

$$min_{\boldsymbol{J}} \left\{ \|\boldsymbol{\Phi} - \boldsymbol{K}\boldsymbol{J}\|^2 + \alpha \|\boldsymbol{J}\|^2 \right\} \tag{2.29}$$

where α is a regularization parameter. Two terms of eq. 2.29 can be seen as two minimum problems: the first provides a minimization of the error (it is practically a MN estimator), the second provides a minimization of the energy associated to the current densities. α determines the ratio between these two minimizations; it is difficult to quantify α, so many approaches exist in literature. With simple algebraic passes, it can be demostrated that the problem 2.29 is solved by:

$$\hat{\boldsymbol{J}} = \boldsymbol{T}\boldsymbol{\Phi} \tag{2.30}$$

where $\hat{\boldsymbol{J}}$ is vector of the estimated current densities, and $\boldsymbol{T}$ is evaluated from the *Moore-Penrose Pseudo Inverse* of $\boldsymbol{K}$:

$$\boldsymbol{T} = \boldsymbol{K}^T(\boldsymbol{K}\boldsymbol{K}^T + \alpha\boldsymbol{I})^{-1} \tag{2.31}$$

where $\boldsymbol{I}$ is the identity matrix. Substituting eq. 2.27 into eq. 2.30 and considering eq. 2.31:

$$\hat{\boldsymbol{J}} = \boldsymbol{T}\boldsymbol{K}\boldsymbol{J} = \boldsymbol{R}\boldsymbol{J} \tag{2.32}$$

where $\boldsymbol{R}$ is called resolution matrix and it is given by:

$$\boldsymbol{R} = \boldsymbol{K}^T(\boldsymbol{K}\boldsymbol{K}^T + \alpha\boldsymbol{I})^{-1}\boldsymbol{K} \tag{2.33}$$

The resolution matrix expresses the relationship between the real distribution of current sources and the estimated version. If the problem was well-posed and not undetermined, it would be an identity matrix. Obviously this is not the case, and in particular $\boldsymbol{R}$ is not invertible. However, resolution matrix is used in sLORETA workflow to standardize $\hat{\boldsymbol{J}}$; 3x3 sub-matrices $\boldsymbol{R}_{ll}$ are extracted from $\boldsymbol{R}$ along its main diagonal. $\boldsymbol{R}_{ll}$ is associated to l-th voxel, and relative $\hat{\boldsymbol{J}}_l$ is so normalized:

$$\hat{J}_{l,std} = \hat{\boldsymbol{J}}_l^{\,T} \boldsymbol{R}_{ll}^{-1} \hat{\boldsymbol{J}}_l \tag{2.34}$$

where $\hat{J}_{l,std}$ is the standardized power associated with the estimated $\hat{\boldsymbol{J}}_l$.
This technique allows to obtain high localization performances. In particular with one current source in a noise-free environment, although the intrinsic smoothing in the resulting image, the center of the image is correctly located at the source position.

2.7.2 Standardized FOCUSS

The FOCal Undetermined System Solver (FOCUSS) is a non linear iterative WMN method, where during each step the solution is updated according to the previous one. Considering the EEG forward problem formulation 2.27, the current densities $\boldsymbol{J}$ estimation from electrodes potential vector $\boldsymbol{\Phi}$ is performed solving the following minimum problem:

$$min_{\boldsymbol{J}} \|\boldsymbol{CJ}\|^2 \quad with\, \boldsymbol{\Phi} = \boldsymbol{KJ} \tag{2.35}$$

where $\boldsymbol{C}$ is a weighting matrix defined as:

$$\boldsymbol{C} = \boldsymbol{W}^T\boldsymbol{W} \tag{2.36}$$

with $\boldsymbol{W}$ a diagonal matrix $3N_V$x$3N_V$ iteratively refined at each iteration. With algebraic passes, solution of problem 2.35 at generic step i is found:

$$\begin{aligned}\hat{\boldsymbol{J}}_i =& \boldsymbol{C}_i^{-1}\boldsymbol{K}^T(\boldsymbol{K}\boldsymbol{C}_i^{-1}\boldsymbol{K}^T)^{-1}\boldsymbol{\Phi} = \\ & \boldsymbol{W}_i\boldsymbol{W}_i^T\boldsymbol{K}^T(\boldsymbol{K}\boldsymbol{W}_i\boldsymbol{W}_i^T\boldsymbol{K}^T)^{-1}\boldsymbol{\Phi}\end{aligned} \tag{2.37}$$

At i-th iteration, $\boldsymbol{W}_i$ is updated according to the solution found on the previous step $\hat{\boldsymbol{J}}_{i-1}$:

$$\boldsymbol{W}_i = \boldsymbol{P}\boldsymbol{W}_{i-1}diag(\hat{\boldsymbol{J}}_{i-1}(1), \hat{\boldsymbol{J}}_{i-1}(2), ..., \hat{\boldsymbol{J}}_{i-1}(3N_V)) \tag{2.38}$$

$\boldsymbol{P}$ is a diagonal matrix, which scales solution at each step to take into account deep sources, avoiding to favor the most external sources:

$$\boldsymbol{P} = diag(\frac{1}{\|\boldsymbol{K}_1\|}, \frac{1}{\|\boldsymbol{K}_2\|}, ..., \frac{1}{\|\boldsymbol{K}_{3N_V}\|}) \tag{2.39}$$

where $\|\boldsymbol{K}_j\|$ is the norm of j-th column of $\boldsymbol{K}$.
FOCUSS allow to obtain highly focused images, but it is very sensible to initial solution. The computational load required for each step is higher than the linear method of sLORETA. A possibility to limit this aspect is to shrink the solution space between each iteration, deleting voxels when the associated estimated current density becomes lower than a prefixed threshold. In fact, given the nature of the algorithm, in successive steps these contributes will be always lower.
Also in FOCUSS it is possible to introduce a standardization of results, which as shown in sLORETA allows a higher quality solution. A resolution matrix between real $\boldsymbol{J}$ and estimated $\hat{\boldsymbol{J}}$ can be evaluated substituting eq. 2.27 into eq. 2.37:

$$\hat{\boldsymbol{J}} = \boldsymbol{W}_i\boldsymbol{W}_i^T\boldsymbol{K}^T(\boldsymbol{K}\boldsymbol{W}_i\boldsymbol{W}_i^T\boldsymbol{K}^T)^{-1}\boldsymbol{K}\boldsymbol{J} = \boldsymbol{R}\boldsymbol{J} \tag{2.40}$$

with resolution matrix $\boldsymbol{R}$ given by:

$$\boldsymbol{R} = \boldsymbol{W}_i \boldsymbol{W}_i^T \boldsymbol{K}^T (\boldsymbol{K} \boldsymbol{W}_i \boldsymbol{W}_i^T \boldsymbol{K}^T)^{-1} \boldsymbol{K} \tag{2.41}$$

Then, as in sLORETA, standardization is locally performed extracting $\boldsymbol{R}_{ll}$ associated to l-th voxel, and relative $\hat{\boldsymbol{J}}_l$ is so normalized:

$$\hat{J}_{l,std} = \hat{\boldsymbol{J}}_l^T \boldsymbol{R}_{ll}^{-1} \hat{\boldsymbol{J}}_l \tag{2.42}$$

where $\hat{J}_{l,std}$ is the standardized power associated to the estimated $\hat{\boldsymbol{J}}_l$.

2.7.3 SSLOFO algorithmic workflow

Standardized Shrinking LORETA-FOCUSS (SSLOFO) combines the advantages of sLORETA and FOCUSS, coupling the high localization performances of sLORETA with the focusing properties of FOCUSS.
Starting from a blurred source distribution determined by sLORETA, iterative steps performed by FOCUSS enhance the strength of preeminent elements while decreasing others. This is obtained by adjusting the weighting matrix $\boldsymbol{W}$ recursively. In addition, the portions of the solution space that are unlikely to contain any brain activity are discarded and not considered in the following iterations.
During SSLOFO iterations, local minima can occur, trapping the current solution and blocking the convergence of the method. To avoid this, current solution is slightly smoothed before entering a new iteration [51].
During SSLOFO elaboration, different criteria can be used to force the end of the method:

1. two successive iterations do not further improve the solution;
2. solution provided by an iteration is less sparse than the previous one;
3. the source strength of a node exceeds a user-defined threshold.

Single steps of SSLOFO are directly given by sLORETA and FOCUSS workflow; a summary of the individual steps of the SSLOFO algorithm is presented in Chapter 4.2.2, where their implementation on multi-core architectures is also discussed.

2.8 EEG Inverse Problem: simulations and results

SSLOFO is implemented on a multi-core GPU based machine desktop PC, in order provide a suitable tool able to elaborate in real time constraints data

acquired by EEG instrumentation. Referring to the temporal requirement of a BCI system, characterized by a feedback time in the order of 100-200 ms, a number of 10 frames per second (FPS) was taken as the minimum threshold to define a real-time constraint. A frame here refers the complete evaluation of the source distribution for a one time instant. As previously introduced, the usage of non-linear reconstruction method heavily increases the computational power required. In our case, sLORETA implementation allows to work in real-time with all typical configurations used in an EEG environment (32-128 electrodes, up to 32000 voxels) and more advanced configuration ($>$ 100000 voxels). In fig. 2.9 a screenshot of our 3D openGL-based graphical interface is shown, plotting voxel activation maps computed by sLORETA; here each pixel represents a voxel and its color stands for the power estimated; on the left input data recorded by electrodes are plotted in an electroencephalogram way. Head model is computed by our hardware accelerated BEM implementation, starting from MRI scans of the head's subject. It is important to highlight as improved performances in EEG forward and inverse solver allow to obtain a complete EEG data elaboration framework based on a realistic head model specific of the patient in exam (fig. 2.10).

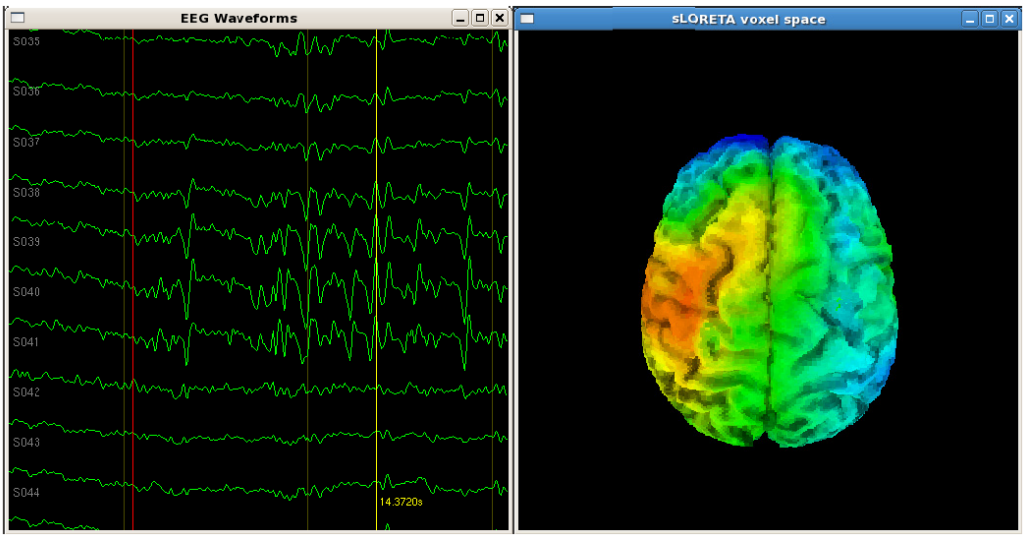

Figure 2.9: *EEG source localization graphical user interface.*

Compared to sLORETA, FOCUSS iterations in SSLOFO work-flow are very time-consuming and with more than 64 electrodes severely limit a real-time elaboration of data. Details of SSLOFO implementation on GPU and the performances achieved are presented in Chapter 4.2.2.

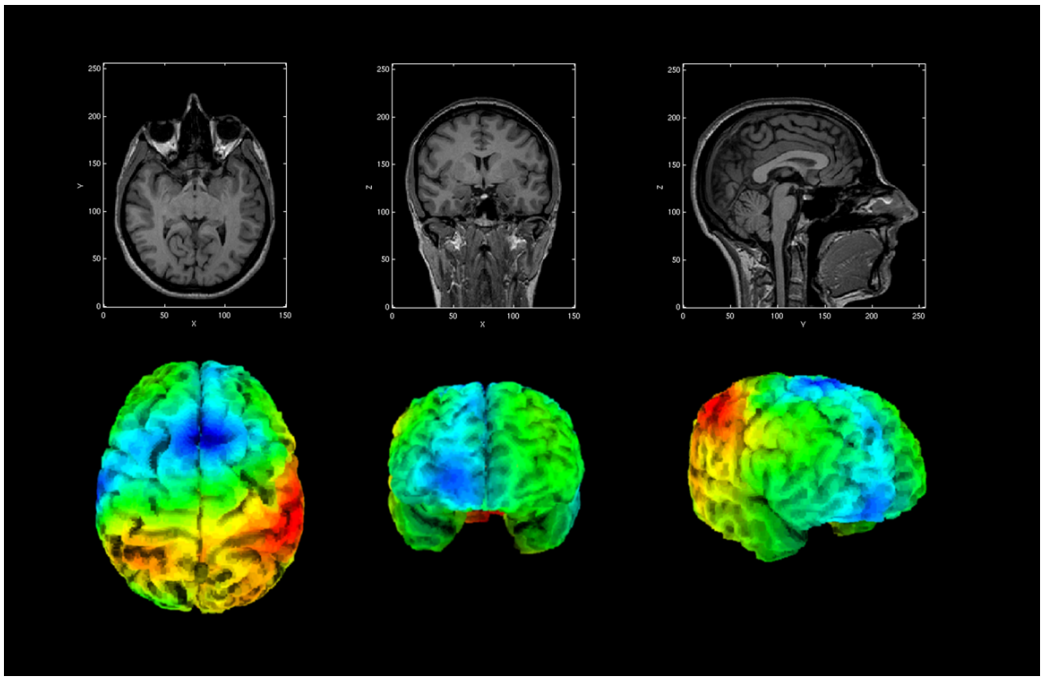

Figure 2.10: *EEG source localization graphical user interface. Patient specific head model is obtained by BEM work-flow starting from MRI scans of the subject; then it is used in EEG inverse problem work-flow.*

An example of SSLOFO EEG reconstruction it is shown in fig. 2.11, which considers a conductive volume constituted by semi-spherical concentric compartments, assuming voxels distributed on a semi-spherical surface and 64 recording electrodes. A single active dipole is considered, and the corresponding potential at the electrodes are evaluated solving the EEG forward problem. Then EEG inverse problem is solved with SSLOFO work-flow. Preliminary sLORETA implementation results in the voxel activity shown in fig. 2.11.a; sLORETA is able to correctly localize the active dipole (brightest point), but the solution has a high level of smoothness around the target point. Successive SSLOFO iterations reduce the smoothness of the figure just in the first one (fig. 2.11.b), while after five iterations the power is totally concentrated on the target dipole (fig. 2.11.c).

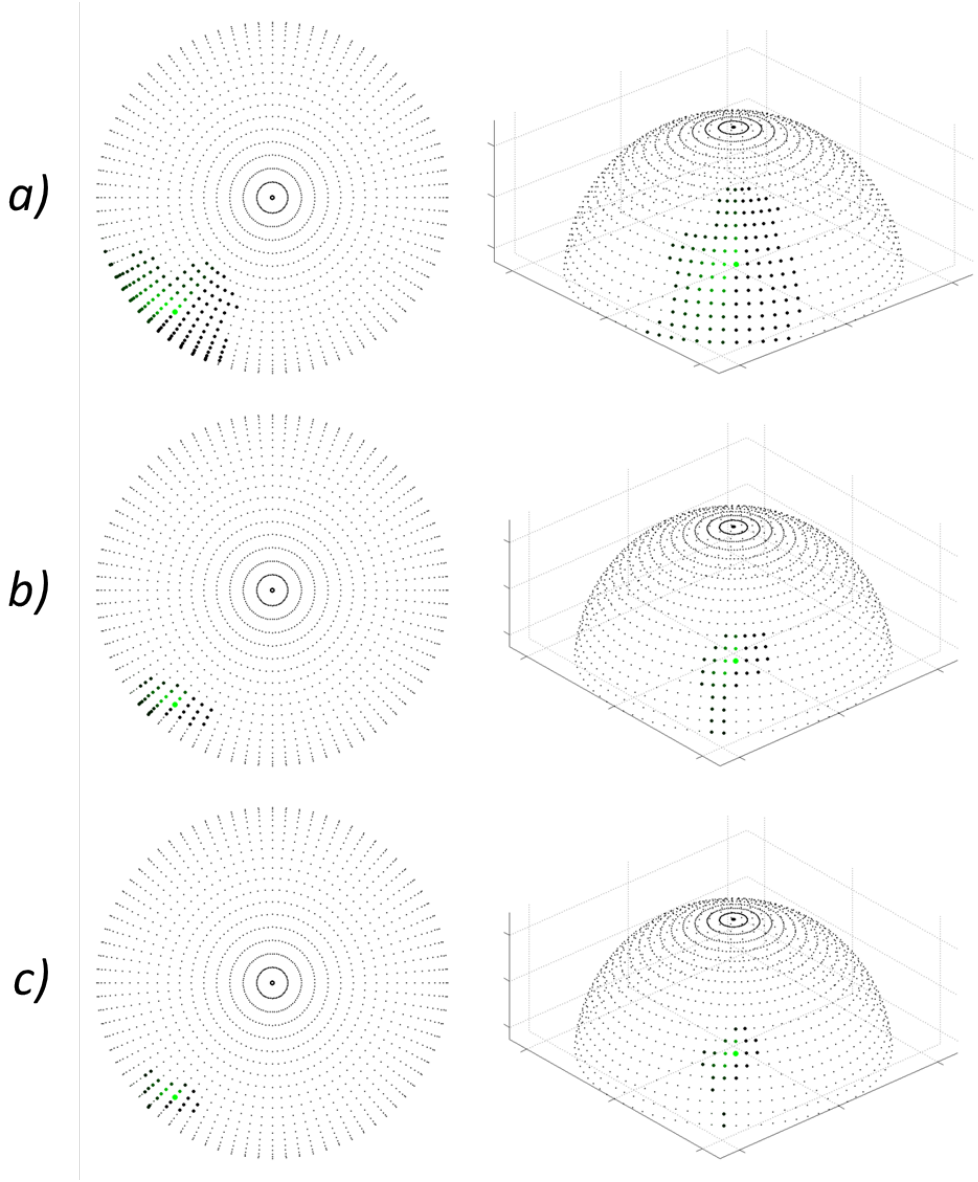

Figure 2.11: *EEG activation map with SSLOFO elaboration. Voxels are distributed on a semi-spherical surface in a conductive volume constituted by concentric spheres modeled by BEM. Voxels are shown in 3D space (figures on the right) and viewed from the top (figures on the left). Results are obtained at various passes of SSLOFO workflow: a) solution provided only by sLORETA, b) after one SSLOFO iteration, and c) after five SSLOFO iterations. Data in each configuration are normalized to the maximum value.*

Chapter 3

Brain Electrical Impedance Tomography

Electrical Impedance Tomography (EIT) [8][52] is a non-invasive imaging technique based on the application of current (*voltage*) patterns to the surface of a body and measuring the electrical potentials (*currents*) on the surface to estimate the impedance distribution inside the body. To retrieve meaningful insights from these measurements, EIT relies on detailed knowledge of the underlying electrical properties of the body. This is obtained from numerical models of current flows therein. The inhomogeneous and anisotropic electric properties of human tissues make accurate modeling and simulation very challenging, leading to a trade-off between physical accuracy and technical feasibility, which currently severely limits the capabilities of EIT.
In this Chapter, EIT computational issues are presented and discussed, introducing our new parallel algorithmic flow for an accurate EIT modeling environment featuring high anatomical fidelity with a spatial resolution equal to that provided by an high resolution MRI. This parallel formulation is explicitly aimed at an implementation on multi-core computing devices, in order to obtain low execution times without affecting resolution or introducing over-simplifications to reduce computational complexity (e.g. isotropic conductivities of the tissues or ideal electrodes).

3.1 EIT Medical Applications

Several studies address the development of instrumentation and software platforms to apply EIT to various biomedical fields. Some of these include the monitoring of pulmonary ventilation (the *Sheffield data collection system* [53]), the detection of breast tumors and the reconstruction of brain activity

[13].
The first commercial clinical solution for pulmonary ventilation monitoring has been announced [54], while the use of EIT in brain analysis and monitoring is still in the research stage, particularly to localize well defined regions of the brain such as epileptic foci, local ischemia and lesions. EIT can be used either to gather static, structural information (absolute imaging) to localize regions characterized by electrical properties that are different with respect to the surrounding tissues, or to monitor time variations of such properties (relative imaging) to enable monitoring of, e.g., blood distribution and perfusion alterations, that are correlated to brain activity.

3.2 EIT Forward and Inverse Problem

As introduced in Chapter 1.1.2, the computational workflow of EIT can be divided in two main parts: forward and inverse problem.
The forward problem is defined as the determination of the voltage distribution in the volume under examination, given its electrical properties (local conductivity and permittivity) and Neumann boundary conditions (currents injected on the body surface)(fig. 3.1). Due to the complexity of the domain,

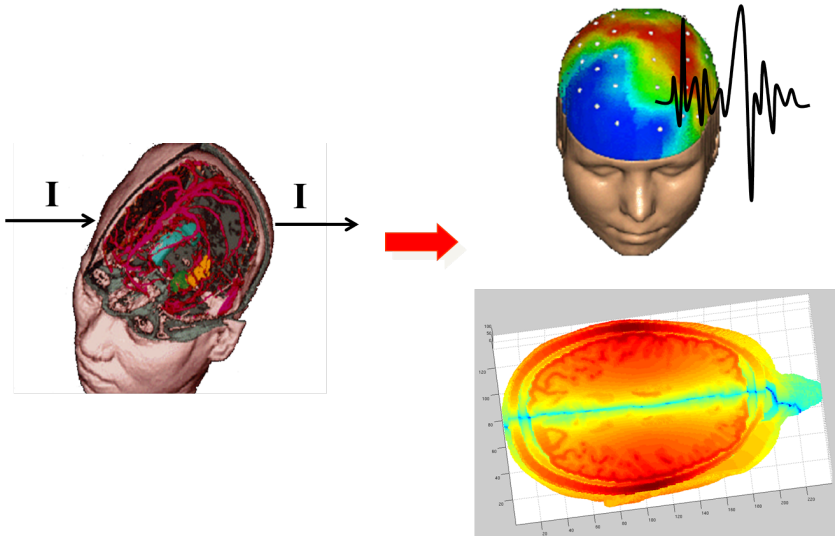

Figure 3.1: *EIT forward problem defines the relation between current patterns injected in the head volume (known its morphology and impedance distribution) and the resulting voltage distribution inside the volume.*

analytical solutions are not feasible, raising the need for numerical solvers. Accurate, fast and reliable forward problem simulation is crucial in order to

optimize EIT instrumentation, such that it maximizes the amount of information it is able to retrieve during usage.
Addressing the forward problem with a numerical method leads to a large sparse symmetric linear system, which can be solved using iterative methods, like the BiConiugate Gradient Method (BiCG).

On the other hand, the inverse problem is defined as the estimation of the impedance distribution in the volume under examination, given the electrode measurements and the relation between the voltage and impedance distribution retrieved by solving the forward problem (fig. 3.2). Given the relative small number of passive electrodes (generally ranging from 32 to 256) compared to the number of voxels (in our work-flow equal to high resolution MRI scans, so more than 5 millions), this problem is highly under-determined yielding a large number of possible solutions. Therefore, the best one can do is calculating an estimation, taking into account *a-priori* information in order to come up with a maximally realistic and physiologically correct solution.
Mathematically, under-determined systems can be solved using numerical approach as the *Least SQuared Residuals Method* (LSQR) using regularization techniques.

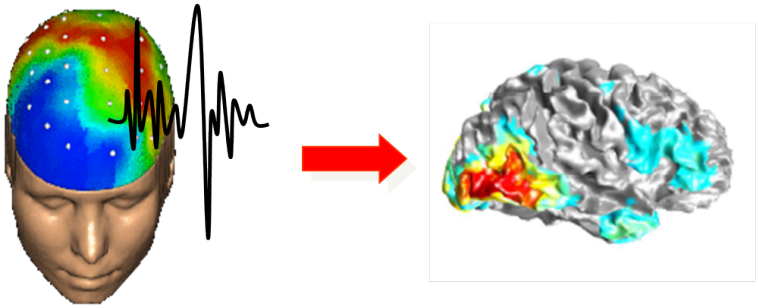

Figure 3.2: *EIT inverse problem. Electrode potentials are elaborated to obtain the impedance distribution map inside the brain, e.g. to highlight relevant local changes of conductivity.*

3.3 EIT Forward model: main issues

Formulation of the forward problem derives directly from the Poisson problem under quasi-static conditions [52] with Neumann boundary conditions depending on the injecting electrodes:

$$\begin{cases} -\nabla \cdot \boldsymbol{\sigma}^* \nabla\varphi &= 0 & on\ \Omega \\ \boldsymbol{\sigma}^* \nabla\varphi \cdot \hat{\boldsymbol{n}} &= \boldsymbol{g} \cdot \hat{\boldsymbol{n}} & on\ \partial\Omega \end{cases} \tag{3.1}$$

where φ is the voltage potential inside the volume Ω, $\mathbf{g}$ is the local current density injected at the surface $\partial\Omega$, $\hat{\boldsymbol{n}}$ is the unit vector normal to the surface, $\boldsymbol{\sigma}^*$ is the complex conductivity tensor of the medium defined as $\boldsymbol{\sigma}^* = \boldsymbol{\sigma} + j\omega\boldsymbol{\epsilon_r}\epsilon_0$ with $\boldsymbol{\sigma}$ representing the real conductivity tensor, $\boldsymbol{\epsilon_r}$ indicating the relative permittivity tensor of the medium and ω is $2\pi f$ with f frequency. The tensorial formulation is necessary in order to respect the anisotropy of conductivity in some tissues, e.g. white matter, as explained in Chapter 3.4.3.

This general formulation does not take into account the effects from contact impedance between the electrode metallic plate and adjacent skin, so a more advanced electrode model is necessary to make the model more realistic. The most common approach is the Complete Electrode Model (CEM), which takes into account both electrode size and contact impedance between the skin and conductive plate [55]. Considering the CEM for a set of L electrodes, problem 3.1 can be reformulated as:

$$\begin{cases} -\nabla \cdot \boldsymbol{\sigma}^* \nabla\varphi & = 0 & & on\ \Omega \\ \iint_{S_i} \boldsymbol{\sigma}^* \nabla\varphi \cdot \hat{\boldsymbol{n}}\, \mathrm{d}S & = \iint_{S_i} \boldsymbol{g} \cdot \hat{\boldsymbol{n}}\, \mathrm{d}S = I_i & & with\ i = 1, 2, \ldots, L \\ \boldsymbol{\sigma}^* \nabla\varphi \cdot \hat{\boldsymbol{n}} & = 0 & & on\ \partial\Omega / \bigcup_{i=1}^{L} S_i \\ \varphi + z_i \boldsymbol{\sigma}^* \nabla\varphi \cdot \hat{\boldsymbol{n}} & = U_i & & with\ i = 1, 2, \ldots, L \end{cases} \tag{3.2}$$

where I_i is the current injected at the i-th electrode of area S_i and U_i is the electrode voltage that also depends on the electrode contact impedance per unit surface z_i. The application of such models is often limited by the accompanying increase in complexity.

3.3.1 State of the art

For brain imaging application, the domain Ω is the volume enclosing the head of the patient and is characterized by the local complex conductivities of the different voxels, which influence the distribution of the electric field inside the head when currents are applied on its surface. Detailed knowledge of these physical parameters has a strong impact on the applicability of the overall methodology. For example, one of the prevalent limiting factors in EIT-based brain imaging is the presence of the skull, which is characterized by a low radial conductivity compared to the scalp thus acting as a barrier that limits the penetration of current through the brain. Considering the typical case of an epileptic focus of about 1 cm^3 diameter with a local

conductivity variation of 10% [56], an injected current of 100 μA can evoke variations as small as 10-50 μV on the electrodes, about 1000 times smaller than the reference potentials. Horesh et al. [12] show how a high change of conductivity introduced by ischemic or hemorrhagic tissues (up to 75%-750%) in the brain results in recorded voltage variations at the scalp between 2% and 7%.
In general, volumetric meshes are derived from MRI scans of the volume under examination. For example, EIDORS3D, an open source EIT simulation environment for MATLAB® [57], uses a finite element approach (FEM) to solve the forward problem; other solutions based on the Boundary Element Method (BEM) have also been presented [58]. Unfortunately, these approaches cannot exploit the richness of details provided by modern MRI/DTI equipment and have to introduce drastic simplifications. In fact, a 3 Tesla MRI instrument for clinical practice can provide images with a resolution of 1 mm^3, while other research instruments are able to use magnetic fields of up to 7T and 9.4T [3], obtaining a resolution higher than 0.05 mm^3 [4]. These hardware improvements increase demand for computational power as more detailed models are necessary to fully utilize the higher spatial resolution. At the state of the art, the commonly used FEM solutions require a preliminary step of mesh generation, which is not only very time-consuming, but also limits the final number of nodes to a resolution typically one or two orders of magnitude lower than the MRI resolution. Time necessary for mesh generation is influenced by the number of tissues to be considered in the volume, becoming a critical process where tissues are extremely thin. What is more, usage of unstructured meshes leads to the generation of a large sparse linear system, whose solution on regular multi-core platforms is affected by a severe overhead in the data handling, typically coped with by introducing simplifications on the model (e.g. by assuming isotropic conductivity).

The presented framework deals with this issue by using a finite volume approach (FVM) with a mesh composed of identical cubic voxels directly mapped on the DTI-MRI image voxels; it thus avoids interpolation and generation of complex unstructured meshes. This allows the forward model to exploit the full resolution given by DTI-MRI, leading to the generation of a banded linear system that can be efficiently solved on parallel multi-core machines using iterative linear system solvers. The simulations presented in this work are based on 3T MRI images with 1 mm^3 voxel size, a resolution 10-100 times larger than other available solutions [59][60]. Using a standard workstation equipped with low-cost GPUs, we are able to solve the problem in about 30 seconds.

3.4 EIT Forward Model: Finite Volume Implementation

In our framework, a patient-specific physical domain is generated from 3T MRI images obtained from the IXI database with a voxel resolution of 0.94 x 0.94 x 1.20 mm [61], resulting in a head volume of around 10 million voxels. White matter anisotropy is modeled from a DTI scan with a resolution of 2x2x2 mm in 7 directions.

3.4.1 Voxel classification

Since the geometric properties of head tissue, and in particular internal boundary regions, deeply influence scalp potentials [62], MRI images are segmented and labeled to obtain a realistic volume composed of five different tissue types, namely scalp, skull, CSF, gray matter and white matter. For this, we employed "BrainSuite" [63], an open-source automated cortical extraction tool. This tool performs a graphical elaboration of MRI images

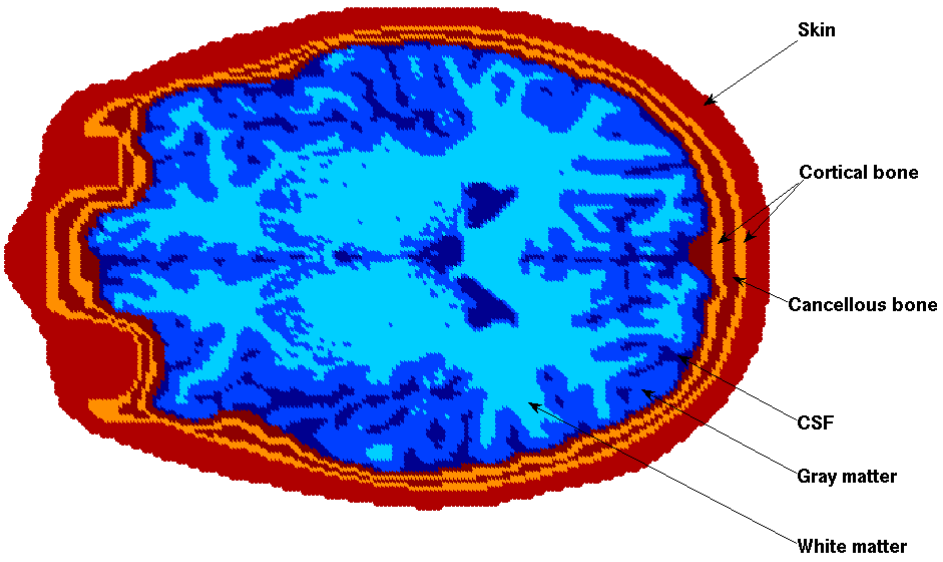

Figure 3.3: *Segmented MRI slice. Each voxel is classified according to the associated tissue. Skull is segmented in his three main tissues (cortical-cancellous-cortical bone layers).*

using reference to a brain atlas, resulting in equivalent segmented images where each voxel is classified according to the associated tissue. This operation results in a classification of all the voxels of the MRI image in the five aforementioned tissue types, maintaining the full resolution provided by the MRI scans (fig. 3.3). Migrating to different or more detailed segmentations would not introduce overhead in the successive forward problem definition, nor would it require a new mesh generation. As explained in Chapter 3.4.3, we perform an ulterior segmentation process for the skull to identify his three main tissues, i.e. the cortical-cancellous-cortical bone layers.

3.4.2 Electrical properties of tissues

Complex conductivity values for frequencies between 10Hz and 10MHz are derived from Gabriel et al. [64][65][66]. Table 3.1 and Table 3.2 show the real conductivities and the relative permittivity of the corresponding tissue types.

Frequency (Hz)	10	100	1 K	10 K	100 K	1 M	10 M
Skin (S/m)	0.434	0.434	0.450	0.5	0.5	0.8	1
Cortical bone	0.006	0.006	0.006	0.006	0.008	0.009	0.010
Cancellous bone	0.06	0.06	0.06	0.06	0.08	0.09	0.10
Csf	2	2	2	2	2	2	2
Gray matter	0.333	0.333	0.333	0.333	0.333	0.333	0.333
White matter	0.142	0.142	0.142	0.142	0.142	0.142	0.142

Table 3.1: *Real conductivity of the head tissues.*

Frequency (Hz)	10	100	1 K	10 K	100 K	1 M	10 M
Skin (x10^6)	1	0.5	0.4	0.1	0.05	0.005	10^{-4}
Cortical bone (x10^4)	5.5	0.58	0.27	0.05	0.02	0.01	0.003
Cancellous bone (x10^5)	100	2.1	0.1	0.01	0.004	0.002	10^{-4}
Csf	110	110	110	110	110	110	108
Gray matter (x10^5)	500	50	1	0.1	0.05	0.01	0.005
White matter (x10^5)	500	10	1	0.1	0.01	0.005	0.001

Table 3.2: *Relative permittivity of the head tissues.*

It is important to highlight that the real conductivity of the outermost structures (skin, cortical and cancellous bone) changes significantly with frequency, while the conductivity of internal tissue types remains practically

constant; relative permittivity is notably frequency-dependent for all tissue types.

3.4.3 Tissue anisotropy

Anisotropic conductivity of the head tissues is particularly significants for the skull and the white matter. This is due to the morphological structure of them, while more homogeneous tissues like gray matter, skin and CSF can be considered isotropic.

Anisotropy of the skull

The anisotropic behavior of the skull derives from its three-layered structure, with the internal layer (cancellous bone) being about ten times more conductive than the surrounding ones (cortical bone) [67]. This is due to the higher concentration of blood in the cancellous bone than in the cortical shell. The external cortical bone layers thus act as a barrier, limiting the current flow in the surrounding cancellous bone layer, where currents assume a complex distribution due to the presence of the most internal cortical bone layer. When considering the skull as an unique layer, it becomes necessary to have an anisotropic description of its conductivity; more precisely, skull voxels are modeled to be around 10 times less conductive in directions normal to the skull surface as opposed to tangential directions. Considering the three adjacent squared layers of fig. 3.4, with size WxW and thickness $t_1/2$, t_2 and $t_1/2$ respectively, with for simplicity real conductivity σ_1 and σ_2 ($\sigma_2 \approx 10\sigma_1$), a conductivity vector can be evaluated along the local spatial Cartesian directions given a current flowing along the normal direction $\hat{n}$ at the structure:

$$\begin{cases} \sigma_t &= t_2\sigma_2 + t_1\sigma_1 \\ \sigma_b &= t_2\sigma_2 + t_1\sigma_1 \\ \sigma_n &= W^2(\frac{\sigma_1\sigma_2}{\sigma_2 t_1 + \sigma_2 t_2}) \end{cases} \tag{3.3}$$

A 3x3 symmetric tensor is then derived from this vector, performing a spatial rotation on each voxel of the skull to convert all data in a common base coordinates system.
However, it has been demonstrated that a model based on isotropic layers is more accurate and realistic than one based on a single anisotropic layer [68]. In fact, as previously introduced, skull anisotropy is due to its layered structure when it is managed as a single region. Since our mesh is detailed enough to allow this approach, we model the skull in our framework as a

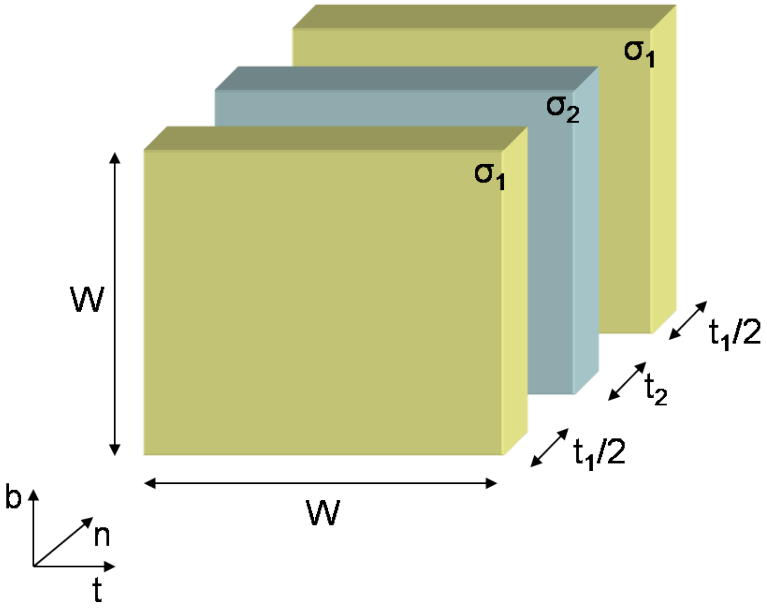

Figure 3.4: *Three layered model of the skull.*

three layered (cortical-cancellous-cortical bone) isotropic structure.

Anisotropy of the white matter

White matter structure is based on fibers whose thickness is often smaller than MRI resolution. They act as a connection network between neurons in the gray matter and the other parts of the nervous system. Current flow is "deviated" along the parallel direction to the fibers axes (fig. 3.5), resulting in a conductivity ratio between normal and parallel direction to the fiber axes which has been estimated to be around 1:9 [69]. A multi-layer approach cannot be used for white matter because fibers have a complex distribution, which can not be modeled using simple structures as adjacent layers, as can be verified visualizing a map of the Fractional Anisotropy (FA) distribution in the volume (fig. 3.6). FA is a index of the degree of the anisotropy of a medium commonly used in brain imaging; a FA value is associated at every voxels and it is computed from associated conductivity tensor. Considering for simplicity real values, a conductivity tensor $\boldsymbol{\sigma}$ can be expressed as a diagonal matrix $\boldsymbol{S}$ defining conductivity values λ_1, λ_2 and λ_3 along the directions of a local coordinates system, opportunely rotated in

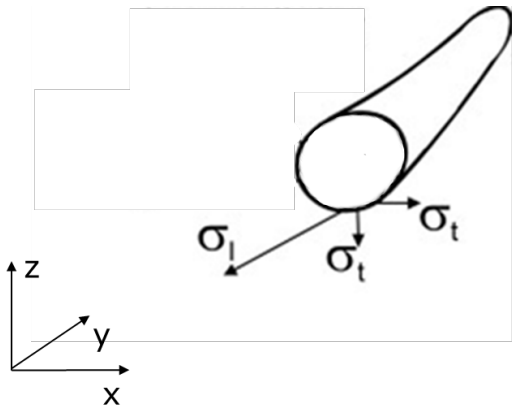

$$\boldsymbol{\sigma} = \mathbf{R^T} \begin{pmatrix} \sigma_l & 0 & 0 \\ 0 & \sigma_t & 0 \\ 0 & 0 & \sigma_t \end{pmatrix} \mathbf{R}$$

Figure 3.5: *Anisotropic conductivity of WM fibers; at each white matter voxel is associated a diagonal conductivity tensor expressing conductivity along directions defined by a local reference system referred to the generic fiber. Then data are ported in the common reference system by an algebraic rotation.*

the common global reference system by a rotation matrix $\mathbf{R}$:

$$\boldsymbol{\sigma} = \boldsymbol{R}^T \begin{pmatrix} \lambda_1 & 0 & 0 \\ 0 & \lambda_2 & 0 \\ 0 & 0 & \lambda_3 \end{pmatrix} \boldsymbol{R} = \boldsymbol{R}^T \boldsymbol{S} \boldsymbol{R} \tag{3.4}$$

Being $\mathbf{R}$ a simple rotation matrix, eigenvalues λ_i are preserved in the transformation. In the particular case of a white matter fiber (fig. 3.5) at each voxel is associated a diagonal tensor given by local conductivity along the parallel and normal directions to the target fiber axis, which becomes a full symmetric tensor when it is rotated in the common global reference system. Known $\boldsymbol{S}$ (or equivalently $\boldsymbol{\sigma}$), FA is computed as followed:

$$FA = \sqrt{\frac{3}{2}\left(\frac{(\lambda_1 - \bar{\lambda})^2 + (\lambda_2 - \bar{\lambda})^2 + (\lambda_3 - \bar{\lambda})^2}{\sum_{i=1}^{3} \lambda_i^2}\right)} \tag{3.5}$$

where $\bar{\lambda}$ is the mean of eigenvalues. FA is equal to zero in isotropic medium ($\lambda_i = \bar{\lambda}$), while it increases when anisotropy degree is higher. In fig. 3.6 FA distribution is shown for three head slices: bright pixels represent voxels where anisotropy is high; they are practically concentrated in the white matter area. It is important to highlight how respects to white matter, the other tissues can be considered isotropic (FA is practically zero). This confirms the layered approach used to model skull properties, because in that case the anisotropic behavior is due to the approximation of modeling skull as

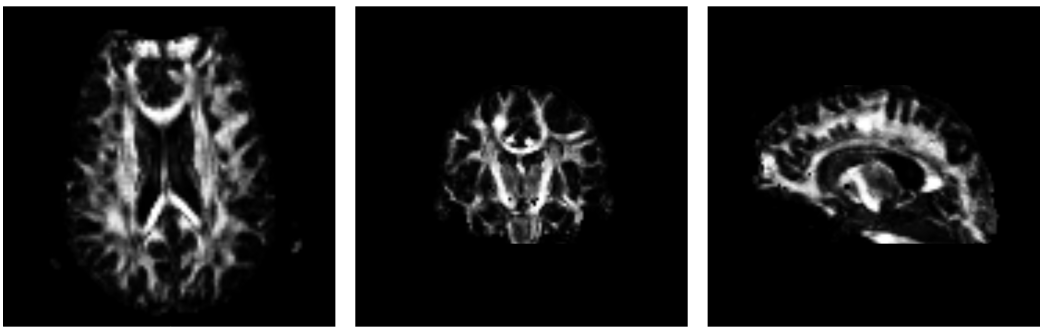

Figure 3.6: *FA distribution on three head slices. FA is a measure of the anisotropy degree. High FA voxels (bright pixels) are concentrated in white matter areas, while in others regions voxels are practically isotropic (black pixel, low FA).*

an unique layer, while in reality cortical and cancellous bone are isotropic if taken individually.
Anisotropic conductivity maps of white matter can be derived from DTI scans. As mentioned before, DTI is a brain imaging technique providing images representative of the water diffusion in the tissues (Chapter 1.1.1). Water diffusion in white matter is influenced by its fibrous structure, and consequently it is possible to reconstruct its morphological structure from DTI elaboration. In our framework, DTI images are processed by *MedINRIA* [70], an open source toolbox which allows to extract water molecule diffusion tensors for each voxel. These are linearly related to the conductivity tensors [71]. Fig. 3.7 shows an example of a 3D white matter reconstruction as obtained in our framework. Each water diffusion tensor $\mathbf{V}$ extracted is composed of the following factors:

$$\boldsymbol{V} = \boldsymbol{R}^{\mathrm{T}} \boldsymbol{D} \boldsymbol{R} \tag{3.6}$$

where $\mathbf{D}$ is a diagonal matrix with its eigenvalues representing the diffusion coefficients in the local reference system of the associated fiber, and $\mathbf{R}$ is given by the eigenvectors representing the rotational matrix with respect to the global coordinate system. Diffusion coefficients are given by fibers structure, so they can be related to the conductivity coefficients of $\boldsymbol{S}$ (eq. 3.4). $\mathbf{D}$ is scaled by its trace and multiplied by the isotropic white matter conductivity (σ^{iso}); in this way the tensor matches the isotropic electrical properties when $\boldsymbol{R}$ is an identity matrix:

$$\boldsymbol{\sigma}^{*} = \boldsymbol{R}^{\mathrm{T}} \cdot \sigma^{iso} \frac{\boldsymbol{D}}{3 \cdot tr(\boldsymbol{R})} \cdot \boldsymbol{R} \tag{3.7}$$

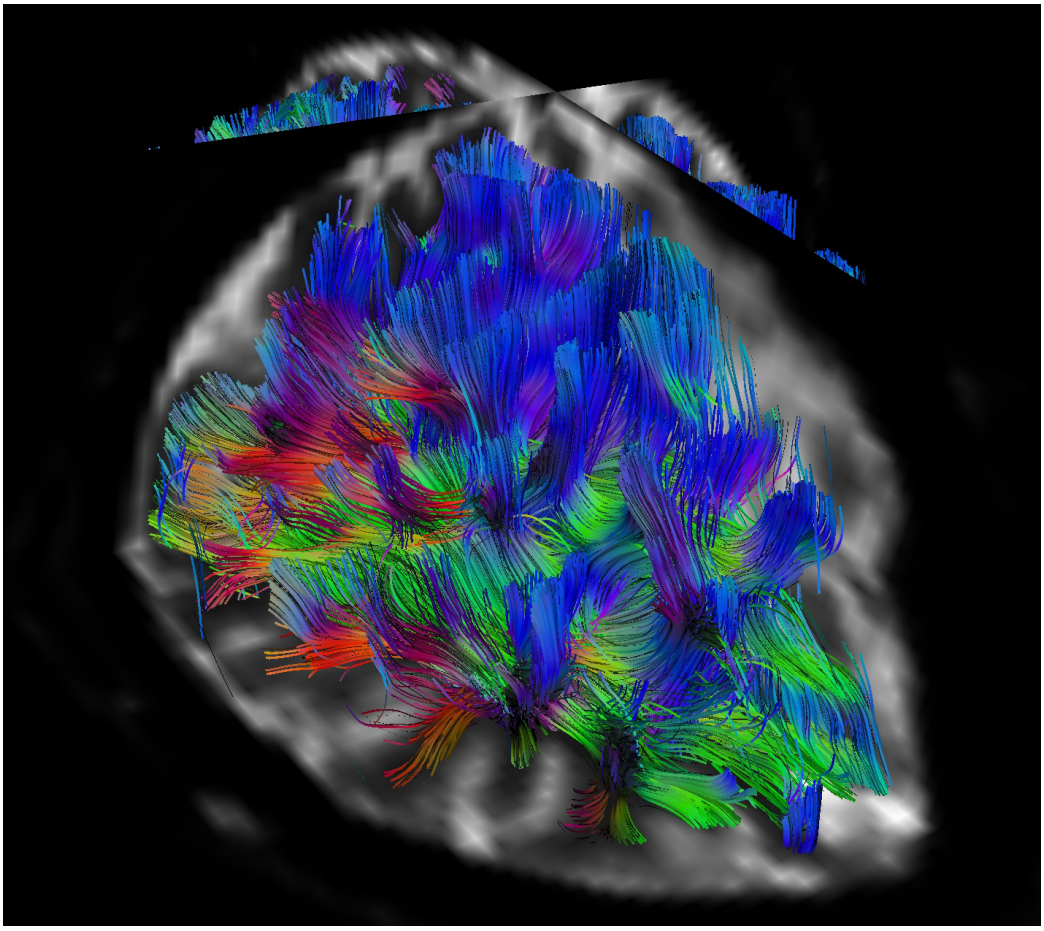

Figure 3.7: *3D white matter fiber reconstruction obtained by processing DTI scans of the subject.*

3.4.4 Numerical model

The numerical solver is based on the FVM formulation for EEG field potentials computation described in [72]. Each cubic voxel is characterized by a constant complex conductivity tensor, so the discretization of volume Ω is a cubic grid with a piecewise constant conductivity tensor distribution. This makes it possible to solve the Poisson problem locally on each corner (node) of the voxels. The method is based on evaluation of current flux given by the field in examination on the oriented surfaces defined by nodes, so it is necessary to convert the Poisson problem to its equivalent integral form. By integrating the first equation of problem 3.2 on the surface of each voxel and

applying the divergence theorem, we obtain:

$$-\iint_{S_i} \boldsymbol{\sigma}^* \nabla\varphi \cdot \hat{\boldsymbol{n}}\, \mathrm{d}S = \iiint_V \nabla \cdot \boldsymbol{g}\, \mathrm{d}V = \iiint_V I_V\, \mathrm{d}V \tag{3.8}$$

where S is the surface of each cubic volume, V is its volume, $\boldsymbol{g}$ and I_V are the vector current density and volumetric current density respectively, which are nonzero only on nodes where currents are injected. Equation 3.8 is applied locally to every volume, with potential gradients expressed as finite differences at the nodes. Evaluation of the electric flux is performed adding a control volume for each point of the grid, but this does not increase the number of points of the resulting problem. The FVM is flux continuous, meaning that current continuity is satisfied over the entire domain.
For better clarity, the finite volume solution to eq. 3.8 will be derived in 2D. This can then be easily extended to the 3D case.

2D formulation

In 2D case, voxels and control volumes are squared elements of size hxh. Referring to an MRI volume, squared voxels in the 2D case represents pixels of a single MRI slice. The conductivity tensor for each voxel is defined as a symmetric 2x2 matrix:

$$\boldsymbol{\sigma}^* = \begin{pmatrix} \sigma^{xx} & \sigma^{xy} \\ \sigma^{xy} & \sigma^{yy} \end{pmatrix} \tag{3.9}$$

Control volumes are squared elements centered on each grid points; they defines the surface of integration for each grid point necessary to evaluate the electric flux of eq. 3.8. In fact considering the grid point "5" of fig. 3.8, where four adjacent voxels of different conductivity share this point, to evaluate electric flux around this is necessary to consider a control volume centered on it. Applying eq. 3.8 at the point "5" and considering the intersection points of control volume and the voxels, it results:

$$-\Big((\boldsymbol{\sigma}^*\nabla\varphi\cdot S^x)_e - (\boldsymbol{\sigma}^*\nabla\varphi\cdot S^x)_w + (\boldsymbol{\sigma}^*\nabla\varphi\cdot S^y)_n - (\boldsymbol{\sigma}^*\nabla\varphi\cdot S^y)_s\Big) = I_V h^2 \tag{3.10}$$

where S^x and S^y are the normal vectors for the faces of the control volume and are defined as $S^x = [h\ 0]^T$ and $S^y = [0\ h]^T$.
Eq. 3.10 states the principle of charge conservation, representing total current flowing at the control volume sides, which is different from zero only with an external current injection, so in case of "5" is considered a point surrounding an active electrode. Each terms of this equation can be evaluated considering a linear distribution of the electric potential and expressing the potential gradients in terms of finite difference between the grid points. In particular

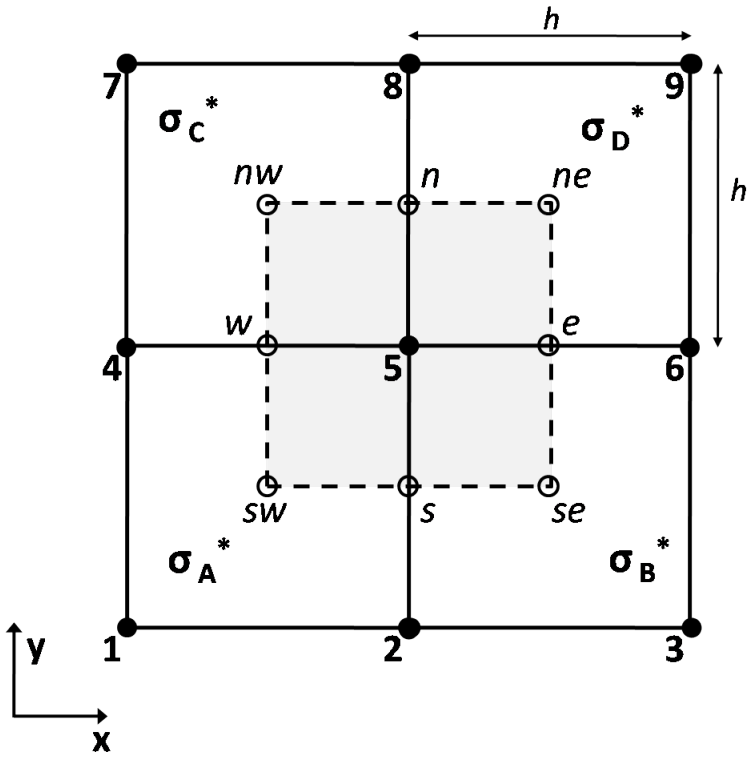

Figure 3.8: *Four squared adjacent voxels with different complex tensor conductivity with a common corner ("5"); to evaluate eq. 3.8 on it a control volume is added (in gray). His intersection with the voxels defines eight further points (n,ne,e,se,s,sw,w,nw) which are used in the formulation of the discretized problem, but without adding them in the solutions space.*

considering the right side e of the volume, flowing current density can be split in two terms:

$$(\boldsymbol{\sigma}^* \nabla\varphi \cdot S^x)_e = \boldsymbol{\sigma}^* \nabla\varphi^B \cdot \frac{S^x}{2} + \boldsymbol{\sigma}^* \nabla\varphi^D \cdot \frac{S^x}{2} \tag{3.11}$$

where $\nabla\varphi^B$ and $\nabla\varphi^D$ are potential gradients evaluated at the face e towards the voxels B and D respectively. Gradients can be approximated with finite differences:

$$\nabla\varphi^B = \begin{pmatrix} (\varphi_6 - \varphi_5)/h \\ (\varphi_e - \varphi_{se})/(h/2) \end{pmatrix} \tag{3.12}$$

$$\nabla\varphi^D = \begin{pmatrix} (\varphi_6 - \varphi_5)/h \\ (\varphi_{ne} - \varphi_e)/(h/2) \end{pmatrix} \tag{3.13}$$

Hypothesizing a linear distribution of potential in the voxels:

$$\begin{aligned} \varphi_e &= (\varphi_6 + \varphi_5)/2 \\ \varphi_{se} &= (\varphi_2 + \varphi_3 + \varphi_5 + \varphi_6)/4 \\ \varphi_{ne} &= (\varphi_5 + \varphi_6 + \varphi_8 + \varphi_9)/4 \end{aligned} \tag{3.14}$$

Substituting eq. 3.14 into eq. 3.12 and eq. 3.13, the final expression of the density of current flowing on face e becomes:

$$\begin{aligned} (\boldsymbol{\sigma}^* \nabla\varphi \cdot S^x)_e = &\frac{\sigma_B^{xx} + \sigma_D^{xx}}{2}(\varphi_6 - \varphi_5) \\ &+ \frac{\sigma_B^{xy}}{4}[(\varphi_5 - \varphi_6) - (\varphi_2 + \varphi_3)] \\ &+ \frac{\sigma_D^{xy}}{4}[(\varphi_8 - \varphi_9) - (\varphi_5 + \varphi_6)]. \end{aligned} \tag{3.15}$$

Applying eq. 3.15 at each faces of the control volume, eq. 3.8 can be simplified in the following linear equation:

$$\sum_{i=1}^{9} A_i \varphi_i = I_V h^2 \tag{3.16}$$

where coefficients A_i are:

$$\begin{aligned} A_1 &= -\frac{1}{2}\sigma_A^{xy}, \\ A_2 &= -\frac{1}{2}(\sigma_A^{yy} + \sigma_B^{yy}), \\ A_3 &= -\frac{1}{2}\sigma_B^{xy}, \\ A_4 &= -\frac{1}{2}(\sigma_A^{xx} + \sigma_C^{xx}), \\ A_6 &= -\frac{1}{2}(\sigma_B^{xx} + \sigma_D^{xx}), \\ A_7 &= -\frac{1}{2}\sigma_C^{xy}, \\ A_8 &= -\frac{1}{2}(\sigma_C^{yy} + \sigma_D^{yy}), \\ A_9 &= -\frac{1}{2}\sigma_D^{xy}, \\ A_5 &= -\sum\nolimits_{i=1, i\neq 5}^{9} A_i. \end{aligned} \tag{3.17}$$

3D formulation

The 2D formulation can be extended to the 3D case, considering voxels and control volume as cubic elements of size hxhxh. To each voxel a 3x3 symmetric conductivity tensor is associated, which becomes a diagonal matrix in case of isotropic conductivity:

$$\boldsymbol{\sigma}^* = \begin{pmatrix} \sigma^{xx} & \sigma^{xy} & \sigma^{xz} \\ \sigma^{xy} & \sigma^{yy} & \sigma^{yz} \\ \sigma^{xz} & \sigma^{yz} & \sigma^{zz} \end{pmatrix} \tag{3.18}$$

Considering the point "10" of fig. 3.9, where eight cubic adjacent voxels share the common corner "10", an equivalent FVM formulation can be applied

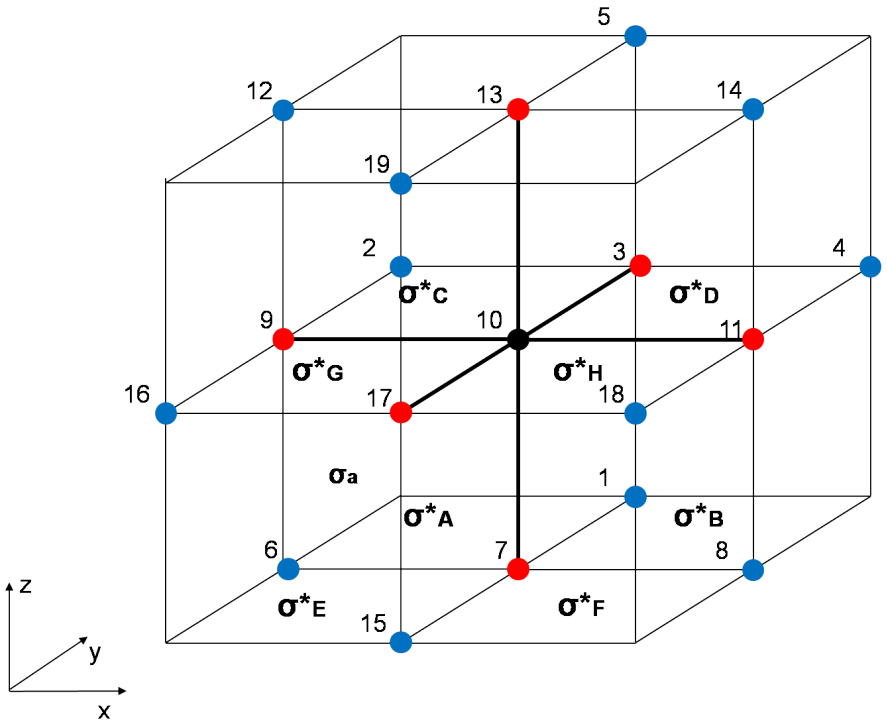

Figure 3.9: *Eight cubic adjacent voxels with different complex tensor conductivity with a common corner ("10"). To apply flux equation 3.8 at this point, it is necessary to express the potential gradients along the three directions of the space as finite differences between its adjacent points. In the case of isotropic conductivities of the volumes ($\boldsymbol{\sigma}^*$ diagonal matrix for all voxels), it is necessary to consider six points (red spots), while with anisotropic conductivities 19 points are necessary (red and blue spots).*

considering the 19 nodes highlighted. In case of isotropic conductivity only points along the three Cartesian directions of the space respect to point "10" (red spots) are to be taken in account. Therefore, the FVM discretized equation of the problem for the point "10" is:

$$\sum_{i=1}^{19} A_i \varphi_i = I_V h^2 \tag{3.19}$$

where coefficients A_i are:

$$\begin{aligned}
A_1 &= -\frac{1}{4}(\sigma_A^{yz} + \sigma_B^{yz}),\\
A_2 &= -\frac{1}{4}(\sigma_A^{xz} + \sigma_C^{xz}),\\
A_3 &= -\frac{1}{4}(\sigma_A^{zz} + \sigma_B^{zz} + \sigma_C^{zz} + \sigma_D^{zz}),\\
A_4 &= \frac{1}{4}(\sigma_B^{xz} + \sigma_D^{xz}),\\
A_5 &= \frac{1}{4}(\sigma_C^{yz} + \sigma_D^{yz}),\\
A_6 &= -\frac{1}{4}(\sigma_A^{xy} + \sigma_E^{xy}),\\
A_7 &= -\frac{1}{4}(\sigma_A^{yy} + \sigma_B^{yy} + \sigma_E^{yy} + \sigma_F^{yy}),\\
A_8 &= \frac{1}{4}(\sigma_B^{xy} + \sigma_F^{xy}),\\
A_9 &= -\frac{1}{4}(\sigma_A^{xx} + \sigma_C^{xx} + \sigma_E^{xx} + \sigma_G^{xx}),\\
A_{11} &= -\frac{1}{4}(\sigma_B^{xx} + \sigma_D^{xx} + \sigma_F^{xx} + \sigma_H^{xx}),\\
A_{12} &= \frac{1}{4}(\sigma_C^{xy} + \sigma_G^{xy}),\\
A_{13} &= -\frac{1}{4}(\sigma_C^{yy} + \sigma_D^{yy} + \sigma_G^{yy} + \sigma_H^{yy}),\\
A_{14} &= -\frac{1}{4}(\sigma_D^{xy} + \sigma_H^{xy}),\\
A_{15} &= \frac{1}{4}(\sigma_E^{yz} + \sigma_F^{yz}),\\
A_{16} &= \frac{1}{4}(\sigma_E^{xz} + \sigma_G^{xz}),\\
A_{17} &= -\frac{1}{4}(\sigma_E^{zz} + \sigma_F^{zz} + \sigma_G^{zz} + \sigma_H^{zz}),
\end{aligned} \tag{3.20}$$

$$
\begin{aligned}
A_{18} &= -\frac{1}{4}(\sigma_F^{xz} + \sigma_H^{xz}), \\
A_{19} &= -\frac{1}{4}(\sigma_G^{yz} + \sigma_H^{yz}), \\
A_{10} &= -\sum\nolimits_{i=1, i\neq 10}^{19} A_i.
\end{aligned}
\tag{3.21}
$$

Iterating this formulation for each points results in a square banded linear system:

$$\boldsymbol{A\Phi} = \boldsymbol{I} \tag{3.22}$$

where $\boldsymbol{A}$ is a complex symmetric non-hermitian matrix, $\boldsymbol{\Phi}$ is the vector of the electric potential at each point of the discretized volume and $\boldsymbol{I}$ is a vector defining injected currents. Since all the voltages are defined only up to an additive constant, the resulting matrix is singular; the singularity is removed once an arbitrary reference voltage node is defined.
The matrix structure (fig. 3.10) is highly regular with a banded structure, with 7 diagonals for isotropic conductivities, 19 once anisotropy is taken into account. Each element $\boldsymbol{A}(i, j)$ physically represents an impedance between points i and j, so the discretized volume can be seen as an impedance network where nodes are defined by the grid points and the connections by the forward problem matrix. Matrix size is given by the number of points in the volume, this means around 10^7x10^7 for an high resolution MRI volume with a density (number of nonzero elements with respect to the total) of less than 0.001%.

Complete electrode model FVM implementation

Since Complete Electrode Model (CEM) requires non-standard boundary conditions, it cannot be straightforwardly implemented in commercial general purpose FEM packages [73]. Ignoring the effects introduced by finite electrodes leads to excessive approximations in the numerical model due to the following issues:

1. Finite size of electrodes which change the electric field distribution near the contact areas,

2. Finite contact impedance.

A solution based on direct introduction of the electrode structure in the volume is depreciable, because this leads to include regions with very high differences of conductivity (e.g. electrode metallic plate is practically a discontinuity in the conductivity distribution) increasing the conditioning number of the forward problem matrix $\boldsymbol{A}$. Therefore, a better solution is to

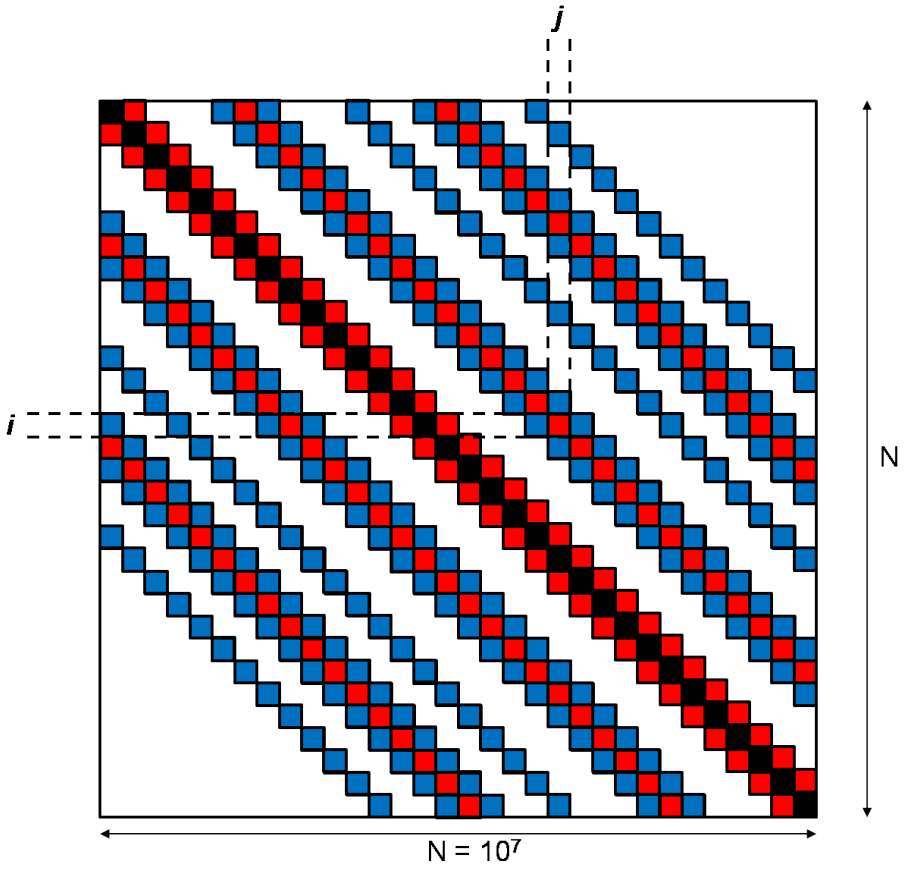

Figure 3.10: *Structure of the matrix* $\boldsymbol{A}$ *obtained with this framework. It is a square banded symmetric matrix of size N equal to the number of voxels in the MRI head volume. Red box elements are required in case of isotropic conductivity, the blue ones are required once anisotropy is taken into account.*

include the electrode properties described by CEM directly modifying matrix $\boldsymbol{A}$, adding ohmic connections between the points of interest.
Neglecting electrode thickness and integrating the fourth equation of pr. 3.2 on the i-th electrode area S_i we obtain:

$$\iint_{S_i} \varphi \, \mathrm{d}S + \iint_{S_i} z_i \boldsymbol{\sigma}^* \nabla\varphi \cdot \hat{\boldsymbol{n}} \, \mathrm{d}S = \iint_{S_i} U_i \, \mathrm{d}S \tag{3.23}$$

where the second integral represents the effect of the contact impedance on the voltage. Considering z_i and U_i constant on the electrode and combining eq. 3.23 with the second equation of pr. 3.2, the electrode voltage U_i is

expressed as:

$$\begin{aligned} U_i &= \frac{1}{S_i} \iint_{S_i} \varphi \, \mathrm{d}S + \frac{I_i z_i}{S_i} \\ &= \frac{1}{S_i} \iint_{S_i} \varphi \, \mathrm{d}S + I_i Z_c \end{aligned} \tag{3.24}$$

where I_i is the current flowing through the electrode and Z_c is the contact impedance. The voltage on the electrode results from the ohmic contact with the skin and from applying an averaging effect on the potentials at the contact. This can be achieved by directly connecting every skin point below the electrode to an unique point representing the electrode itself (fig. 3.11.a), although this alters the banded structure of the matrix introducing connections between non adjacent points, increasing the complexity for the numeric solver. In order to avoid this, we introduce a new CEM implementation based on the usage of additional nodes which make possible to link only adjacent points, following a tree structure where the root represents the electrode (fig. 3.11.b). This leads to a marginal increase in the matrix element number but preserves its banded structure. The impedance value assigned to every branch depends on its level in the tree and is determined in order to obtain an identical equivalent impedance Z_0 between any scalp point and the tree root. In the example of fig. 3.11.b, with all scalp points short-circuited, the current is split in equal parts at each point where branches diverge, so that the same amount of current reaches every scalp point. As an example, the skin point adjacent to the root is directly connected with an impedance $Z_0 = 1/G_0$, while the farthest ones are connected with an equivalent impedances network:

$$\frac{1}{2G_0} + \frac{1}{4G_0} + \frac{1}{8G_0} + \frac{1}{8G_0} = \frac{1}{G_0} = Z_0. \tag{3.25}$$

Z_0 is determined by computing the equivalent impedance Z_e between the tree root and the shorted nodes and imposing it to be equal to the expected contact impedance Z_c:

$$Z_e = \alpha Z_0 = Z_c \quad \Rightarrow Z_0 = Z_c/\alpha \tag{3.26}$$

Sensitivity analysis

EIT is often used in order to identify conductivity variations with respect to a reference situation. This happens for example in patient's monitoring: electrode potential variations are elaborated to localize significant changes in the impedance distribution respect to one taken as reference. A first immediate

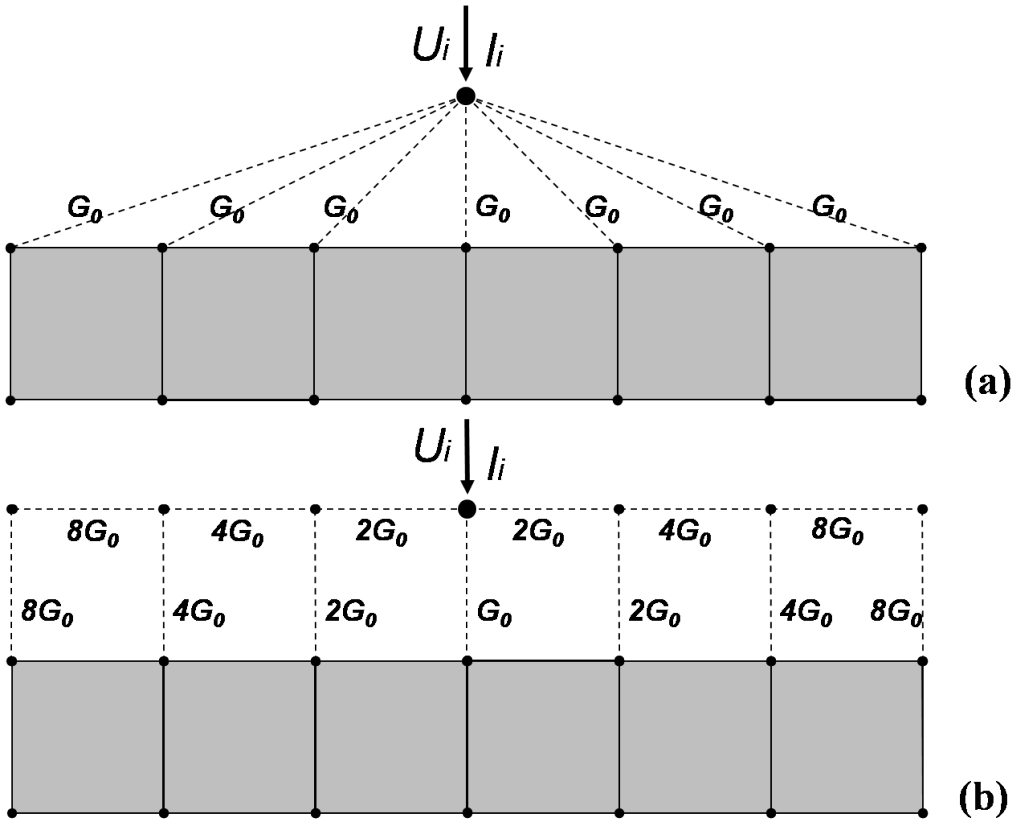

Figure 3.11: *Different electrode model implementations: a) Skin nodes are directly connected to the point representing the electrode. b) Skin nodes are connected with a tree structure using additional points. In both cases, an equivalent conductance G_0 is present between injecting point and any skin point.*

approach for this can be to evaluate impedance variations simply as difference of stand alone different solutions. From a computational point of view, this procedure can be source of errors and introduce unacceptable numerical noise levels, because electrode voltage variations are orders of magnitude smaller than the reference ones in the typical ranges of the signals involved in EIT analysis. Consequently, given a reference conductivity distribution $\boldsymbol{\sigma}_r^*$, a perturbed distribution $\boldsymbol{\sigma}_p^* = \boldsymbol{\sigma}_r^* + \Delta\boldsymbol{\sigma}^*$ and a current pattern $\boldsymbol{I}$ flowing in the electrodes, the evaluation of the potential variations $\Delta\boldsymbol{\Phi} = \boldsymbol{\Phi_p} - \boldsymbol{\Phi_r}$ as the difference between the potentials computed with the two conductivity distributions is affected by accumulation of the numerical errors of the two different solutions, which is not negligible because of the small difference between them.

For this reason we have implemented a sensitivity analysis approach to evaluate the effects of small changes of conductivity distribution in the head. Hence, to obtain a more robust solution and avoid to recompute matrix $\mathbf{A}$, we linearize the problem 3.22 around the reference point given by $(\boldsymbol{\sigma}_r^*, \boldsymbol{\Phi_r}, \boldsymbol{I})$. Expressing eq. 3.22 in the two different cases leads to the system:

$$\begin{cases} \boldsymbol{A}(\boldsymbol{\sigma}_r^*)\boldsymbol{\Phi}_r &= \boldsymbol{I} \\ \boldsymbol{A}(\boldsymbol{\sigma}_p^*)\boldsymbol{\Phi}_p &= \boldsymbol{A}(\boldsymbol{\sigma}_r^* + \boldsymbol{\Delta\sigma}^*) \cdot (\boldsymbol{\Phi}_r + \boldsymbol{\Delta\Phi}) = \boldsymbol{I} \end{cases} \tag{3.27}$$

with $\boldsymbol{I}$ constant. By construction:

$$\boldsymbol{A}(\boldsymbol{\sigma}_r^* + \boldsymbol{\Delta\sigma}^*) = \boldsymbol{A}(\boldsymbol{\sigma}_r^*) + \boldsymbol{A}(\boldsymbol{\Delta\sigma}^*) \tag{3.28}$$

Subtracting term by term the two equations of pr. 3.27 and considering eq. 3.28, we obtain:

$$\boldsymbol{A}(\boldsymbol{\sigma}_r^*) \cdot \boldsymbol{\Delta\Phi} + \boldsymbol{A}(\boldsymbol{\Delta\sigma}^*) \cdot \boldsymbol{\Phi}_r + \boldsymbol{A}(\boldsymbol{\Delta\sigma}^*) \cdot \boldsymbol{\Delta\Phi} = \mathbf{0} \tag{3.29}$$

This system of equations can be linearized around the reference point defined by $(\boldsymbol{\sigma}_r^*, \boldsymbol{\Phi_r}, \boldsymbol{I})$ with the hypothesis of small variations $\Delta\boldsymbol{\sigma}^*$, resulting in the following:

$$\boldsymbol{A}(\boldsymbol{\sigma}_r^*) \cdot \boldsymbol{\Delta\Phi} = -\boldsymbol{A}(\boldsymbol{\Delta\sigma}^*) \cdot \boldsymbol{\Phi}_r \tag{3.30}$$

Equation 3.30 shares the same matrix $\boldsymbol{A}$ of the original problem 3.22, so obtained linear system does not neither require any modification in our parallel multi-core solver (Chapter 3.4.5) nor any re-computation of $\boldsymbol{A}$. Right hand side now is evaluated as function of the reference solution and $\boldsymbol{\Delta\sigma}^*$.

3.4.5 Forward problem parallel multi-core solving

This section has been included for the purpose of demonstrating the practical feasibility of this work, while algorithmic details and performances achieved are shown in Chapter 4.2.3. As described in Chapter 3.4.4, our work flow involves the solution of a large linear system, based on a 19-band complex coefficient matrix $\mathbf{A}$ with a size in the order of few millions for a standard 3 T scan with 1 mm^3 voxel size. Direct solution of such a system is not feasible, suggesting the use of iterative solvers; still, the complexity and sheer magnitude of the problem make this step a serious bottleneck in the work flow. Using standard numerical software on a common desktop machine, this process can take hours, severely limiting the practical use of our procedure. However, we were able to drastically reduce computation times down less of a minute using our own hardware-accelerated solver specifically designed for this purpose. Its design will be outlined in Chapter 4.2.3.

Considering the non-hermitian properties of matrix **A**, the Bi-Conjugate Gradient Method (BiCG) was found to be the best approach to address this problem; between this method and the alternatives we tested (Minimum and Generalized Minimum Residual, CG Squared, Least Squares, BiCG Stabilized [74]), BiCG showed the fastest convergence rate for our problem class.

3.5 EIT Forward Model: Simulations and Results

In order to provide the practical feasibility of this work and to show as this EIT forward problem simulation environment can be used for the design and characterization of the acquisition hardware, we have performed a parametrical analysis of the obtained system.
All computation flow is performed with complex floating point data in double precision. The model has been previously validated by comparing the results to an analytical reference in simplified volumes based on concentric spherical models. All of the following analyses have been performed considering conductivity variations which are compatible with biological processes, such as epileptic seizures [56]. Injected current amplitudes, frequencies and readout voltage levels are chosen to be comparable to those of reported EIT systems [8].

3.5.1 Simulations setup

Simulations performed are based on the setup shown in fig. 3.12, where two active electrodes are placed in opposite positions on the head, one injecting a current of 1 mA on the right side of the head and one draining the same current on the left side. Configurations of 32, 64, 128 and 256 passive electrodes with a radius varying from 2 to 5 mm equally distributed on the surface are considered to detect potential variations from the reference values.
Conductivity variations are introduced in regions (*active regions*) of variable size and position with respect to the injecting electrode; in particular the active regions are located along semicircular arcs centered on the injecting electrode. In this way it is possible to consider in the analysis brain region with different ratios of white-gray matter voxels and check the influence of WM anisotropy on the measures.
Simulations are performed at typical EIT frequencies in the 1 KHz to 10 MHz range.

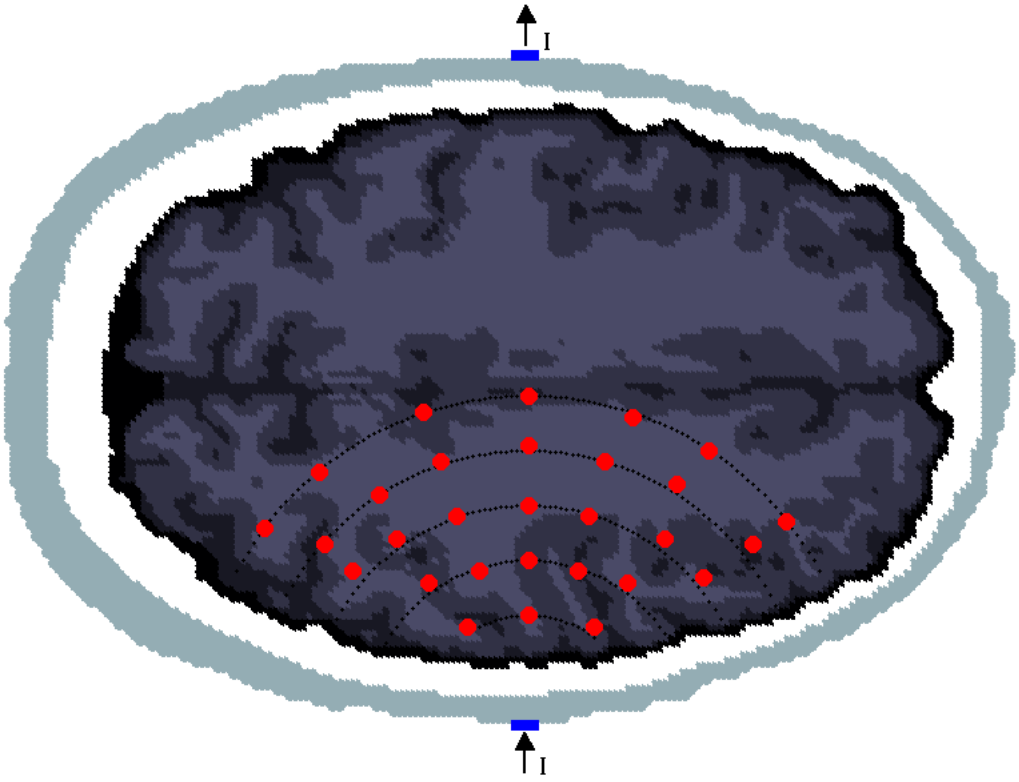

Figure 3.12: *Segmented head volume slice representing the scheme used in the simulations. From the outermost region, scalp, skull, CSF, gray and white matter are identified. A current I is injected between two active electrodes and an active region subject to conductivity change is placed at the positions indicated by the red points, one at a time. Points are distributed along circular arcs centered on the injecting electrode and covering brain regions with different ratios of white-gray matter voxels.*

3.5.2 Electrode sensitivity analysis and electrode characteristics influence

A set of simulations using the presented sensitivity approach are performed in order to characterize the sensitivity of the electrodes to different conductivity variations in different areas. In this first set of simulation white matter anisotropy is not considered, to focus analysis of results on electrical sensitivity of electrodes.

Firstly, sensitivity of the electrodes to active regions at variable distances

is studied.
Using 256 passive electrodes with a 2 mm radius and two active electrodes injecting a current of 1 mA at 1 KHz, a change of 10% of the conductivity is induced in cubic active regions of 2000 mm^3 located as shown in fig. 3.12. Simulation results are plotted in fig. 3.13.a in terms of electrode potential variations with respect to the reference configuration. In particular, data are relative to four passive electrodes chosen in the set, located at 20, 30, 40, 60 mm from the active region under examination, and are presented as a function of the distance between the active regions and the injecting electrode.
Voltage variations strongly depend both on the distance between the active regions and the active electrode, and on the distance between the regions

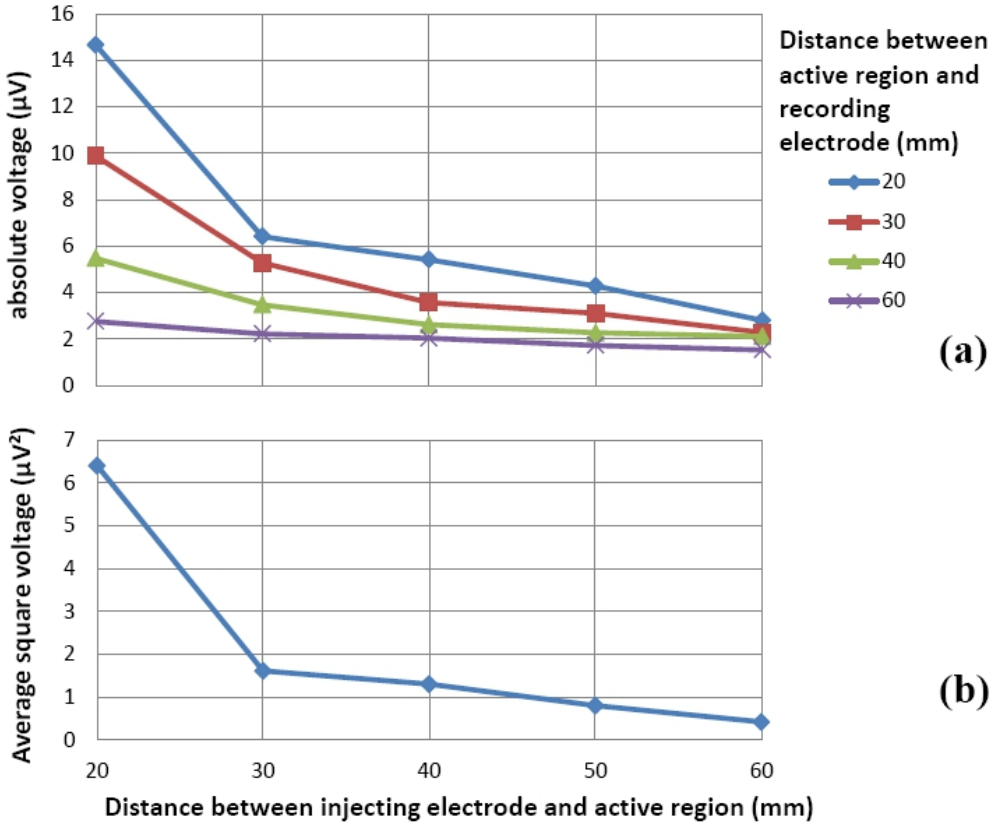

Figure 3.13: *Active region-electrode distances influence: a) Highest absolute values of potential detected by the passive electrodes when a region of 2000 mm^3 changes its conductivity by 10%. b) Average square voltage detected by a set of 256 electrodes when a region distant 20, 30, 40, 50, 60 mm from the injecting electrode changes its conductivity by 10%.*

and the passive one. Fig. 3.13b shows as the average square potentials are similarly influenced by the distance between the active region and active electrode. This analysis also shows how, neglecting white matter anisotropy, the relative positions between the active regions and the line joining the active electrodes do not substantially influence the potential variations detected.

The influence of the size of the active region on the recorded voltages is shown in fig. 3.14, where the highest absolute voltage variations detected are plotted as a function of active region to active electrode distance. Potential

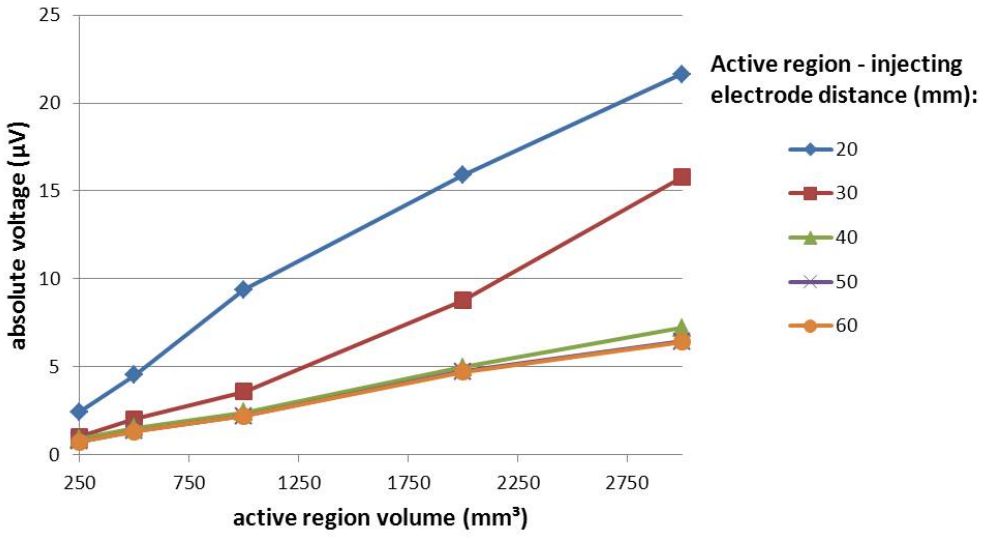

Figure 3.14: *Highest absolute voltage variations induced on the passive electrodes by active regions of different sizes located at a 20-60 mm distance from the injecting electrode.*

variations scale almost linearly with the size of the active region. Considering the noise levels of state of the art analog circuits [75], an EIT instrumentation can detect active regions smaller than 1 cm^3 (less than a few μV with 1 mA of injected current), which can be indicative of brain lesions. These values are obtained for injected currents of 1 mA and scale linearly with this amplitude.

The influence of the conductivity changes in the active region is shown in fig. 3.15 at frequencies between 1 KHz and 10 MHz. The highest absolute voltage variation induced by changes from 5% to 20% of the complex conductivity tensors of each voxel belonging to the active region scale linearly, independent of frequency. In general, a weak dependence on the frequency can be observed, with peaks visible at 1 KHz, 100 KHz and 10 MHz. To

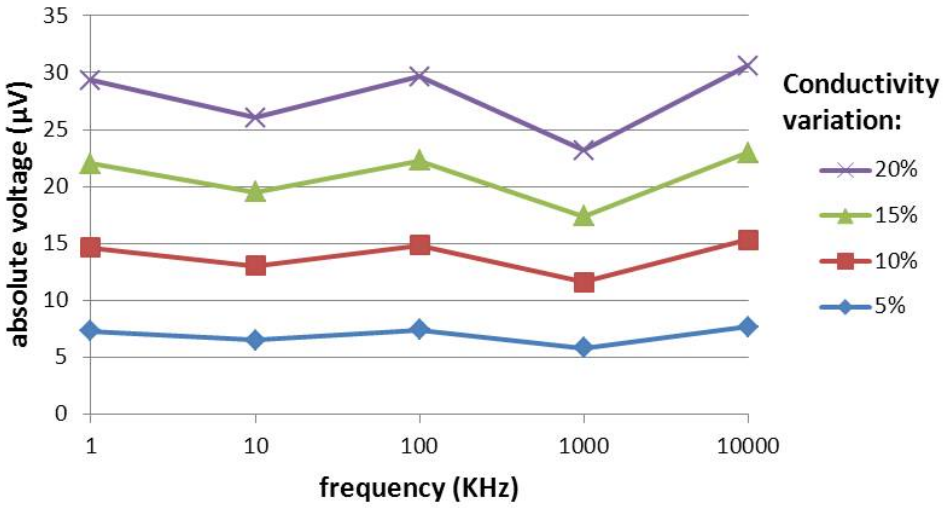

Figure 3.15: *Highest absolute voltage variations induced on the passive electrodes by an active region of 2000 mm^3 at 20 mm from the injecting electrode at different frequencies with changes of the complex conductivity tensors of the region from 5% to 20% of the reference value.*

justify this behavior, real and imaginary parts of the electrode voltage are plotted separately in fig. 3.16, with 10% variations in the imaginary and real part of the active region conductivity. The real potential induced by real and imaginary variations of the conductivity is practically constant with the frequency; in particular, the one induced by variations in the imaginary part is one order of magnitude smaller. The imaginary part of the potential induced by imaginary conductivity variations tends to increase in module at higher frequencies. Changes of the real conductivity result in particularly relevant variations of the imaginary potential around 100 KHz.

3.5.3 White matter anisotropy influence

The influence of the anisotropic conductivity of the white matter on the recorded potentials is demonstrated by performing a set of simulations under the conditions shown in fig. 3.12 with a set of 32 passive electrodes and an injected current frequency of 1 KHz. Active regions have a volume of 2000 mm^3 with a relative change of conductivity of 20%. The voltage variations induced activating one of these regions are evaluated considering white matter both anisotropic and isotropic.

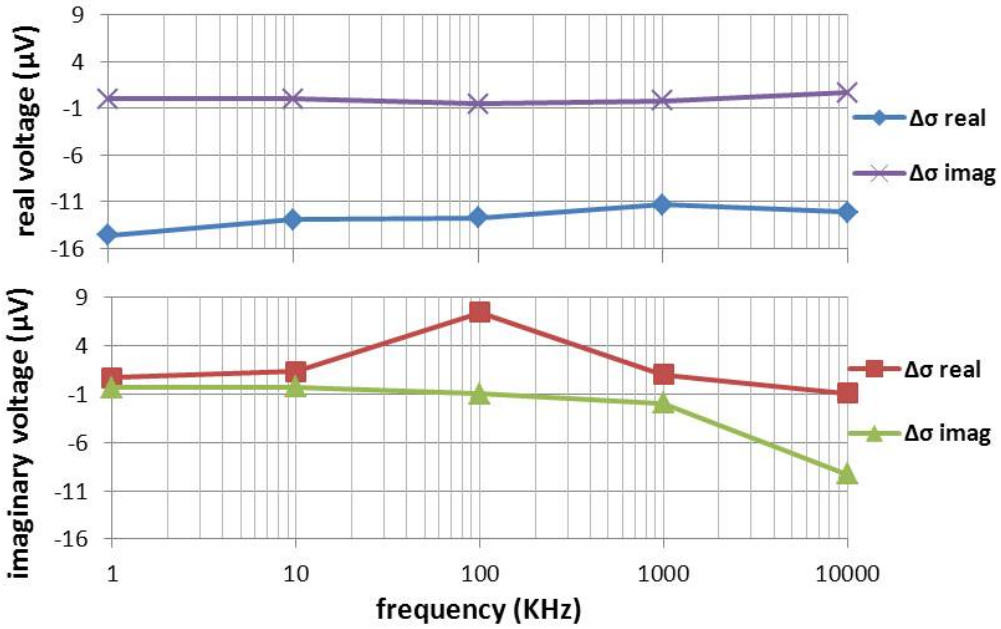

Figure 3.16: *Real and imaginary component of the potential induced by an active region at various frequencies. Shown in the first graph are real voltages due to changes in the real and imaginary parts of conductivity, while in the second graph, the relative imaginary components are shown.*

Highest voltage variations computed in the two configurations are shown in fig. 3.17, where the results are arranged in four graphs according to the distance between the active region and the injecting electrode. Results show that in this situation, white matter anisotropy causes differences in the voltage variations up to 300% with respect to the isotropic case. In fact, the two solutions are strictly similar when the active region is placed where the gray matter volume (isotropic) is dominant, such as in the first two rings and in the corners of the others, while the difference increases where white matter becomes dominant.

3.5.4 Perturbations due to electrode(s)

A set of simulations was performed to analyze the impact of the size and the contact impedance of the electrodes. Fig. 3.18 shows the average square voltage variations detected on the passive electrodes induced by an active region subject to a conductivity change of 20% at a 2 cm distance from the electrode injecting 1 mA current at a frequency of 1 KHz. Data are recorded by 30 passive electrodes. Contact impedance effects are relatively low in this

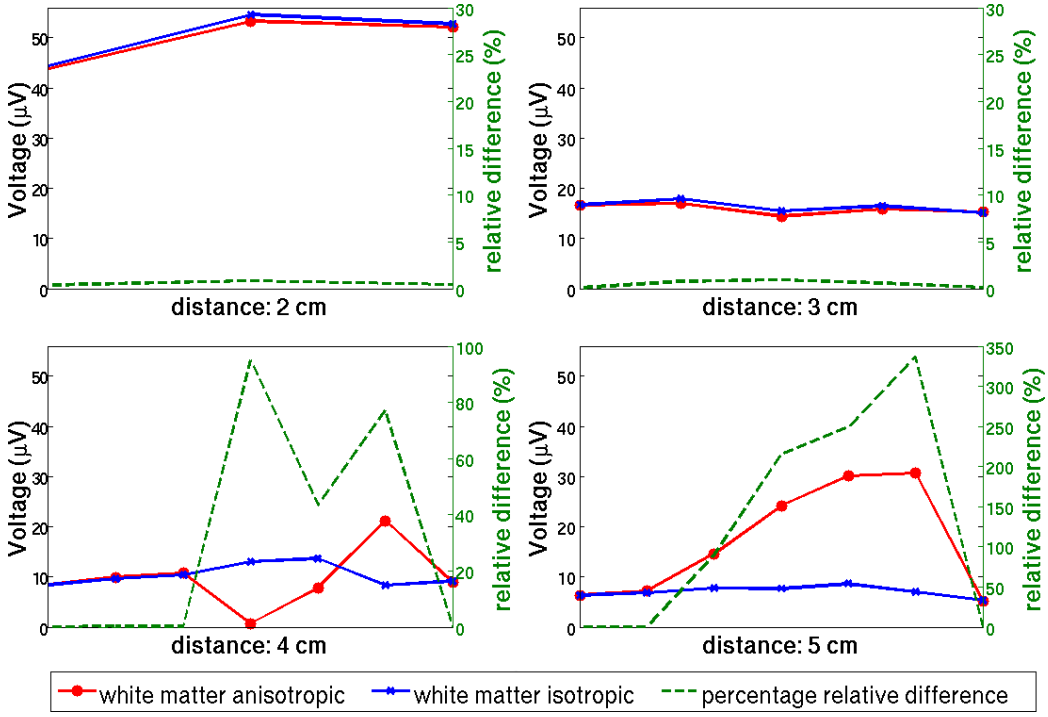

Figure 3.17: *Maximum electric potential variations induced on the electrodes by active regions 2, 3, 4 and 5 cm away from an injecting electrode. Data are organized according to the scheme of fig. 3.12; spanning the x-axis of each graph, values obtained by moving an active region from left to right along one of the arcs are presented.*

case, while the different electrode sizes can cause variations up to 10%. These perturbations increase with growing electrode number. Simulation shows that with 64 electrodes, a decrease in the measured peak voltage perturbation can be observed, which increases with electrode radius. This is due to the perturbation on the electric field caused by the electrode itself, since for a high density configuration of 256 electrodes of 5 mm radius, almost one fourth of the scalp surface is covered by electrode metal. In any case, the maximum decrease (256 electrodes, 5 mm radius) is less than 10%, an acceptable result for the design of the analog circuitry.

3.6 EIT inverse problem: linearized approach

EIT inverse solution is a ill-posed under-determined non-linear problem due two main reasons. First, due to electrical properties of the head tissues, a linear internal conductivity variation does not result on linear variations at

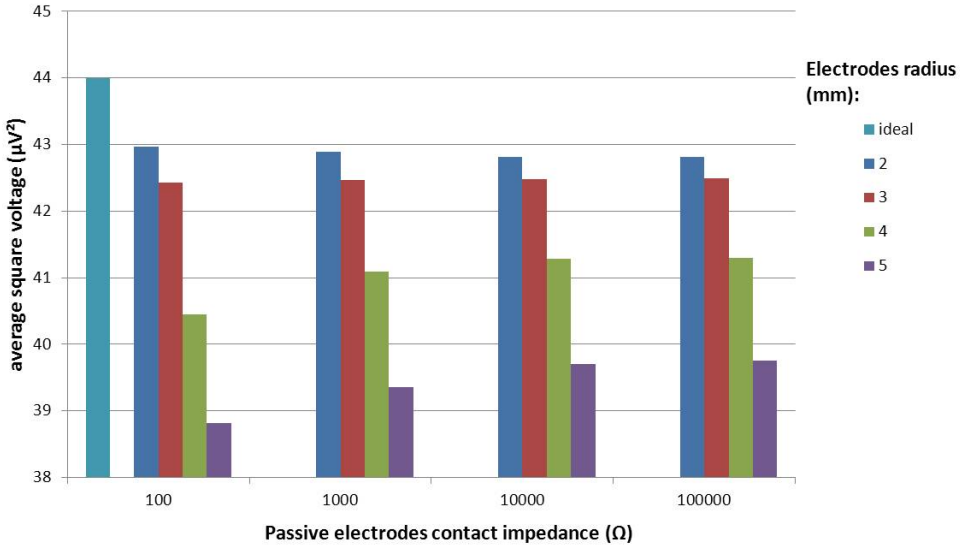

Figure 3.18: *Average square voltage detected on passive electrodes of different size. Contact impedance of the active electrodes is constant (1 KΩ), while for the passive electrodes it changes from 100 Ω to 100 KΩ. The first column is relative to the ideal situation with punctiform electrodes.*

the electrodes (Chapter 3.5). Second, the number of electrodes data is much smaller than voxels number.
One of the most used class of techniques to solve EIT inverse problem is based on the linearization of the problem. This is based on the assumption that for small variations of the conductivity distribution, changes on the electrodes voltage are linear [8]. Linearizing problem 3.22 holding fixed injected currents results in:

$$\Delta \boldsymbol{U} = \boldsymbol{J} \Delta \boldsymbol{\sigma}^* \tag{3.31}$$

where $\Delta \boldsymbol{U}$ is vector of the voltage variations on the electrodes, $\Delta \boldsymbol{\sigma}^*$ the conductivity (small) variations vector and $\boldsymbol{J}$ the Jacobian matrix of problem 3.22.
Inverse problem is so formulated in order to fit measured data at the electrodes ($\Delta \boldsymbol{U}_{meas}$) with the electrodes voltage predicted by eq. 3.31. This results in the minimization of a functional F defined as:

$$F(\Delta \boldsymbol{\sigma}^*) = \left\| \Delta \boldsymbol{U}_{meas} - \boldsymbol{J} \Delta \boldsymbol{\sigma}^* \right\|^2 \tag{3.32}$$

Minimization of F is an ill-posed problem with infinite solutions. In order to select a proper solution a regularization term is added to the functional:

$$F(\Delta \boldsymbol{\sigma}^*) = \left\| \Delta \boldsymbol{U}_{meas} - \boldsymbol{J} \Delta \boldsymbol{\sigma}^* \right\|^2 + \alpha \left\| \boldsymbol{L} \Delta \boldsymbol{\sigma}^* \right\|^2 \tag{3.33}$$

where $\boldsymbol{L}$ is a regularization matrix and α a control parameter. Different regularization matrix are reported in literature; $\boldsymbol{L}$ can be a 3D laplacian filter to reduce smoothness in the solution [76], or an identity matrix obtaining a standard zero-order Tikhonov-Philips regularization (as in EEG inverse problem, Chapter 2.6), or a diagonal matrix where values are scaled according to the sensitivity of each voxels (so $\boldsymbol{L} = diag(\boldsymbol{J}^T\boldsymbol{J})$) in order to avoid favoring most external voxels [77].

3.6.1 EIT inverse problem: Jacobian computation

Jacobian matrix $\boldsymbol{J}$ is a rectangular $(N_E - 1)\text{x}N_V$ matrix with N_E number of the electrodes and N_V number of voxels (rows number is smaller than N_E because an electrode acts as reference for the others). Each $\boldsymbol{J}_{ij}$ is the potential variation induced on the i-th electrode by a conductivity variation of the j-th voxel.
In this formulation variations in the orientation of conductivity tensors are not considered (eq. 3.7), so Jacobian can be formulated considering scalar conductivity values:

$$\boldsymbol{J}_{ij} = \frac{\Delta U_i}{\Delta \sigma_j^*} \tag{3.34}$$

Direct computation of $\boldsymbol{J}$ requires a forward problem computation for each voxel, which it is impossible for a realistic head volume. The number of necessary computations can be reduced to $N_E - 1$ applying the principle of reciprocity to the EIT problem [78]. This allows to compute a jacobian row at once. Lets assume an arbitrary conductive volume Ω with complex conductivity distribution σ^* and four electrodes A, B, C and D as shown in fig. 3.19. In the first situation a current I is applied to electrodes A and B (fig. 3.19.a), resulting in a potential distribution φ and in a voltage U_{CD} between electrodes C and D. In fig. 3.19.b a reciprocal situation is shown, where the same current I is applied to C and D, generating a potential distribution ψ and a voltage U_{AB} between A and B. Multiplying generated current density in first situation with ψ and integrating at the volume surface yields:

$$U_{AB}I = -\iint_{\partial\Omega} \psi\sigma^*\nabla\varphi \,\mathrm{d}S \tag{3.35}$$

where current density is expressed by Ohm's law and no current flowing outside the volume is imposed, except for the electrodes. Applying Gauss's

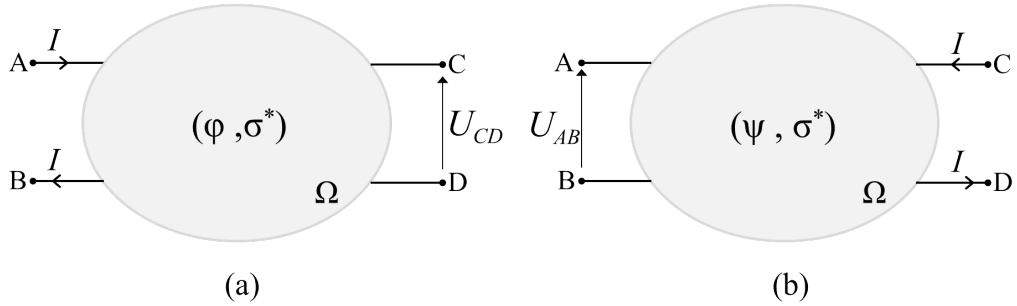

Figure 3.19: *EIT reciprocal configuration in a conductive volume Ω. A current applied to A and B leads to a potential distribution φ, and a voltage U_{CD} can be measured between C and D. (b) With the same current applied to C and D, a potential distribution ψ results, leading to a voltage U_{AB} between A and B.*

theorem to eq. 3.35:

$$\iint_{\partial\Omega} \psi\sigma^*\nabla\varphi \,\mathrm{d}S = \iiint_{\Omega} \nabla(\psi\sigma^*\nabla\varphi) \,\mathrm{d}S = \iiint_{\Omega} \sigma^*\nabla\psi\nabla\varphi \,\mathrm{d}V + \iiint_{\Omega} \psi \underbrace{\nabla\sigma^*\nabla\varphi}_{=0} \,\mathrm{d}V \tag{3.36}$$

Last integral of eq. 3.36 is zero according to the Poisson problem 3.1. Repeating the same procedure to case (b) yields to the following equations:

$$\begin{aligned} U_{AB} &= -\frac{1}{I} \iiint_{\Omega} \sigma^*\nabla\psi\nabla\varphi \,\mathrm{d}V \\ U_{CD} &= -\frac{1}{I} \iiint_{\Omega} \sigma^*\nabla\varphi\nabla\psi \,\mathrm{d}V \end{aligned} \tag{3.37}$$

Eq. 3.37 states that in a reciprocal configuration potential difference measured between a couple of electrodes CD when a current pattern is injected on an other couple of electrodes AB, is the same occurring between AB when the same current pattern is applied on electrodes CD. Considering the discretization of the domain in N_V voxels, first equation can be written as:

$$U_{AB} = -\frac{1}{I} \sum_{i=1}^{N_V} \iiint_{\Omega_i} \sigma_i^*\nabla\psi^i\nabla\varphi^i \,\mathrm{d}V \tag{3.38}$$

where Ω_i is the volume of i-th voxel, σ_i^* its conductivity, ψ^i and φ^i potential at its nodes in the two reciprocal configuration. From eq. 3.38 computing of

jacobian row referred to electrode pair CD when a current I is injected on AB is immediate:

$$\frac{\partial U_{CD}}{\partial \sigma_i^*} = -\frac{1}{I} \iiint_{\Omega_i} \nabla\psi^i \nabla\varphi^i \, \mathrm{d}V \tag{3.39}$$

So, using a reciprocal approach, it is possible to compute Jacobian matrix solving EIT forward problem with different current patterns, one for each rows. Firstly it is necessary to solve forward problem with the injection pattern really used in the measures like in fig. 3.19.a to obtain φ distribution. Second, for each passive electrodes pairs it is necessary to determine the relative ψ distribution using them as active electrodes, like in fig. 3.19.b. Potential distributions in the two situations are then elaborated according to eq. 3.39. Numerical computation of this integral on each voxels can be efficiently performed considering that potential is assumed to be linear, according to the FVM implementation used (tri-linear in the 3D space). Referring to fig. 3.20, potential φ on the generic voxel can be expressed by the tri-linear form:

$$\begin{aligned}\varphi =& a(x-x_0) + b(y-y_0) + c(z-z_0) + \\ & d(x-x_0)(y-y_0) + e(x-x_0)(z-z_0) + f(y-y_0)(z-z_0) + \\ & g(x-x_0)(y-y_0)(z-z_0) + l\end{aligned} \tag{3.40}$$

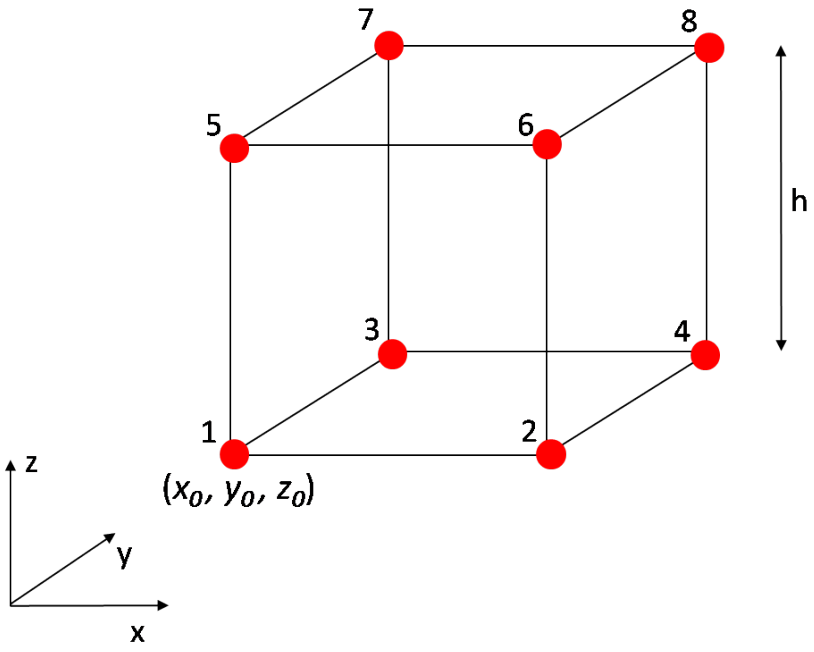

Figure 3.20: *Labels of the nodes in an EIT voxels.*

where constant coefficients are given by value of φ at each node. Considering for simplicity $(x_0, y_0, z_0) = (0, 0, 0)$ and pass h equal to 1, potential gradient in the generic voxel is:

$$\begin{cases} \nabla\varphi|_x &= a + dy + ez + gzy \\ \nabla\varphi|_y &= b + dx + fz + gxz \\ \nabla\varphi|_z &= c + ex + fy + gxy \end{cases} \tag{3.41}$$

Given this expression, products and exact integrations of the potential gradients in eq. 3.39 is trivial. Coefficients for each voxel can be computed from potentials at the nodes as following:

$$\begin{pmatrix} a \\ b \\ c \\ d \\ e \\ f \\ g \\ l \end{pmatrix} = \begin{pmatrix} -1 & 1 & 0 & 0 & 0 & 0 & 0 & 0 \\ -1 & 0 & 1 & 0 & 0 & 0 & 0 & 0 \\ -1 & 0 & 0 & 0 & 1 & 0 & 0 & 0 \\ 1 & -1 & -1 & 1 & 0 & 0 & 0 & 0 \\ 1 & -1 & 0 & 0 & -1 & 1 & 0 & 0 \\ 1 & 0 & -1 & 0 & -1 & 0 & 1 & 0 \\ -1 & 1 & 1 & -1 & 1 & -1 & -1 & 1 \\ 1 & 0 & 0 & 0 & 0 & 0 & 0 & 0 \end{pmatrix} \cdot \begin{pmatrix} \varphi_1 \\ \varphi_2 \\ \varphi_3 \\ \varphi_4 \\ \varphi_5 \\ \varphi_6 \\ \varphi_7 \\ \varphi_8 \end{pmatrix} \tag{3.42}$$

3.7 Noise Evaluation in EIT and EEG

Both in EEG and EIT case, potential variations on the scalp are very limited in magnitude, generally between 1 and 100 μV. As previously introduced, this is mainly due to electrical properties of the skull, which is more resistive than others head tissues, so that limiting propagation of the electric field. Given the limited amplitude of potential variations, the analogic design of electrodes needs to take into account perturbations introduced by noise. In particular it necessary to maintain a level of noise lower than 1 μV_{RMS} in the band of acquisition. In EEG for example, being information located at low frequencies ($< 30Hz$), the IFCN standard requires additional noise in the recording to be less than 1.5 mV peak-to-peak and 0.5 mV root-mean-square at any frequency from 0.5-100 Hz including 50-60 Hz [79]. However, while noise sources and effects due to instrumentation measurements are known, in our knowledge an analysis to evaluate influence of head cells noise on the electrodes is not present in literature.
In the particular case of neurons, noise is largely studied using patch of neuronal membranes, leading to a classification of its sources which could be summarized as [80]:

- Johnson noise, due to thermal agitation of the charge carriers,

- channel noise, due to activity of the potassium and sodium ionic channels in the cell membrane (Chapter 1.3.2),
- synaptic noise, associated to the synapses of the neurons.

Effects of local source of noise inside the head must be reported at the electrodes to evaluate their real influence on the measurements. For this purpose we have used a procedure based on the application of the reciprocity principle on our EIT realistic head model. This procedure allows to estimate transfer functions between each voxels and the scalp electrodes. It is important to highlight that this analysis is not limited to EIT environment, but is valid also for EEG and more in general to evaluate electrical perturbations induced by head internal noise sources on any points of the head volume and of scalp surface.

3.7.1 Noise sources in neurons

Noise sources in a head voxel can be modeled as injected noise currents. For neurons, [15] asserts that noise generated by a neural membrane patch of 1000 μm^2 can be described by a current power spectral densities $S_I(f)$ as shown in Table 3.3. Here noise is classified according to its source, and channel noise is split in the contributes given by potassium ionic channels and sodium ionic channels. So considering noise induced by cells in a voxel

Frequency (Hz) / Noise Source	0	10	100	1 K	10 K
Thermal	-29,8	-29,8	-29,8	-29,8	-29,8
Na	-29	-29	-29	-29	-30
K	-26,7	-26,7	-28	-30	-32
Synaptic	-26,2	-26,2	-26,5	-32	-34

Table 3.3: *Noise current power spectral densities $S_i(f)$ generated by a neuronal membrane patch of 1000 μm^2 at frequencies from 1 to 10 KHz. Noise is classified according to its sources. Data are in logarithmic scale.*

as a current injection on its relative nodes, the resulting noise voltage power spectral density $S_V(f)$ on the electrodes can be obtained scaling $S_I(f)$ of each voxel for the power of its relative function transfer and then summing all contributions:

$$S_{V,j}(f) = \sum_k |H_{jk}(f)|^2 S_{I,k}(f) \tag{3.43}$$

where H_{jk} is the transfer function between k$-th$ noise source and the j$-th$ electrode.

3.7.2 Transfer functions computation

Transfer function H_{jk} can be computed exploiting the reciprocity principle in a similar way as for jacobian evaluation (Chapter 3.6.1). Lets assume an arbitrary conductive volume Ω with a complex conductivity distribution σ^*, two electrodes A and B, and two internal points C and D, as shown in fig. 3.21.

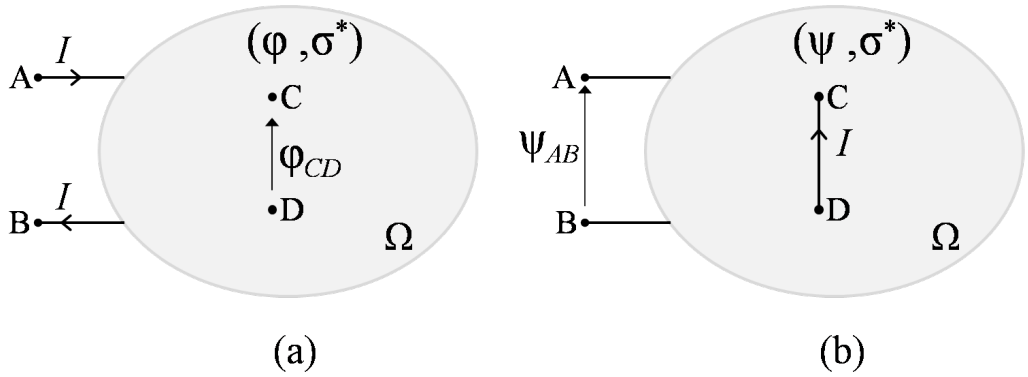

Figure 3.21: *(a) Conducting volume Ω with complex conductivity σ^*. A current I applied to ports A and B leads to a potential distribution φ, with a φ_{CD} between points C and D. (b) Same current I is applied to points C and D, resulting in a potential distribution ψ and a voltage ψ_{AB} which can be measured between points A and B.*

A current I is applied in the first situation to electrodes A and B (fig. 3.21.a), resulting in a potential distribution φ and in particular in a potential difference φ_{CD} between internal points C and D. In fig. 3.21.b instead a reciprocal situation is shown, where the same current I is applied to C and D, generating a potential distribution ψ and a difference of potential ψ_{AB} between A and B. Potential difference φ_{CD} and ψ_{AB} can be correlated. In Chapter 3.6.1 this is demonstrated when also points C and D are external to volume. A similar results can also be obtained when C and D are inside Ω. Multiplying generated current density in first situation with ψ and integrating at the volume surface yields:

$$\psi_{AB} = -\frac{1}{I} \iiint_{\Omega} \sigma^* \nabla\psi \nabla\varphi \, \mathrm{d}V$$

In case (b) no current flows outside the volume because current I is injected in internal points C and D. In this condition Poisson problem has to be

reformulated:

$$\nabla\sigma^*(\boldsymbol{r})\nabla\psi(\boldsymbol{r}) = I^{'}(\delta(\boldsymbol{r}-\boldsymbol{r}_C)-\delta(\boldsymbol{r}-\boldsymbol{r}_D)) \tag{3.44}$$

where $\boldsymbol{r}$ is the generic vector point, $\boldsymbol{r}_C$ and $\boldsymbol{r}_D$ vector pointing to C and D, δ is the Dirac function and $I^{'}$ a volumetric impressed current density. Multiplying generated current density $\boldsymbol{J}$ in the second situation with φ and integrating at the volume surface yields:

$$\iint_{\partial\Omega} \boldsymbol{J}\,\mathrm{d}\boldsymbol{S} = -\iint_{\partial\Omega} \varphi\sigma^*\nabla\psi\,\mathrm{d}S = 0 \tag{3.45}$$

where current density is expressed by Ohm's law and no current flows outside the volume because electric sources are inside the domain. Applying Gauss's theorem to eq. 3.45:

$$\begin{aligned}\iint_{\partial\Omega} \varphi\sigma^*\nabla\psi\,\mathrm{d}\boldsymbol{S} = \iiint_{\Omega} \nabla(\varphi\sigma^*\nabla\psi)\,\mathrm{d}S = \\ \iiint_{\Omega} \sigma^*\nabla\varphi\nabla\psi\,\mathrm{d}V + \iiint_{\Omega} \varphi \underbrace{\nabla\sigma^*\nabla\psi}_{=I^{'}(\delta(\boldsymbol{r}-\boldsymbol{r}_C)-\delta(\boldsymbol{r}-\boldsymbol{r}_D))} \mathrm{d}V\end{aligned} \tag{3.46}$$

Last volume integral is different from zero only in $\boldsymbol{r}_C$ and $\boldsymbol{r}_D$ according to Poisson problem 3.44, and integration of the source volumetric current density $I^{'}$ is the impressed current I. Consequently:

$$\varphi_{CD} = -\frac{1}{I}\iiint_{\Omega} \sigma^*\nabla\varphi\nabla\psi\,\mathrm{d}V \tag{3.47}$$

Then combining eq. 3.47 and eq. 3.44 finally results in the reciprocity principle formulation for these two configurations:

$$\varphi_{CD} = \psi_{AB} = -\frac{1}{I}\iiint_{\Omega} \sigma^*\nabla\varphi\nabla\psi\,\mathrm{d}V \tag{3.48}$$

So, using a reciprocal approach, it is possible to compute the transfer function between any voxel and the generic electrode couple AB, performing a single forward problem simulation. Eq. 3.48 states in fact that the resulting potential differences between nodes of the volume when a current pattern is injected on electrodes AB, is equal to the potential difference at AB when the same current is injected directly on the interested nodes. Consequently, imposing $I = 1A$, these values represents the transfer function between current impressed at any couple of nodes and the resulting voltage differences at the electrodes.

3.7.3 Simulation Results

First of all in this noise analysis we have considered the head model as a pure impedances network, associating at each impedance a current injection given by its thermal noise according to the well-known Johnson formula:

$$S_{I,k}(f) = 4K_B T Re\{Z_k\} \tag{3.49}$$

where Z_k is the k-th impedance of the head model, K_B the Boltzmann constant and T the temperature. Results are shown in fig. 3.22, where are considered the contributes of the different tissues and the power noise given by the electrodes with contact impedances of 100Ω and $1K\Omega$. It is evident

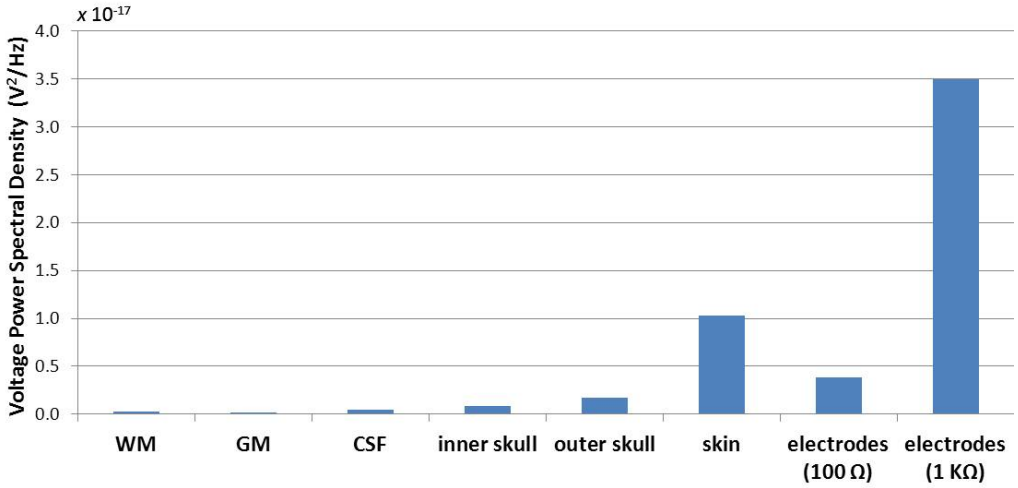

Figure 3.22: *Thermal noise power spectral density on a couple of electrodes due to various head tissues at a temperature of 310°K. Last two columns indicates the contributes given by the thermal noise of the electrodes considering a contact impedance of 100Ω and 1KΩ.*

that influence of electrodes noise is considerably higher than noise due to the tissues. This because transfer functions associated to internal sources are strongly dependent by the distance to the considered electrodes, as shown in the sagittal slice in fig. 3.23, where each pixel represents a voxel, and its color the power of the associated transfer function referred to a couple of injecting electrodes. However, as shown in Table 3.3 in the case of neurons, thermal noise is not the unique source of noise given by cellular activity. For example synaptic noise is four order of magnitude bigger than Johnson one. In order to provide an estimate of the neurons noise sources influence, we

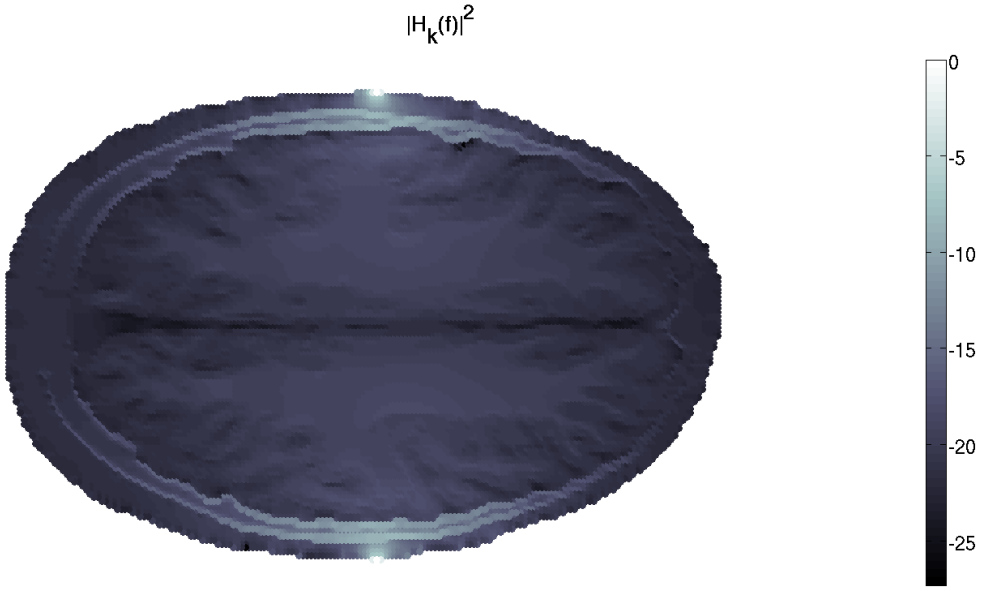

Figure 3.23: *Power of transfer functions between couples of points in a sagittal slice of the head model and a couple of electrodes located at the brightest points. Data are in logarithmic scale.*

have modeled a brain gray matter voxel considering a population of neurons according to parameters given in [81], where an occupancy of 46% of neurons in gray matter volume is considered, and dendrites are modeled as cylinders. Considering cylinders of 5 μm of radius and length 5 μm in a voxel of $1mm^3$, this results in an equivalent area given by all the membranes of about 108 μm^2. Data in Table 3.3, which are relative to an membrane area of 1000 μm^2, are then scaled to the total area occupation. Noise evaluation is so performed, obviously considering only gray matter voxels; results obtained are shown in fig. 3.24 compared to thermal noise due to contact impedances of the electrodes. Data are relative to noise induced by synapses and channels activity. This last is split in the contributes given by potassium (K) and sodium (Na) channels. In this case, synaptic activity, although attenuated by distances voxels-electrodes, comports a resulting voltage noise on the electrodes comparable with thermal noise due to contact impedances of $1K\Omega$.

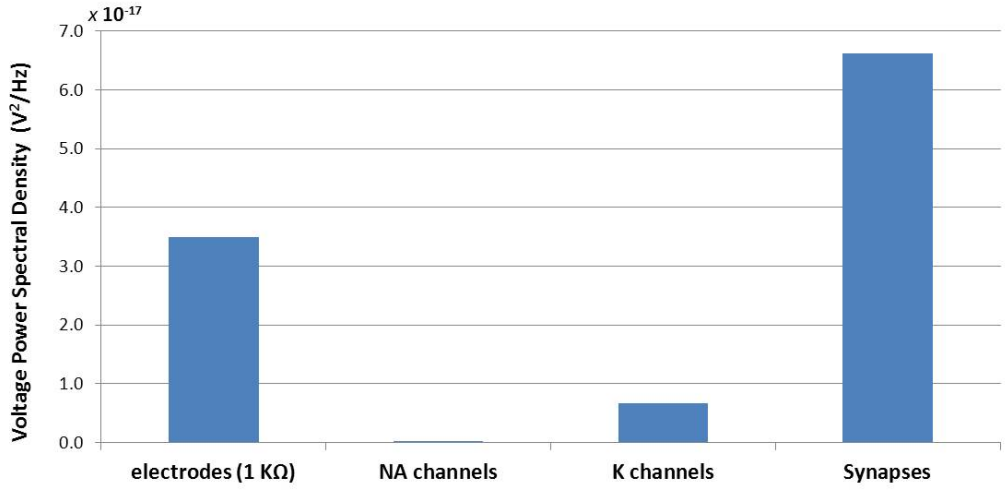

Figure 3.24: *Voltage power spectral densities on the electrodes given by neuronal noise sources in the brain cortex.*

Chapter 4

Parallel Computation on Graphical Processing Units (GPUs)

Both the EIT and the EEG computational work-flows implemented in this work are designed in order to be accelerated on highly parallel multi-core architectures. This choice results in a parallel approach and the organization of the code in order to be efficiently executed on the target hardware. The computational demand of EIT and EEG algorithms for brain imaging is high; however, the usage of multi-core hardware allows to execute data processing in reasonable times or under strict temporal constraints without introducing simplifications in the models or reducing the available resolution.
In this chapter the hardware used is presented, focusing on the Graphical Processing Unit device (GPU), an highly parallel computing device programmable by the user. GPUs is a computing device, which, coupled with standard desktop workstation (*host system*), is able to provide performances as super-computing architecture, maintaining lower costs. Then GPU implementation of some EEG and EIT critic kernels is described.

4.1 The Graphical Processing Unit

As well known, originally GPUs were born as devices for graphical applications. Internal structures reflected steps of the so-called *rendering pipeline*, where each hardware block (*shader*) was specialized to efficiently execute a precise function of the 3D graphic elaboration process. The possibilities offered by a so vast market, coupled with the continuous growing demand of computational power (especially for videogames), have caused a rapid in-

crease in the GPU performances and computing capabilities. In 2006, the first GPUs with a unified shader model are presented; these GPUs were based on equal computing blocks (*unified shaders*), without any specializations and differentiation between each other. The resulting hardware was thus based on a parallel set of programmable scalar processors able to provide a high-throughput in data elaboration. Memory hierarchy and control logic was sacrificed to obtain as much area disposable for processors as possible (fig. 4.1), so making the GPUs particularly efficient for highly parallel computationally intensive tasks, but penalized for control or memory intensive tasks.

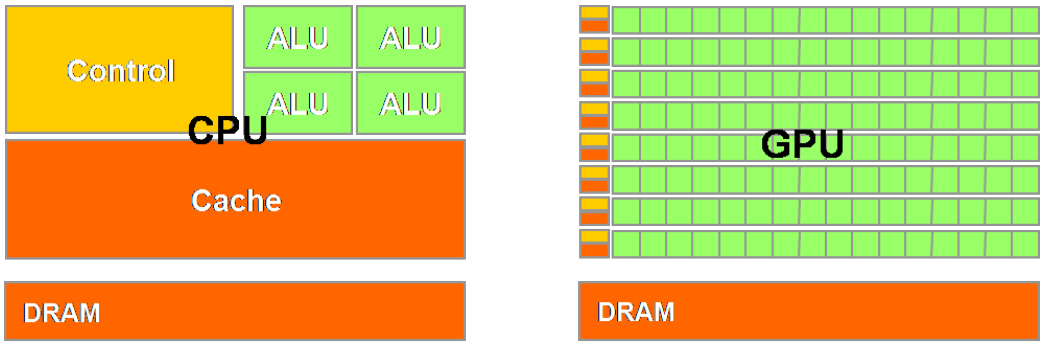

Figure 4.1: *Qualitative area occupation in CPU vs GPU.*[1]

The possibility to obtain high-throughput in data elaboration, without the higher costs of supercomputer, make GPUs today largely used in scientific computation in many different fields. The relevance of this new market is proven by the introduction of the last GPU generations of functionalities typical of scientific computing as:

- faster read-back from GPU memory,
- double precision support,
- fully IEEE-compliant floating point arithmetic,
- ECC error correction,
- hardware-controlled caching.

At the moment the leading company of the market is the NVIDIA®, which provides a user-friendly programming environment based on common high level programming language (C, C++) known as CUDA® (Compute Unified

[1]Source: NVIDIA®

Device Architecture) [82]. The last generation of NVIDIA GPU, the Fermi series (GTX480™), is able to provide more than one TFLOP/s (Tera floating point operations per second), which is 5 times higher than a serial processor INTEL® solution (fig. 4.2). It is interesting to note that the NVIDIA Tesla series does not even have a graphical output, highlighting so as GPUs usage in scientific computing is becoming an important market for the producers.

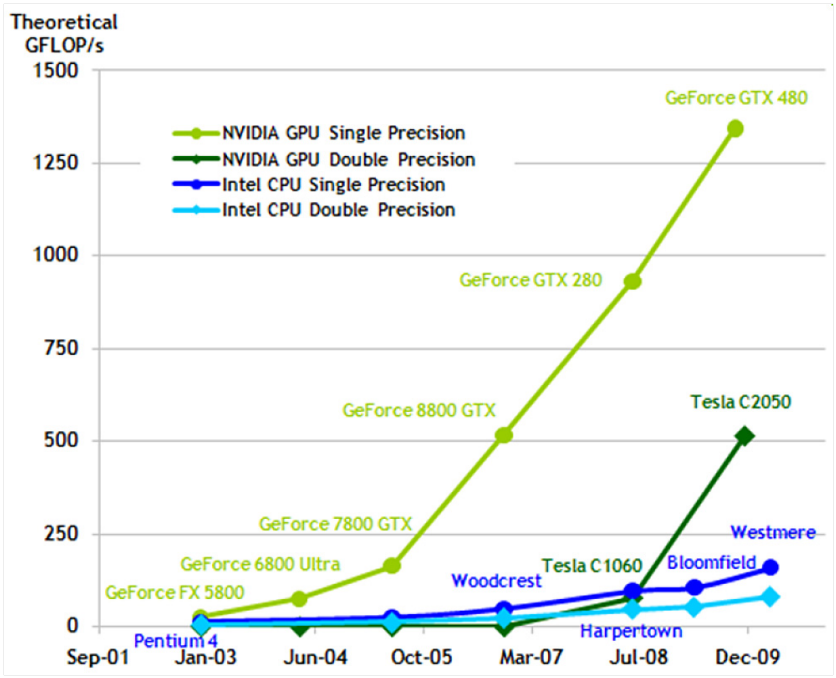

Figure 4.2: *Evolution in the last years of computable capacity of NVIDIA GPU and INTEL processors.*[2]

4.1.1 Architectural overview

A modern NVIDIA GPU board provides a chip composed by a set of parallel processors organized in blocks, the so-called Streaming Multiprocessors (SMs), which are organized in higher level structures (Texture Processing Clusters, TPCs). The interfacing between the chip and the PC is performed by a high-speed PCI express interface, which is connected to the system's north bridge. The GPU board is also equipped with an off-chip DRAM (*device memory*) with a capacity up to 1,5 GBytes. Because the data exchange with the DRAM can represent a bottleneck during data elaboration, the interface chip-DRAM is highly parallel, with 256-512 lanes towards the banks

[2]Source: NVIDIA®

memory (exact number depends on the GPU model).The general GPU architecture of the NVIDIA Series 8, 9 and 200 is displayed in fig. 4.3; a part TPCs and DRAM device, there are some blocks of dedicated logic to schedule instruction in case the GPU is used for graphical application, while a work distribution scheduler provides for the scheduling and distribution of instructions in the case of non-graphical applications. The number and ar-

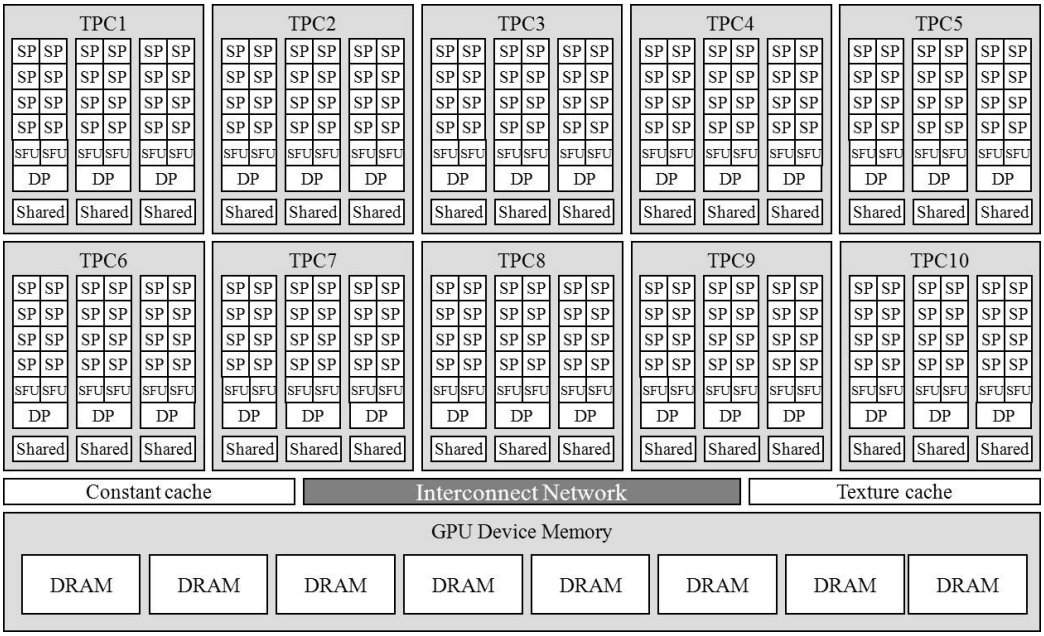

Figure 4.3: *NVIDIA GPU general architecture.*

chitecture of the TPCs depend on the individual GPU model: in NVIDIA GeForce® series 8 and 9, each TPC integrates two stream multiprocessors, each of which contains eight 32-bit floating point stream processors (SP) and two Special Function Units (SFU). On each SM are present 16kB of fast shared memory, a small constant cache and an instruction cache. SPs are optimized for single precision floating point arithmetic; integer and logic operations are possible but may take more clock cycles. Additional control logic includes a Texture Unit (TU) and a *Multi-Thread Instruction Fetch & Issue logic* (MTIFI). In the series 200, there are three SMs per TPC, and each one is additionally equipped with a double precision unit (DP). Each TPC has a shared Geometry Control (GC) and Stream Multiprocessor Control (SMC). Both TPC variants are shown in fig. 4.4. This architecture has been used in NVIDIA GPU GeForce series until the last generation. While the series 8, 9 and 200, in fact, maintain logic aided to the scheduling of graphical application, the new GeForce® 400 series (also known as *Fermi* serie) is more

oriented towards scientific computing. This is proven by a different hardware organization, where TPC clustering is abandoned and the GPU can be seen as a uniform array of SMs, as shown in fig. 4.5. Each SM in particular is

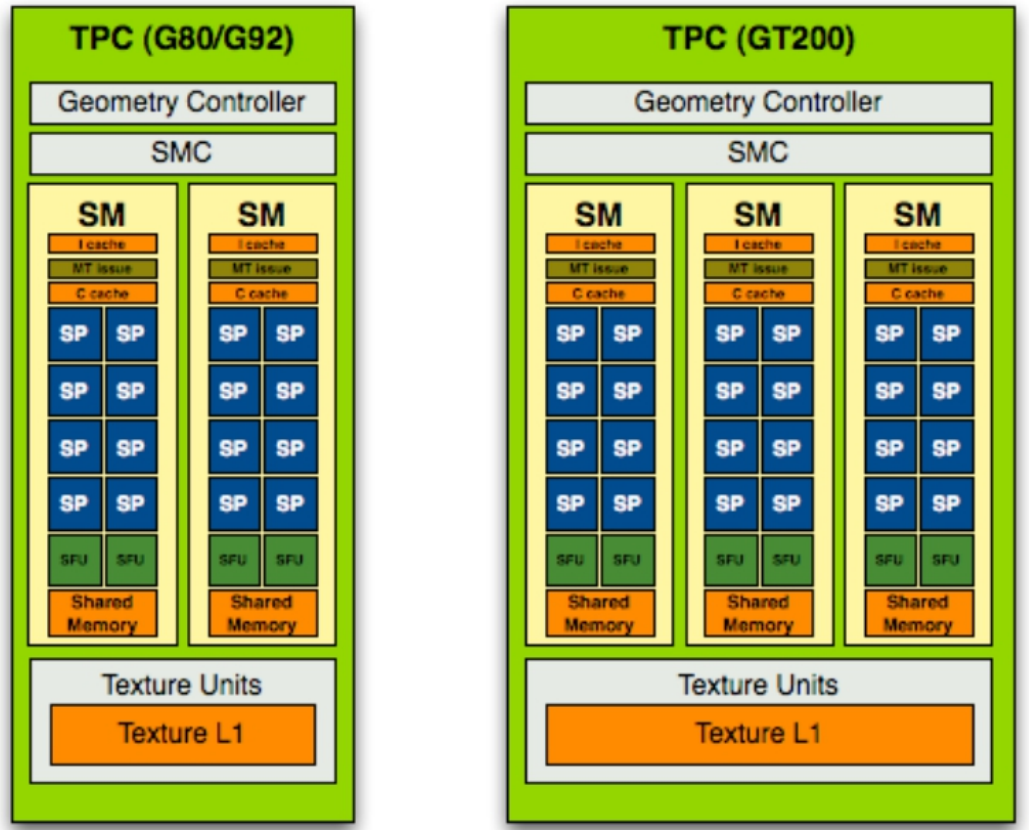

Figure 4.4: *TPC variants of the NVIDIA GeForce series 8 and 9 (left) and the NVIDIA GeForce series 200 (right).*[3]

now bigger, containing 32 SPs instead of 8 as in previous series, and 4 Special Function Units instead of 2. There is not a double precision logic block in SMs, but the same single-precision processors work in pairs to perform double precision computation; with this choice parallelism in double precision of each SM rises to 16 instead of 1 of the previous versions. Moreover each SP is now fully IEEE-compliant in floating point arithmetic computation and can issue one integer operation per cycle. The shared memory in each SM is much larger with 64kB, and has hardware controlled caching. These improvements are clearly oriented to make the Fermi series more suitable for scientific computing instead of graphical usage; for example double precision

[3]Source: `www.anandtech.com`

elaboration or hardware controlled cache are practically useless for graphic rendering.

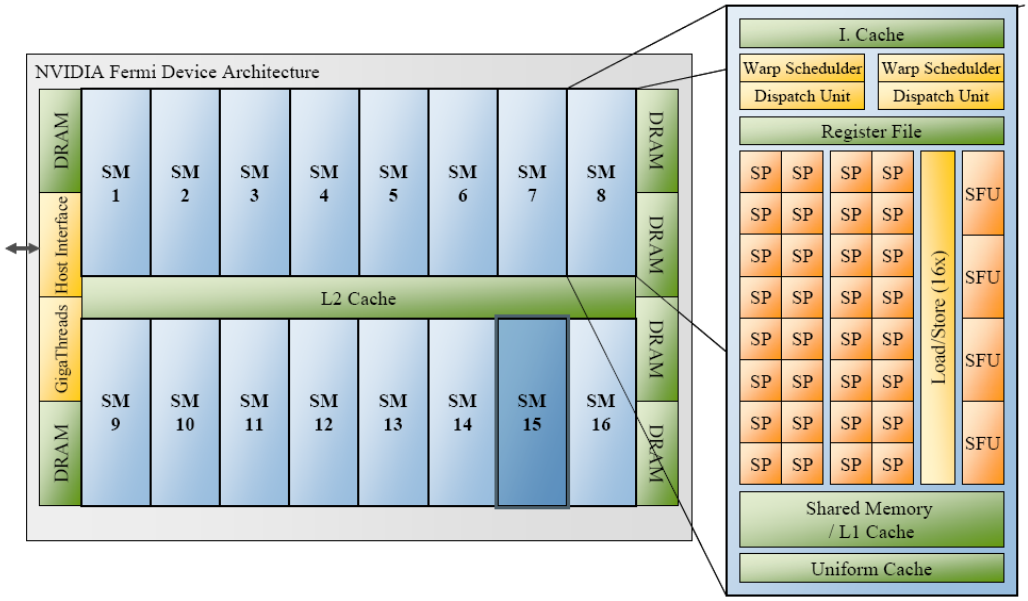

Figure 4.5: *Architecture of the NVIDIA series 400 (Fermi) GPU.*[4]

4.1.2 Compute Unified Device Architecture (CUDA)

CUDA® is a programming language developed by NVIDIA to program GPUs for non graphical applications. This is a C-based language, extended with a set of instructions aided to handle and manage GPU operations.
GPU is used in a normal desktop PC as a sort of passive user-programmable co-processor: it is not able in fact to replace CPU functionalities given its high level of specialization for parallel computing. Consequently it is used to accelerate critical kernels that are particularly onerous for CPU, exploiting its intrinsic parallelism and computing capabilities, while the control of all application is performed by the CPU. A common CUDA code is so composed by two parts: the first is the code running on the general purpose processor (*host code*), the second the effective GPU code (*device code*). The typical work flow during elaborations is the following:

1. CPU uploads input data to GPU memory.

[4]Source: [83]

2. The parallel GPU kernel code is transferred and launched onto the device. The code is executed asynchronously; to verify its completion the status needs to be polled by the CPU.

3. After completion, the CPU downloads the processed data sets to host memory for output or further usage.

GPU programming model

The GPU code is described by the user in a thread way; it can be seen as an array (*grid*) of identical threads, which are executed by each processor of the GPU on a different set of data. So the GPU code is given by instructions of a single thread, described in a parametric way in the function of the generic processor. It is important that this code is highly regular, in order to obtain as much as possible a homogeneous distribution of the instructions on all the GPU processor. As previously explained, in fact, on each Streaming Multiprocessor there is a single instruction manager, consequently all scalar processors in each SM can execute the same instruction (obviously on different data) each time, or at least stall. The occurrence of a divergence in the execution on a SM (e.g. given by a conditional statement whose result is different for some of the scalar processor) causes a serialization of the execution with consequent loss of performances.
The GPU code is organized in two levels. At the grid level, the threads are organized into blocks; each block is then assigned to each SM (fig. 4.6). This scheduling of the work is handled following a Single Instruction Multiple Threads paradigm (SIMT); this means that some degrees of divergence can be tolerated at this level, because the entire execution of a thread block is assigned to only one SM (which is equipped with an instruction manager). Blocks are independently executed as single sub-problems on each SM and no interaction or synchronization is possible between them. Differently, at the SM level, the threads in the assigned block are effectively executed on the SP. Here it is necessary that the execution is regular, strictly following a Single Instruction Multiple Data paradigm (SIMD); this effectively means that at each time all SP must execute the same instruction on different data (fig. 4.7); every divergence in the operations results in a code serialization. The threads inside a block, on the other hand, can easily communicate via the shared on-chip memory of the stream multiprocessor and can synchronize using a low-overhead barrier.
The data transfer connections and the limited structure of the memory hierarchy can introduce high latencies in GPU elaboration resulting in performance loss. This is solved by an ad hoc work load distribution strategy. On a

stream multiprocessor, the threads are divided into groups of 32 SIMD identical instructions (*warps*). This choice allows to cover latencies of instruction fetching and coding, because a full warp requires 4 instruction-cycle to be executed on a SM (32 instances of the same instruction versus 8 SP).

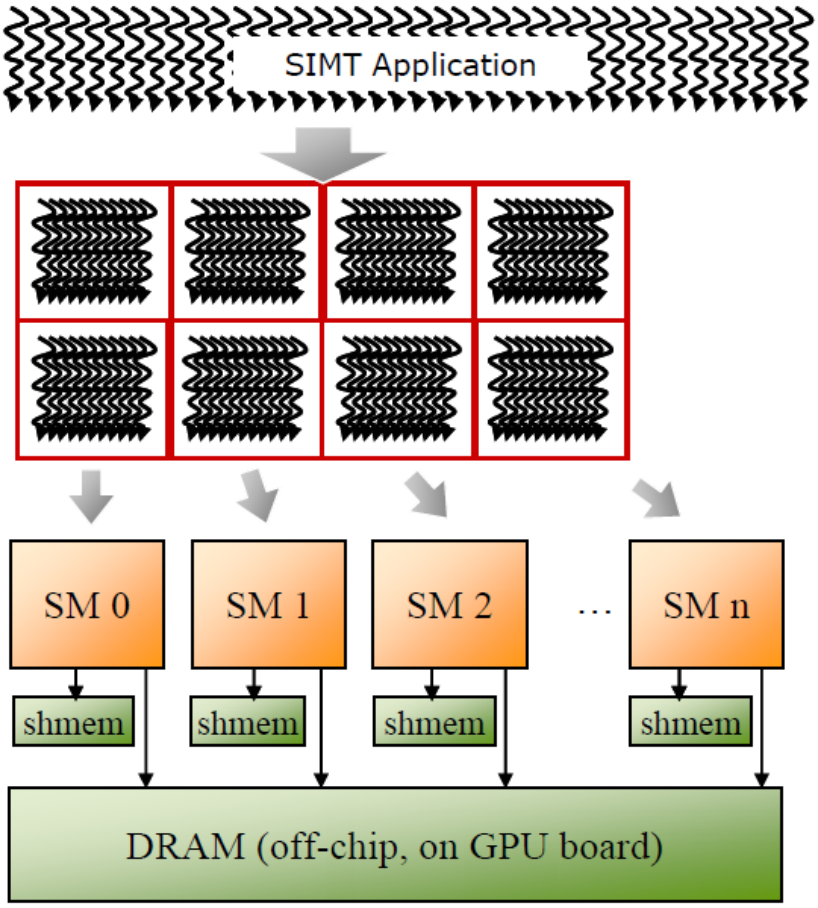

Figure 4.6: *Thread blocks organization and dispatching on SMs.*[5]

In order to hide memory access latencies, the warp execution is not linear; a warp scheduler determines the warps execution order, choosing as many mutually independent instructions stream as possible (fig. 4.8). With this choice 13 warp are required to fully hide latencies to the slowest memory, the off-chip DRAM. However in the Fermi series, where GPU architecture is deeply different from the previous ones, a warp is executed completely in parallel by SPs.

[5]Source: [83]

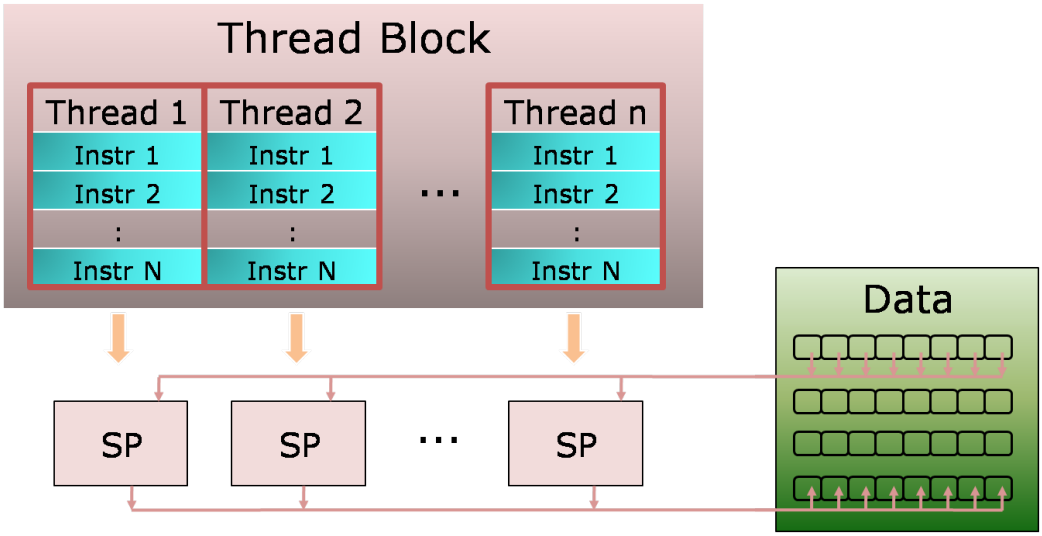

Figure 4.7: *SIMD execution model.*

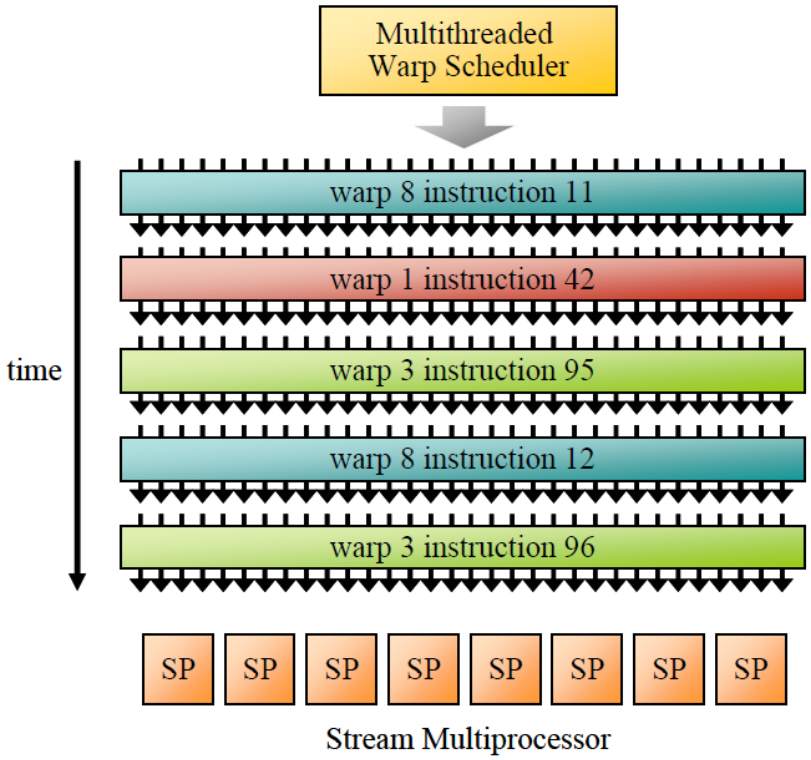

Figure 4.8: *CUDA warp scheduling.*

Memory model

The GPU memory hierarchy (fig. 4.9) strongly influences the application performances and, taking this into account, it is necessary to configure the GPU code in order to limit the overhead of data transfers. Most of the chip area is occupied by arithmetic units, so only a small amount of fast on-chip memory is present, making the GPU a bandwidth limited architecture. Furthermore, data reusage is also difficult due to the lack of a hardware controlled cache hierarchy, with the exception of the last Fermi series.
A local memory is assigned to each thread, which is taken from a set of 16 KB register files, shared by threads in a block. When a thread finishes, its local memory is dislocated. All threads inside a block can share data by a shared memory. As for the local memory, the access to shared memory is fast, and it is organized in banks to allow multiple accesses. The consistence of data is maintained until the relative block is active.
Lowest layer of the hierarchy is the off-chip DRAM (also called *global memory*). The GPU device memory has a high theoretical bandwidth, but requires structured accesses to be very efficient. All thread can access global memory, and data are consistent until the kernel is active; this means that data can not be maintained between two consecutive GPU calls.

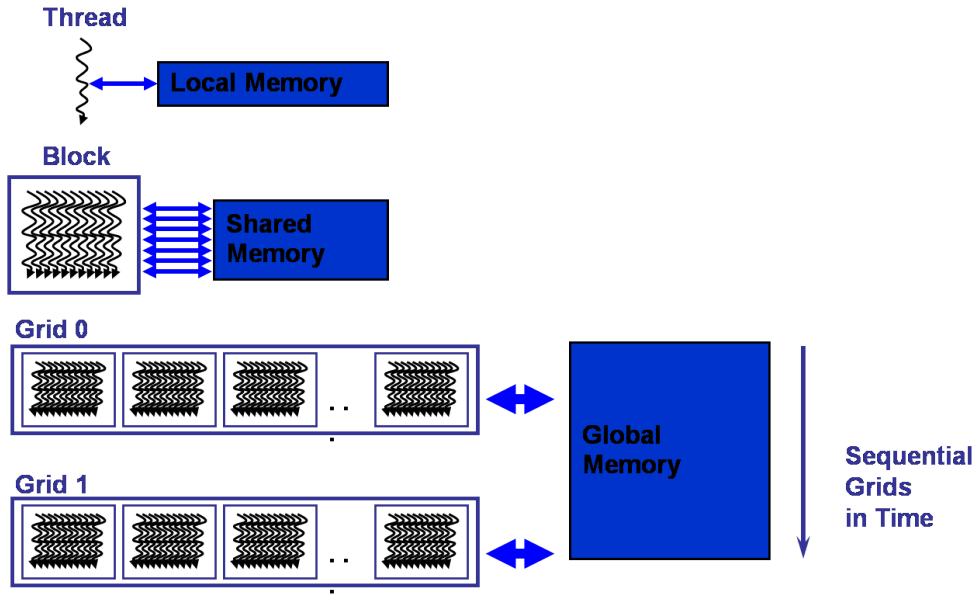

Figure 4.9: *CUDA memory hierarchy.*[6]

[6]Source: NVIDIA

4.2 Algorithms implementation on GPUs

As introduced in Chapter 4.1.2, GPU acceleration is based on extracting critic kernels from the target application and then implementing it on the multi-cores device. For this reason applications are implemented in this work in order to obtain kernels with a high intrinsic parallelism and a regular workflow.

4.2.1 GPUs used

NVIDIA GPUs used are listed in Table 4.1, both with some hardware details. All SMs contains 8 SPs each one, except for Fermi GTX480 where there are 32 SPs for each SM. All board are equipped with a single GPU core, except GTX295 which contains on the same board two GPU cores and two off-chip device memory. Last two columns indicates the throughput in GFLOP/s (Giga FLOP per second) with floating point data in single and double precision.

Model	#TPC	#SM	DRAM (MBytes)	SP throughput (GFLOP/s)	DP throughput (GFLOP/s)
8800 GT™	7	14	512	504	-
GTX 280™	10	30	1024	933	78
GTX 295™	10 *x*2	30 *x*2	896 *x*2	894 *x*2	75 *x*2
GTX 480™	-	15	1536	1345	672

Table 4.1: *GPUs used hardware details.*

4.2.2 EEG implementation on GPU

The EEG implementation on GPU is motivated by two factors: firstly, GPU acceleration is necessary in the EEG forward model implementation with BEM in order to provide for a patient-specific head model within a reasonable time (Chapter 2.5), secondly to provide electrodes data elaboration in *real-time* in sLORETA or SSLOFO algorithms (Chapter 2.7).

Matrix inversion on GPU

The BEM formulation requires computationally intensive matrix operations; however, the highest computational load required is concentrated in the inversion of a large, dense matrix (eq. 2.27). It is well-established that the

dense matrix inversion is a critic algebraic operation, and often it is preferred to avoid it, preferring the usage of different linear system solvers or ad-hoc algorithms, which exploit properties of the matrix (e.g. symmetric matrix). However, this is not always possible, as in our case. Typically, inversion of a general dense matrix is performed in more steps as shown in fig. 4.10: first the matrix is factorized with LU decomposition, then each triangular matrix is inverted separately (which is simpler than inverting a full matrix), and finally the inverse is obtained multiplying the triangular inverses.

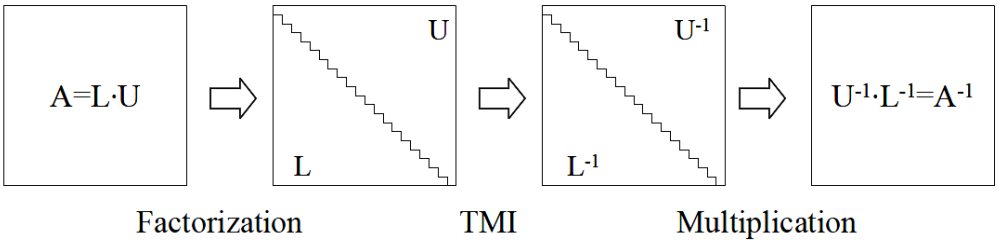

Figure 4.10: *Dense matrix inversion routine.*

GPU implementation for LU factorization just exists [84], and the matrix product is a standard operation well implemented on GPU. Instead no GPU solutions for triangular matrix inversion (TMI) exist.
To exploit the GPU intrinsic parallelism, TMI is implemented following a *divide-and-conquer* approach based on the observation that the inverse of a triangular matrix can be partitioned into three sub-matrices according to the scheme of fig 4.11, where $\boldsymbol{U}$ and $\boldsymbol{L}$ are an upper and lower triangular matrix respectively. As can be shown, portioning the matrix $\boldsymbol{L}$ (or $\boldsymbol{U}$) into a square matrix $\boldsymbol{A}$ and two smaller triangular matrices $\boldsymbol{B}$ and $\boldsymbol{C}$, the relative inverse can be computed assembling the inverses of $\boldsymbol{B}$ and $\boldsymbol{C}$ and a square matrix given by $-\boldsymbol{B}^{-1}\boldsymbol{A}\boldsymbol{C}^{-1}$. Applying this approach recursively, it is possible to perform TMI performing matrix products in parallels. Considering a matrix $\boldsymbol{L}$ of sizes $dim = 2^k \cdot m$ with k integer, it can be partitioned as in fig. 4.12, where mxm triangular matrices are selected along the main diagonal of $\boldsymbol{L}$, and the resting area is divided into square matrices of the sizes m, $2m$, $4m$ $\ldots 2^{k-1}m$. TMI can be so performed as a sequence of parallel matrix products (fig. 4.13): first the inverses of the triangular matrices along the diagonal of $\boldsymbol{L}$ and $\boldsymbol{U}$ are computed (which are small, so inversion is relatively fast and simple), then blocks "1"are so computed using approach shown in fig. 4.11 and so on.
If matrix size dim is not factorisable into the form $dim = 2^k \cdot m$, a padding

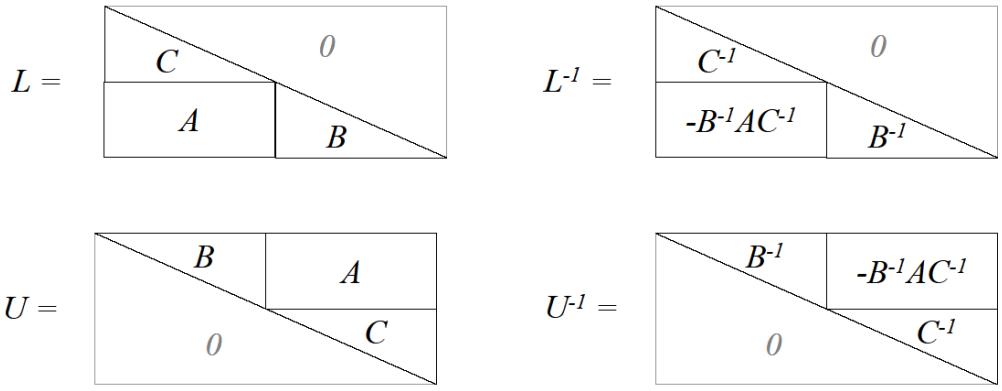

Figure 4.11: *Blocks triangular matrix inversion.*

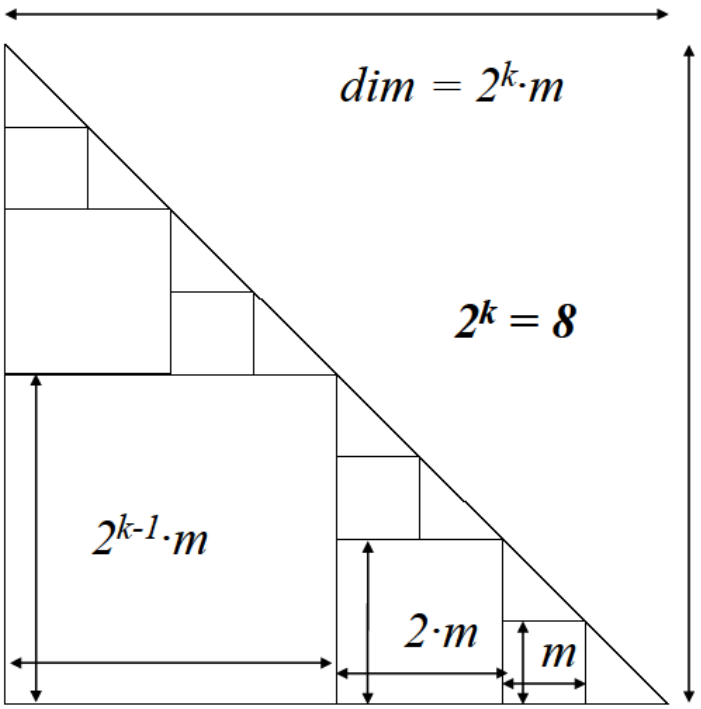

Figure 4.12: *Partitioning of a matrix* $\boldsymbol{L}$ *with k=3.*

procedure is applied, adding identity matrix rows and columns to the original matrix in order to obtain an acceptable matrix size. It is possible to maintain more regular GPU threads this way, avoiding to introduce conditional operators which provokes divergence in the warps execution. Obviously, the relative rows and columns are discarded in the final inverse matrix.

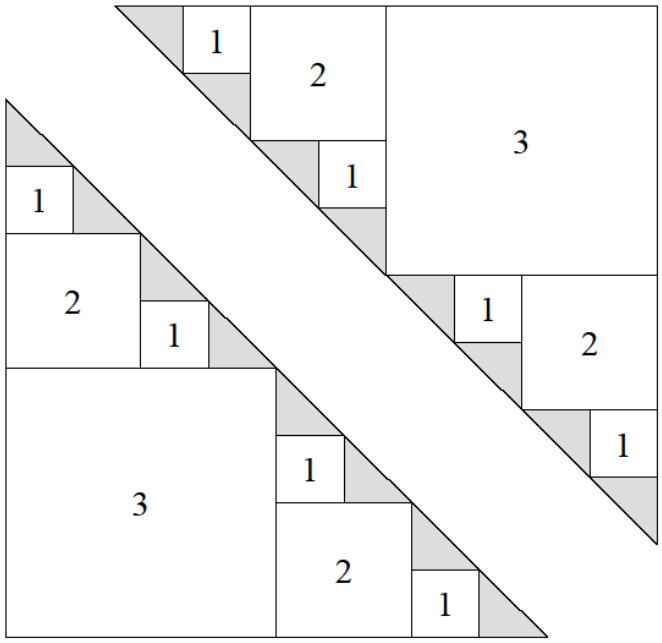

Figure 4.13: *Steps of the TMI algorithm implemented on GPU. Inverse matrix blocks are computed recursively in different steps following the indicated sequence.*

The TMI has been benchmarked on a PC desktop system, equipped with a dual-GPU NVIDIA GTX295 graphics card. GTX295 is a GPU equipped with two cores, so an inversion of a matrix $\boldsymbol{L}$ and $\boldsymbol{U}$ is performed in parallels, one for each core. The hardware configuration used is the following:

- Intel Core2 6300 CPU at 1.86 GHz,
- NVIDIA GTX295 graphics card,
- 4 GB RAM.

Execution performances were compared to that of a dualCPU-only reference based on standard FORTRAN library of LAPACK, obtaining speedup up to 60x. Fig. 4.14 shows the computation time required by the two solutions with matrices of variable size.

SSLOFO implementation on GPU

The EEG inverse problem multi-core implementation is based on the acceleration of the SSLOFO estimator on GPU (Chapter 2.7). The main steps of

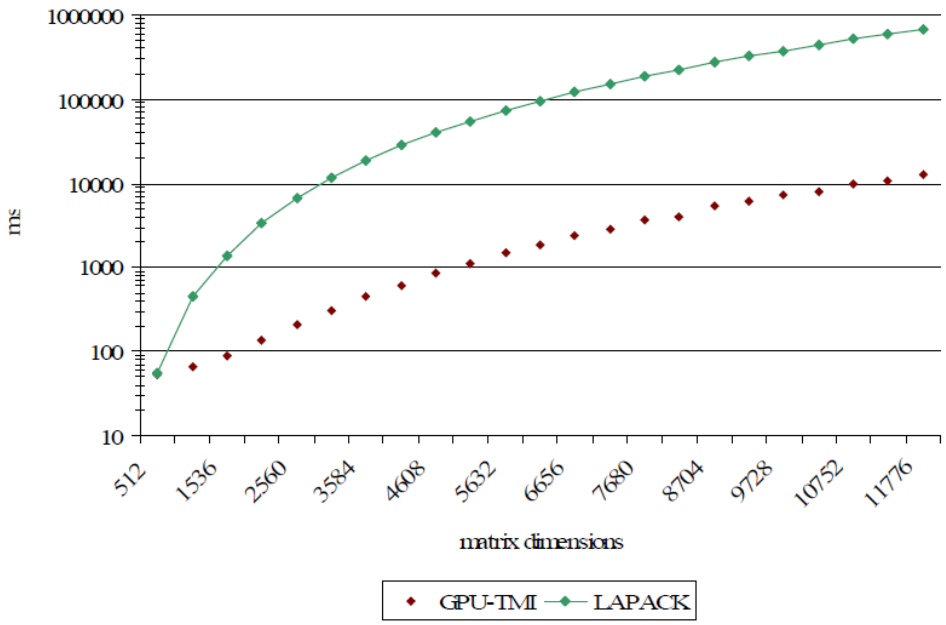

Figure 4.14: *Execution times of GPU TMI and the LAPACK based dual-CPU reference.*

the SSLOFO solver are shown in fig. 4.15.
Being a massively parallel processor, the GPU needs to run thousands of independent threads to work at full efficiency. Moreover, the architecture prefers high arithmetic-to-data ratios as the off-chip DRAM memory tends to have a significant transfer access delay and the host-device communication is outright stalling the computation flow. Conveniently, most parts of the algorithm can be parallelized very efficiently, making it suitable for this kind of hardware implementation.
The evaluation of each single voxel can be processed independently by a dedicated thread. This includes the initial solution calculated by sLORETA (fig. 4.15, step 1), the standardized iterative solution (8), calculation and readjustment of the weighting matrix (3), the shrinking of the solution space (10) and smoothing (9). The threads have been bundled into blocks of 32 threads to comply with the warp size of the SMs, while still generating enough thread blocks to at least partially hide the inevitable global memory access delays by using pipelined warp scheduling.
The process of building the inverse estimator, however, must be addressed differently. The first matrix multiplication (4) can still be significantly accelerated by splitting the problem into multiple subsets, processing them in parallels and reassembling them. Matrix inversion (5) is performed on

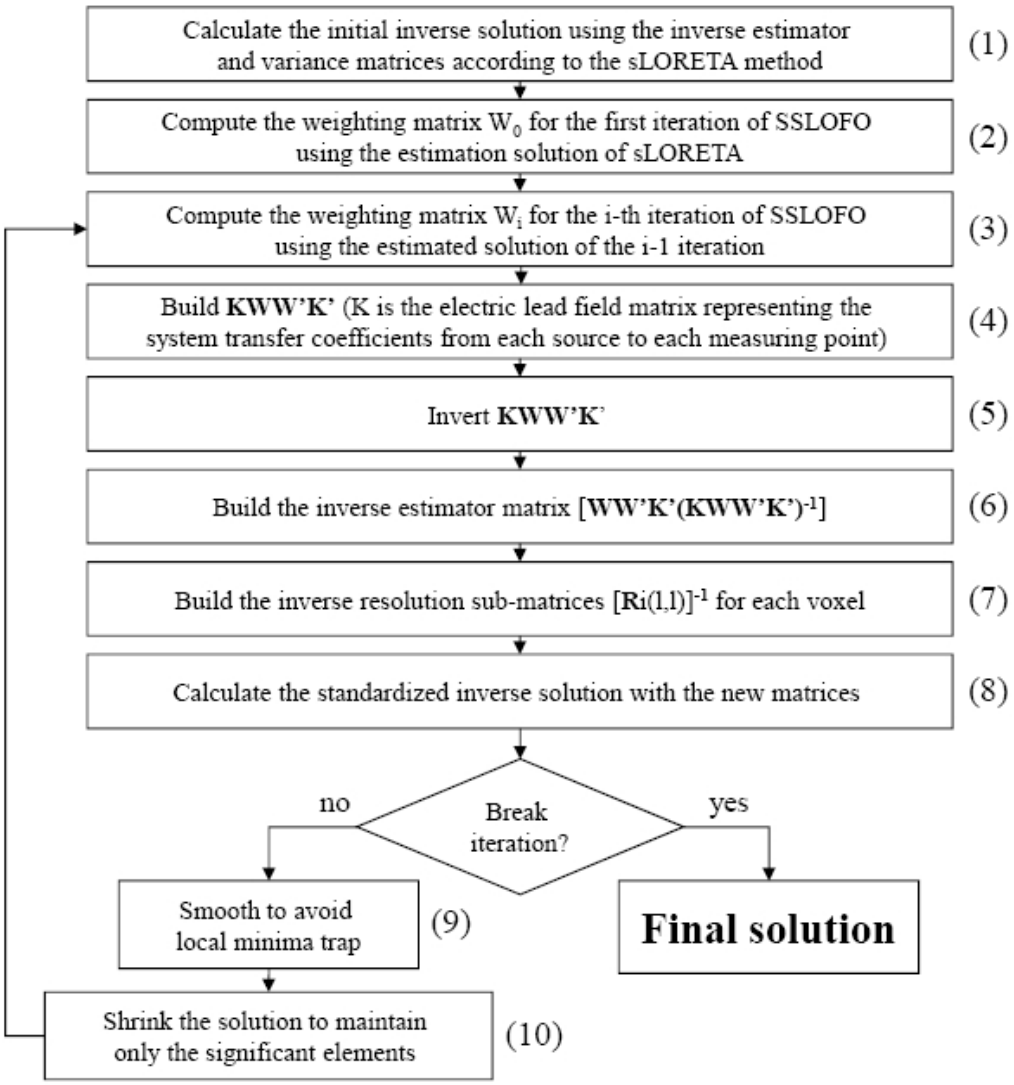

Figure 4.15: *SSLOFO algorithmic workflow.*

the CPU. The small size of the matrix (its rank is equal to the number of electrodes) makes it impracticable to invert on the massively parallel GPU. Even the additional host-device transfers introduce only a negligible overhead quantifiable in the order of μs. For the inversion, a Cholesky decomposition is performed, followed by a triangular matrix inversion. The square of this inverse yields the inverse of the full matrix. Completing the inverse estimator matrix (6) can again be parallelized on a one-thread-per-voxel basis. However, this step remains the heaviest part of the implementation due to its huge arithmetic complexity and the large size of input and output data

involved. Around 50% of the computation time is spent in this step. The FOCUSS estimator is completed by construction of the standardization matrices, which again can be done for each voxel independently, i.e. in parallel (7).
Table 4.2 shows the distribution of the computational load of the individual sub-tasks, with reference to the steps explained in fig. 4.15.

Sub-task	%
Calculate W_i and shrink (3)(10)	0.49
$KWWK^{'}$ on GPU (4)	26.10
Merging segments (4)	0.28
Invert $KWWK^{'}$ on CPU including up-/download (5)	3.68
Inverse estimator matrix $WWK^{'}(KWWK^{'})^{-1}$ (6)	55.22
Standardization matrices R_i^{-1} (7)	5.74
Standardized inverse solution (8)	3.36
Smoothing (9)	5.13

Table 4.2: *Computational load of SSLOFO sub-tasks.*

Only parts inside the iteration loop were considered. As already mentioned above, the assembly of the inverse estimator matrix takes the biggest share. With around 25% the $\boldsymbol{KWWK^{'}}$ matrix multiplication still has a significant impact. All other sub-tasks introduce only a moderate work load. Furthermore, the host-device communication per timeframe remains negligibly low, in the order of a few hundred microseconds. In addition to the matrix upload and download involved in the matrix inversion step, the application needs to upload the sensor data only once, and to download the standardized current density powers only once per iteration. All other data can be uploaded before starting the real-time processing. It should be noted that the sLORETA related matrices and the lead field $\boldsymbol{K}$ are pre-loaded into the device memory before starting computation. An update of these matrices during the execution is in fact not necessary.
Hardware configuration used in the simulations is the following:

- Intel Core 2 Quad CPU,
- GPU NVIDIA GeForce 8800 GT,
- 4 GB of DDR2-SDRAM.

In order to evaluate the performance of our architecture, we worked with different voxels densities to explore different resolution levels, and different

electrode configurations. In our algorithmic implementation, we apply a fixed number of iterations for the solution of the non linear problem. In the following results, we were using two iterations, since we already observed significant improvements over sLORETA while still meeting real-time requirements for most configurations. Referring to the temporal requirement of a BCI system, characterized by a feedback time in the order of 100-200 ms, a number of 10 frames per second (FPS) was taken as the minimum threshold to define a real-time constraint. A frame here refers the complete evaluation of the source distribution for one time instant. In Table 4.3 and Table 4.4 results collected from CPU + GPU and CPU only computation are showed, in terms of FPS obtained considering 32, 64 and 128 electrodes with voxel resolutions from 3939 to 32032 point sources.

Voxels \ Electrodes	32	64	128
3939	**98.30**	**21.15**	5.09
6430	**77.79**	**17.42**	4.12
8068	**60.82**	**13.95**	3.36
12980	**40.13**	9,64	2.32
15860	**32.20**	8.07	1.99
32032	**19.11**	4.51	1.05

Table 4.3: *Frames per Second provided by GPU acceleration.*

Voxels \ Electrodes	32	64	128
3939	**13.92**	3.86	0.70
6430	6.66	1.50	0.23
8068	6.56	1.48	0.20
12980	2.26	0.43	0.08
15860	1.06	0.53	0.09
32032	0.94	0.23	0.04

Table 4.4: *Frames per Seconds provided by the CPU stand alone.*

The number of electrodes was chosen to reflect commonly used commercial EEG recording caps. The voxel resolutions were selected to be compliant with the range found in the literature. Configurations matching real-time requirements are highlighted. As can be seen, the usage of only one CPU-GPU bundle allows us to elaborate data from 64 electrodes in real-time with

a maximum resolution of 8068 voxels, and data from 32 electrodes with all the voxel densities we used in this test. On the other hand, using a CPU-only implementation enables us to elaborate data from 32 electrodes in real time with a maximum resolution of no more than 3939 voxels. As we can see, with the help of the GPU we are able to run an efficient algorithm to solve the EEG inverse problem for most of the contemporarily used electrode-voxel configurations, considering that the 128 electrode montage is rarely applied in the field. A comparable implementation is not achievable with a CPU-only solution. If we consider, for example, a configuration with 64 electrodes and 8068 voxels it is possible to elaborate EEG data with around 14 frames per second, which is enough to support a BCI system. On the contrary, using a CPU-only system, the number of FPS available with the same electrodes-voxels configuration is around 1.5; so in this case the speed-up between the two architectures is around 10x.

Obtained FPS allows usage of GPU-accelerated SSLOFO using electrode-voxel configurations typically found in literature. However considering head models with higher resolution (> 100000 voxels), this solver does not allow to obtain enough performances to satisfy real-time constraints. Nevertheless, it is important to highlight that the GPU used in this analysis is not at the state of the art at the time of writing, as it is shown in Table 4.1; consequently usage of most recent GPUs can results in higher performances. In fact, according to our evaluations, considering the limited data exchange between CPU and GPU, the performance could scale linearly with the number of SMs in the GPU utilized, allowing real time elaboration for even higher numbers of electrodes and voxel densities. Simulations of stand alone GPU-accelerated sLORETA shows instead as it is possible to satisfy real time constraints also for head model with 200000 voxels.

4.2.3 EIT solving on GPU

As previously explained, implementation of applications on GPU require the definition of regular and homogeneous threads, in order to prevent warp divergences during the elaboration. Overhead introduced by memory accesses, especially if unstructured, reduces the obtainable performances. For this reasons, our EIT forward problem (Chapter 3.4.4) is implemented in order to result in a diagonal forward matrix with 19 bands instead of a general sparse matrix. This is obtained through a high resolution head model based on structured meshes; also the tissues anisotropy and the realistic modeling of the electrodes are implemented preserving the regular structure of the resulting matrix. That way, the GPU implementation of the BiConiugate

Gradient Method (Chapter 3.4.5) can be done with more regular threads, limiting warp divergences and reducing the amount of the data transfer between GPU and the rest of the system. The algorithmic details of the BiCG implementation on GPU are presented in [85].
In the scope of this work, we used a system with two NVIDIA GeForce GTX 480 GPUs. Our system configuration summarizes to:

- Two Intel Xeon E5520 CPUs at 2.4 GHz,
- Two GPU NVIDIA Fermi GTX 480,
- 24 GB RAM

all of which are run-of-the-mill hardware components. The general system setup is depicted in fig. 4.16.

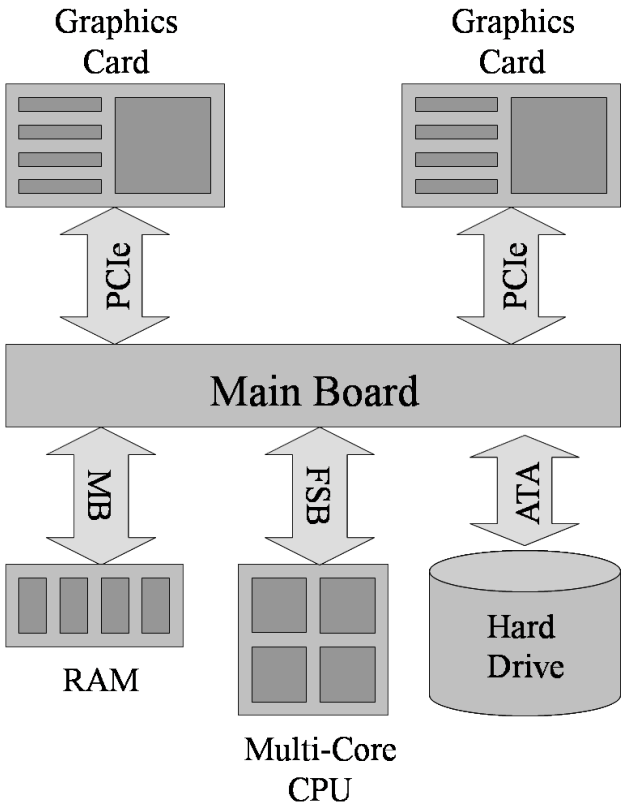

Figure 4.16: *General setup of a dual-GPU accelerated desktop machine, including a multi-core CPU connected via front side bus (FSB). The GPUs are connected via PCI express interfaces.*

In fig. 4.17, a profiling of the framework is showed. Computation of EIT

forward model matrix $\boldsymbol{A}$ with a head model of 5.2 million voxels is performed with MATLAB® in around 20 seconds. The banded structure of $\boldsymbol{A}$ makes an overhead of about 7s for the data transfers between the RAM of the system and the GPUs memory. This hardware-accelerated solver achieves a computational throughput of around 220 million nodes per second for a 19 band linear system like the one at hand. A sufficiently precise solution with a relative residual lower than 10^{-6} can be obtained after 700 iterations, so in a mid-sized setup spanning 5.2 million FVM elements, all the calculations are done in about twenty seconds. This is about two orders of magnitude faster than non-accelerated implementations based on a MATLAB or even an optimized parallel C-code (fig. 4.17). Even for larger problems, computation times can generally be kept in the range of tens of seconds. This allows a level of detail for the simulation that would be unfeasible with non-parallel methods.
Since several forward problems need to be usually solved for the same matrix $\boldsymbol{A}$ but a different right hand side, e.g. when solving an EIT inverse problem, the overhead due to matrix generation and transfer gets rapidly negligible for an increasing problem number. In particular, the solution of the 5.2 million elements problem for 64 different right hand sides takes about 850 s, allowing the computation of a Jacobian matrix for the EIT inverse problem solution in about 15 minutes with 64 electrodes, and 1 hour with 256 electrodes.

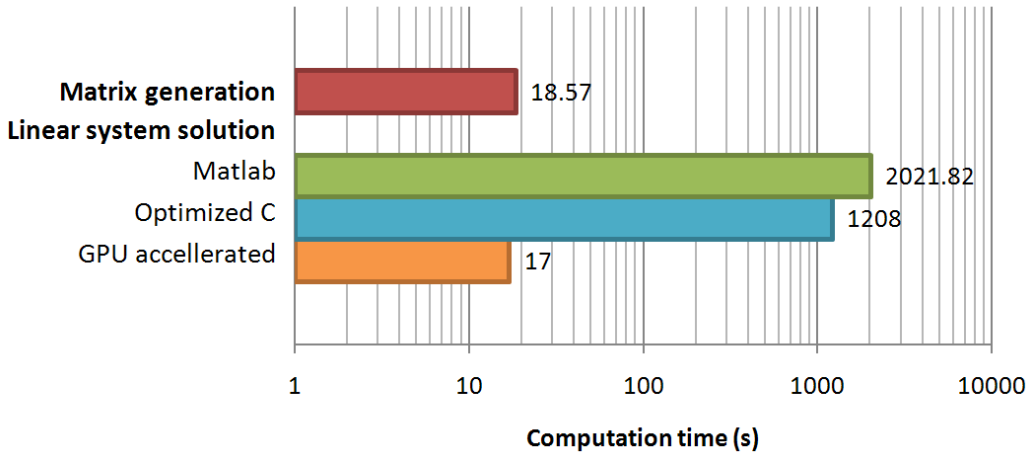

Figure 4.17: *Computation times in seconds for matrix generation on MATLAB and solution of a problem with 5.2 million elements within 700 iterations, as required by implementations based on MATLAB, optimized parallel C-code and the GPU-accelerated solver.*

Chapter 5

Discussion

This thesis is focused on the parallel modeling of the electric field distribution inside the brain. Studied techniques are EEG and EIT, with particular attention to their usage for brain imaging. These techniques are characterized by an high temporal resolution and a portable acquisition hardware. However both in EEG and EIT, relative simplicity of the acquisition hardware is balanced by the heavy computational load required in data elaboration. In order to provide acceptable simulations times in the simulations and data elaboration, algorithms implemented are accelerated on GPU-based desktop PC, a multi-core solution able to provide computational power in parallel data elaboration comparable with super-computing solution, maintaining lower costs.

In Chapter 2, a complete framework for EEG data elaboration is presented. The volume conductor model is based on an MRI description of the subject head. Data are elaborated with a BEM implementation based on a compartmental description of the tissues, providing a realistic patient specific head model. Isolated skull approach (ISA) is used in the numeric implementation to reduce numerical errors due to the high conductivity difference between skull and adjacent tissues. The derived BEM solver is accelerated using a GPU-based multi-core platform, focusing on the matrix operations involved, which are highly time-consuming, such as the inverse computing of large dense matrix. With this approach, a dense matrix of 10000x10000 elements can be inverted in less than a minute, with a speed-up of 60x respect to a standard LAPACK solution.
The obtained head model is used in the successive EEG inverse problem computation. The solver used in this step is SSLOFO, which combines the well-known, high performances sLORETA, with FOCUSS, a iterative non-linear method able to provide source reconstruction with an high level of

focalization as shown in fig. 2.11. The inverse problem solver has been implemented on GPU-based desktop PC, in order to obtain a fast solution able to compute data recorded by electrodes in real-time, which is a necessary constraint in many applications, e.g. BCIs.

In Chapter 3, a complete framework for EIT forward problem solution and computation of the jacobian matrix to solve the inverse problem with a linearized approach are presented. The volume conductor modeling is based on an FVM discretization of the human head, which makes use of full MRI resolution to maximize the detail level of the fine-grained non homogeneity of human tissues and accounts for anisotropy and dielectric properties using a complex tensor description. The model is completed by a novel electrode model which takes into account contact impedance and the finite size of the electrodes. We have shown how the introduction of these features leads to different results with respect to standard over-simplified models, justifying the introduction of such features. The framework is designed to provide unprecedented anatomical precision, without sacrificing performance, thanks to a tuned combination of hardware and software design. Our model features a linear dependence between injected currents and measured voltages, so results are linearly scalable. Simulations are performed using typical values obtained from literature, which are indicative of pathological diseases. For an epileptic focus of limited volume [56], simulation results show that the difference of potentials induced on the scalp is influenced by the distance from the injecting electrode for depths of up to about 4 cm. If white matter were considered isotropic, recorded voltage magnitudes would be influenced only by the distance between active electrodes and the active region, rather than by the actual relative position. This is not true when anisotropy is taken into account; in particular, due to the mainly radial distribution of white matter fibers, preferential current patterns tend to be localized in this direction. Therefore, active regions along these preferential patterns tend to affect surface potentials more significantly. It seems to be reasonable to distribute active and passive electrodes uniformly on the scalp, in particular using active electrodes placed at opposite sites, in order to maximize current flow in the radial direction and to reduce the shunting effect of the scalp. In fig. 3.14, it is shown that potential variations scale almost linearly with the size of the active region and that the noise levels of state of the art analog circuits [75] can detect active regions smaller than 1 cm^3 (less than a few μV with 1 mA of injected current), which can be indicative of brain lesions. With respect to typical non-idealities which are not accounted for in classical EIT models, we have shown how significant errors are derived from the erroneous assumption of isotropic behavior in white matter (fig. 3.17) and

from neglecting electrode size. Standard approximations can easily lead to errors in the system design (e.g., leading to the assumption that the higher the number of electrodes, the better), in best current pattern choices (which should consider tissue anisotropy and electrode properties) and in the solution of the inverse problem based on them. The forward problem solver has a spatial resolution 10-100 times bigger than other available solutions [9][59][60] and, in contrast to standard forward problem solvers, it accounts for tissue anisotropy and realistic electrode models. In term of computational efficiency, we have shown the benefits of algorithms exploiting GPU based platforms. With respect to [9], for which 321 s are required to a parallel FEM solver running on an octal Xeon 5355 based server for solving 64 EIT forward problem with the same matrix and a 150000 node grid, we are able to use a much more detailed mesh (more than 5 million nodes) and to account for anisotropy with a computation time less than 3 times larger.
Achieved performances directly influences Jacobian matrix computation, necessary for the EIT inverse problem solving with linearized methods. Thanks to the application of the reciprocity principle Jacobian matrix computation is achieved by solving as many forward model simulations as the electrodes number. Time required by the additional operations is negligible.
Application of this solver allows to easily perform simulations aimed to configure at best EIT instrumentation. To this purpose an algorithmic work flow is introduced to take into account effects of electrical noise due to brain neurons activity, showing as they can be of the same magnitude of the thermal noise given by electrodes contact impedance.
The implemented solver is applied to the solution of the EIT forward problem, but can be easily applied to similar applications, such as estimating the injected current paths of Transcranial Direct Current Stimulation (tDCS) [86] or, with minor modifications, the EEG source localization forward problem exploiting the reciprocity principle used for noise analysis. Using this approach in fact, nodes in the head model can be collected in terms of current dipoles, considering adjacent nodes along Cartesian direction of the space as the components of each current density associated to the dipoles. Differently from BEM implementation, this approach allows the introduction of conductivity anisotropy and realistic electrode model in the EEG brain model. Moreover, achieved resolution is considerable higher than that provided by BEM, because it is based on full matrix operations whose sizes is given by the number of elements in the meshes used. Consequently, the finite size of the memory reduces the anatomical details acceptable. On the contrary a FVM solution is based on sparse matrix operations, which are in general more computationally onerous than dense matrix ones, but allows a better usage of the memory space.

Conclusions

This work is focused on the parallel modeling of the electric field distribution inside the brain. Techniques studied are EEG and EIT, with particular attention to their usage for brain imaging purposes. These techniques are characterized by an high temporal resolution and a portable acquisition hardware. These properties make them complementary to high spatial resolution techniques (such as fMRI) in a medical context, and allows their usage in others applications as BCI, where hardware portability and temporal resolution are mandatory. However both in EEG and EIT, the relative simplicity of the acquisition hardware is balanced by the heavy computational load required in data elaboration. In order to provide acceptable simulation times in the data elaboration, algorithms implemented are accelerated on GPU-based desktop PC, a multi-core solution able to provide computational power in parallel data elaboration comparable with super-computing solutions, maintaining lower costs.

A complete framework for EEG data elaboration has been realized based on an MRI description of the subject head. Data are elaborated with a BEM implementation based on a meshes compartmental description of the tissues, providing a realistic patient specific head model. Code implementation on a GPU shows improvements up to 60x referring to a solution based on standard multi-core general purpose processor.

EEG inverse problem is solved by SSLOFO, a solver which combines the well-known, high performances sLORETA, with FOCUSS, an iterative non-linear method able to provide source reconstruction with an high level of focalization. Inverse problem solver has been implemented targeting GPU-based desktop PC, in order to obtain a fast solution able to compute the solution from data recorded by electrodes in real-time, which is a necessary constraint in many applications, such as BCIs.

A complete framework for EIT forward problem solution has also been implemented. The volume conductor modeling is based on an FVM discretization of the human head, which makes use of full MRI resolution to maximize the detail level of the fine-grained non homogeneity of human tissues

and accounts for anisotropy and dielectric properties using a complex tensor description. The model is completed by a novel electrode model which takes into account contact impedance and the finite size of the electrodes, without increasing complexity of the solver. We have shown how the introduction of these features leads to different results with respect to standard over-simplified models, justifying the introduction of such features. The framework is designed to provide unprecedented anatomical precision, without sacrificing performance, thanks to a tuned combination of hardware and software design.
Improvements given by GPU acceleration are also presented referring to Jacobian matrix computation necessary to solve EIT inverse problem.
Additionally, a procedure to evaluate noise induced by neuronal activity on the electrodes measures is presented. This is based on application of reciprocity principle to EIT forward problem, however results are valid in general for any electrical measures of scalp potential with passive high impedance electrodes (like in EEG).

Paper submissions

The following papers have been co-authored and are currently submitted for publication awaiting reviews.

- **T. De Marco, F. Ries, M. Guermandi, R. Guerrieri** - EIT Forward Problem Parallel Simulation Environment with Anisotropic Tissue and Realistic Electrode Models - *IEEE Transactions on Biomedical Engineering (TBME).*

- **F. Ries, T. De Marco, R. Guerrieri** - Solving Large Non-Hermitian Linear Systems on Multi-GPU Accelerated Workstations - *IEEE Transactions on Parallel and Distributed Systems (TPDS).*

The following papers have been co-authored and are accepted for publication.

- **F. Ries, T. De Marco, R. Guerrieri** - Triangular Matrix inversion on Heterogeneous Multicore Systems - In PrePrints, to appear in *IEEE Transactions on Parallel and Distributed Systems (TPDS).*

- **F. Ries, T. De Marco, M. Zivieri, R. Guerrieri** - Triangular matrix inversion on Graphics Processing Unit - *Proceedings of the Conference on High Performance Computing Networking, Storage and Analysis (SC '09)*, pp.1-10, 2009.

Bibliography

[1] E.R. Kandel, J.H. Schwartz, T.M. Jessell, S. Mack, and J. Dodd. *Principles of neural science*, volume 3. Elsevier New York, 1991.

[2] E. Lindholm, J. Nickolls, S. Oberman, and J. Montrym. NVIDIA Tesla: A unified graphics and computing architecture. *Micro, IEEE*, 28(2):39–55, 2008.

[3] T. Vaughan, L. DelaBarre, C. Snyder, J. Tian, C. Akgun, D. Shrivastava, W. Liu, C. Olson, G. Adriany, J. Strupp, et al. 9.4 T human MRI: preliminary results. *Magnetic Resonance in Medicine*, 56(6):1274–1282, 2006.

[4] J.H. Duyn, P. Van Gelderen, T.Q. Li, J.A. De Zwart, A.P. Koretsky, and M. Fukunaga. High-field MRI of brain cortical substructure based on signal phase. *Proceedings of the National Academy of Sciences*, 104(28):11796, 2007.

[5] D. Le Bihan, J.F. Mangin, C. Poupon, C.A. Clark, S. Pappata, N. Molko, and H. Chabriat. Diffusion tensor imaging: concepts and applications. *Journal of magnetic resonance imaging*, 13(4):534–546, 2001.

[6] S.G. Kim, W. Richter, and K. Ugurbil. Limitations of temporal resolution in functional MRI. *Magnetic Resonance in Medicine*, 37(4):631–636, 1997.

[7] P.L. Nunez and R. Srinivasan. *Electric fields of the brain: the neurophysics of EEG*. Oxford University Press New York, 2006.

[8] RH Bayford. Bioimpedance tomography (electrical impedance tomography). *Biomedical Engineering*, 8(1):63–91, 2006.

[9] A. Borsic, A. Hartov, K.D. Paulsen, and P. Manwaring. 3D electric impedance tomography reconstruction on multi-core computing platforms. In *Engineering in Medicine and Biology Society, 2008. EMBS*

2008. 30th Annual International Conference of the IEEE, pages 1175–1177. IEEE, 2008.

[10] J. Malmivu and R. Plonse. Bioelectromagnetism–Principles and Applications of Bioelectric and Biomagnetic Fields, 1995.

[11] M. Modarreszadeh and R.N. Schmidt. Wireless, 32-channel, EEG and epilepsy monitoring system. In *Engineering in Medicine and Biology Society, 1997. Proceedings of the 19th Annual International Conference of the IEEE*, volume 3, pages 1157–1160. IEEE, 2002.

[12] L. Horesh, O. Gilad, A. Romsauerova, A. McEwan, SR Arridge, and DS Holder. Stroke type differentiation by multi-frequency electrical impedance tomography – a feasibility study. *Proc. IFMBE*, 11, 2005.

[13] D. Holder. *Electrical impedance tomography: methods, history, and applications*. Taylor & Francis, 2005.

[14] M. Teplan. Fundamentals of EEG measurement. *Measurement Science Review*, 2(2):1–11, 2002.

[15] A. Manwani and C. Koch. Detecting and estimating signals in noisy cable structures, I: Neuronal noise sources. *Neural computation*, 11(8):1797–1829, 1999.

[16] H. Hallez, B. Vanrumste, R. Grech, J. Muscat, W. De Clercq, A. Vergult, Y. D'Asseler, K.P. Camilleri, S.G. Fabri, S. Van Huffel, et al. Review on solving the forward problem in EEG source analysis. *Journal of NeuroEngineering and Rehabilitation*, 4(1):46, 2007.

[17] R.M. Gulrajani. *Bioelectricity and biomagnetism*. Wiley New York, 1998.

[18] E. Niedermeyer and F.H.L. Da Silva. *Electroencephalography: basic principles, clinical applications, and related fields*. Lippincott Williams & Wilkins, 2005.

[19] E. Niedermeyer and F.H.L. Da Silva. *Electroencephalography: basic principles, clinical applications, and related fields*. Lippincott Williams & Wilkins, 2005.

[20] C.M. Michel, G. Lantz, L. Spinelli, R.G. de Peralta, T. Landis, and M. Seeck. 128-channel EEG source imaging in epilepsy: clinical yield and localization precision. *Journal of Clinical Neurophysiology*, 21(2):71–83, 2004.

[21] H. Robot. Clinical application of an EEG-based brain-computer interface: a case study in a patient with severe motor impairment. *Clinical Neurophysiology*, 114:399–409, 2003.

[22] F. Masterpasqua and K.N. Healey. Neurofeedback in psychological practice. *Professional Psychology Research and Practice*, 34(6):652–656, 2003.

[23] J.E. Walker and G.P. Kozlowski. Neurofeedback treatment of epilepsy. *Child and adolescent psychiatric clinics of North America*, 14(1):163–176, 2005.

[24] D. Vernon, T. Egner, N. Cooper, T. Compton, C. Neilands, A. Sheri, and J. Gruzelier. The effect of training distinct neurofeedback protocols on aspects of cognitive performance. *International Journal of Psychophysiology*, 47(1):75–85, 2003.

[25] J. Gruzelier, T. Egner, and D. Vernon. Validating the efficacy of neurofeedback for optimising performance. *Progress in brain research*, 159:421–431, 2006.

[26] J.N. Mak and J.R. Wolpaw. Clinical Applications of Brain-Computer Interfaces: Current State and Future Prospects. *Biomedical Engineering, IEEE Reviews in*, 2:187–199, 2009.

[27] B. Blankertz, M. Tangermann, C. Vidaurre, S. Fazli, C. Sannelli, S. Haufe, C. Maeder, L. Ramsey, I. Sturm, G. Curio, et al. The Berlin Brain–Computer Interface: Non-Medical Uses of BCI Technology. *Frontiers in neuroscience*, 4, 2010.

[28] C. Guger and G. Edlinger. The First Commercial Brain–Computer Interface Environment. *Brain-Computer Interfaces*, pages 281–303, 2010.

[29] B. Vanrumste, G. Van Hoey, R. Van de Walle, M.R.P. D'Havé, I.A. Lemahieu, and P.A.J.M. Boon. Comparison of performance of spherical and realistic head models in dipole localization from noisy EEG. *Medical engineering & physics*, 24(6):403–418, 2002.

[30] G. Huiskamp, M. Vroeijenstijn, R. van Dijk, G. Wieneke, and A.C. van Huffelen. The need for correct realistic geometry in the inverse EEG problem. *Biomedical Engineering, IEEE Transactions on*, 46(11):1281–1287, 2002.

[31] Gang Wang, Gregory Worrell, Lin Yang, Christopher Wilke, and Bin He. Interictal spike analysis of high-density eeg in patients with partial epilepsy. *Clinical Neurophysiology*, In Press, Corrected Proof, 2010.

[32] N. Chauveau, X. Franceries, B. Doyon, B. Rigaud, J.P. Morucci, and P. Celsis. Effects of skull thickness, anisotropy, and inhomogeneity on forward EEG/ERP computations using a spherical three-dimensional resistor mesh model. *Human brain mapping*, 21(2):86–97, 2004.

[33] R. Plonsey and D.B. Heppner. Considerations of quasi-stationarity in electrophysiological systems. *Bulletin of Mathematical Biology*, 29(4):657–664, 1967.

[34] B. He, T. Musha, Y. Okamoto, S. Homma, Y. Nakajima, and T. Sato. Electric dipole tracing in the brain by means of the boundary element method and its accuracy. *Biomedical Engineering, IEEE Transactions on*, 34(6):406–414, 2007.

[35] M. Fuchs, R. Drenckhahn, H. Wischmann, and M. Wagner. An improved boundary element method for realistic volume-conductor modeling. *Biomedical Engineering, IEEE Transactions on*, 45(8):980–997, 2002.

[36] C.R. Johnson. Numerical methods for bioelectric field problems. *The biomedical engineering handbook*, pages 162–180, 1995.

[37] H. Hallez, B. Vanrumste, P.V. Hese, Y. D'Asseler, I. Lemahieu, and R.V. Walle. A finite difference method with reciprocity used to incorporate anisotropy in electroencephalogram dipole source localization. *Physics in medicine and biology*, 50:3787–3806, 2005.

[38] S. Rush and DA Driscoll. EEG electrode sensitivity–an application of reciprocity. *IEEE transactions on bio-medical engineering*, 16(1):15–22, 1969.

[39] RD Pascual-Marqui. Standardized low-resolution brain electromagnetic tomography (sLORETA): technical details. *Methods Find Exp Clin Pharmacol*, 24(Suppl D):5–12, 2002.

[40] S. Baillet, JC Masher, and R.M. Leahy. Electromagnetic brain imaging using brainstorm. In *Biomedical Imaging: Nano to Macro, 2004. IEEE International Symposium on*, pages 652–655. IEEE, 2005.

[41] B. Fischl, A. Liu, and A.M. Dale. Automated manifold surgery: constructing geometrically accurate and topologically correct models of the human cerebral cortex. *Medical Imaging, IEEE Transactions on*, 20(1):70–80, 2002.

[42] A.M. Dale, B. Fischl, and M.I. Sereno. Cortical Surface-Based Analysis* 1:: I. Segmentation and Surface Reconstruction. *Neuroimage*, 9(2):179–194, 1999.

[43] M.S. Lynn and W.P. Timlake. The use of multiple deflations in the numerical solution of singular systems of equations, with applications to potential theory. *SIAM Journal on Numerical Analysis*, 5(2):303–322, 1968.

[44] M.S. Hamalainen and J. Sarvas. Realistic conductivity geometry model of the human head for interpretation of neuromagnetic data. *Biomedical Engineering, IEEE Transactions on*, 36(2):165–171, 2002.

[45] MS Hämäläinen and RJ Ilmoniemi. Interpreting magnetic fields of the brain: minimum norm estimates. *Medical and Biological Engineering and Computing*, 32(1):35–42, 1994.

[46] C.L. Lawson and R.J. Hanson. *Solving least squares problems*. Society for Industrial Mathematics, 1995.

[47] RE Greenblatt. Probabilistic reconstruction of multiple sources in the bioelectromagnetic inverse problem. *Inverse problems*, 9:271, 1993.

[48] RD Pascual-Marqui, M. Esslen, K. Kochi, and D. Lehmann. Functional imaging with low resolution brain electromagnetic tomography (LORETA): review, new comparisons, and new validation. *Japanese Journal of Clinical Neurophysiology*, 30:81–94, 2002.

[49] I.F. Gorodnitsky, J.S. George, and B.D. Rao. Neuromagnetic source imaging with FOCUSS: a recursive weighted minimum norm algorithm. *Electroencephalography and clinical Neurophysiology*, 95(4):231–251, 1995.

[50] H. Liu, P.H. Schimpf, G. Dong, X. Gao, F. Yang, and S. Gao. Standardized shrinking LORETA-FOCUSS (SSLOFO): a new algorithm for spatio-temporal EEG source reconstruction. *Biomedical Engineering, IEEE Transactions on*, 52(10):1681–1691, 2005.

[51] H. Liu, X. Gao, P.H. Schimpf, F. Yang, and S. Gao. A recursive algorithm for the three-dimensional imaging of brain electric activity: shrinking LORETA-FOCUSS. *Biomedical Engineering, IEEE Transactions on*, 51(10):1794–1802, 2004.

[52] M. Cheney, D. Isaacson, and J.C. Newell. Electrical impedance tomography. *SIAM review*, 41(1):85–101, 1999.

[53] BH Brown and AD Seagar. The Sheffield data collection system. *Clinical Physics and Physiological Measurement*, 8:91–97, 1987.

[54] `http://www.draeger.com/UK/en/applications/ventilation_therapy/eit`.

[55] G. Boverman, B.S. Kim, D. Isaacson, and J.C. Newell. The complete electrode model for imaging and electrode contact compensation in electrical impedance tomography. In *Engineering in Medicine and Biology Society, 2007. EMBS 2007. 29th Annual International Conference of the IEEE*, pages 3462–3465. IEEE, 2007.

[56] S. Fauser and A. Schulze-Bonhage. How large must an epileptic focus be to cause an electrographic status epilepticus–a case report. *Clinical Neurophysiology*, 115(10):2274–2279, 2004.

[57] A. Adler and W.R.B. Lionheart. Uses and abuses of EIDORS: an extensible software base for EIT. *Physiological Measurement*, 27:25–42, 2006.

[58] S.I. Goncalves, J.C. de Munck, J.P.A. Verbunt, F. Bijma, R.M. Heethaar, and F. Lopes da Silva. In vivo measurement of the brain and skull resistivities using an EIT-based method and realistic models for the head. *Biomedical Engineering, IEEE Transactions on*, 50(6):754–767, 2003.

[59] A. Adler, A. Borsic, N. Polydorides, and W.R.B. Lionheart. Simple FEMs arent́ as good as we thought: experiences developing EIDORS v3. 3. *Proc. 9th Conf. Electrical Impedance Tomography*, 2008.

[60] JL Davidson, CJD Pomfrett, and H. McCann. Predicted EIT current densities in the brain using a 3D anatomically realistic model of the head. In *13th International Conference on Electrical Bioimpedance and the 8th Conference on Electrical Impedance Tomography*, pages 376–379. Springer, 2007.

[61] A. Rowland, M. Burns, T. Hartkens, JV Hajnal, D. Rueckert, and DLG Hill. Information extraction from images (IXI): Image processing workflows using a grid enabled image database. *Proceedings of DiDaMIC*, 4:26–29, 2004.

[62] C. Ramon, P. Schimpf, J. Haueisen, M. Holmes, and A. Ishimaru. Role of soft bone, CSF and gray matter in EEG simulations. *Brain topography*, 16(4):245–248, 2004.

[63] D.W. Shattuck and R.M. Leahy. BrainSuite: An automated cortical surface identification tool. *Medical Image Analysis*, 6:129–142, 2002.

[64] C. Gabriel, S. Gabriel, and E. Corthout. The dielectric properties of biological tissues: I. Literature survey. *Physics in Medicine and Biology*, 41:2231, 1996.

[65] S. Gabriel, RW Lau, and C. Gabriel. The dielectric properties of biological tissues: II. Measurements in the frequency range 10 Hz to 20 GHz. *Physics in Medicine and Biology*, 41:2251, 1996.

[66] S. Gabriel, RW Lau, and C. Gabriel. The dielectric properties of biological tissues: III. Parametric models for the dielectric spectrum of tissues. *Physics in Medicine and Biology*, 41:2271, 1996.

[67] S. Rush and DA Driscoll. Current distribution in the brain from surface electrodes. *Anesthesia and analgesia*, 47(6):717–723, 1968.

[68] RJ Sadleir and A. Argibay. Modeling skull electrical properties. *Annals of Biomedical engineering*, 35(10):1699–1712, 2007.

[69] P.W. Nicholson. Specific impedance of cerebral white matter. *Experimental Neurology*, 13(4):386–401, 1965.

[70] P. Fillard, N. Toussaint, and X. Pennec. Medinria: DT-MRI processing and visualization software. In *Similar Tensor Workshop*, volume 5, page 7, 2006.

[71] J.F.P.J. Abascal, S.R. Arridge, D. Atkinson, R. Horesh, L. Fabrizi, M. De Lucia, L. Horesh, R.H. Bayford, and D.S. Holder. Use of anisotropic modelling in electrical impedance tomography; description of method and preliminary assessment of utility in imaging brain function in the adult human head. *Neuroimage*, 43(2):258–268, 2008.

[72] M.J.D. Cook and Z.J. Koles. A high-resolution anisotropic finite-volume head model for EEG source analysis. In *Engineering in Medicine and Biology Society, 2006. EMBS'06. 28th Annual International Conference of the IEEE*, pages 4536–4539. IEEE, 2008.

[73] W.R.B. Lionheart. EIT reconstruction algorithms: pitfalls, challenges and recent developments. *Physiological Measurement*, 25:125–142, 2004.

[74] Y. Saad. *Iterative methods for sparse linear systems*. Society for Industrial Mathematics, 2003.

[75] R.R. Harrison and C. Charles. A low-power low-noise CMOS amplifier for neural recording applications. *IEEE Journal of Solid-State Circuits*, 38(6):958–965, 2003.

[76] M. Vauhkonen, D. Vadasz, PA Karjalainen, E. Somersalo, and JP Kaipio. Tikhonov regularization and prior information in electrical impedance tomography. *Medical Imaging, IEEE Transactions on*, 17(2):285–293, 2002.

[77] M. Cheney, D. Isaacson, JC Newell, S. Simske, and J. Goble. NOSER: An algorithm for solving the inverse conductivity problem. *International Journal of Imaging Systems and Technology*, 2(2):66–75, 1990.

[78] B. Brandstatter. Jacobian calculation for electrical impedance tomography based on the reciprocity principle. *Magnetics, IEEE Transactions on*, 39(3):1309–1312, 2003.

[79] M.R. Nuwer, G. Comi, R. Emerson, A. Fuglsang-Frederiksen, J.M. Guerit, H. Hinrichs, A. Ikeda, F.J.C. Luccas, and P. Rappelsberger. IFCN standards for digital recording of clinical EEG. *Recommendations for the practice of clinical neurophysiology: guidelines of the International Federation of Clinical Neurophysiology*, page 11, 1999.

[80] A.A. Faisal, L.P.J. Selen, and D.M. Wolpert. Noise in the nervous system. *Nature Reviews Neuroscience*, 9(4):292–303, 2008.

[81] M.J. Peters, M. Hendriks, and J.G. Stinstra. The passive DC conductivity of human tissues described by cells in solution. *Bioelectrochemistry*, 53(2):155–160, 2001.

[82] NVIDIA Corporation. NVIDIA CUDA compute unified device architecture programming guide v3.2, 2010.

[83] F. Ries. *Heterogeneus Multicore Systems for Signal Processing*. PhD thesis, University of Bologna, 2011.

[84] V. Volkov and J.W. Demmel. Benchmarking GPUs to tune dense linear algebra. In *Proceedings of the 2008 ACM/IEEE conference on Supercomputing*, pages 1–11. IEEE Press, 2008.

[85] F. Ries, T. De Marco, and R. Guerrieri. Solving Large Non-Hermitian Linear Systems on Multi-GPU Accelerated Workstations. *Submitted to IEEE Transactions on Parallel and Distributed Systems (TPDS)*, 2010.

[86] F. Fregni and A. Pascual-Leone. Technology Insight: noninvasive brain stimulation in neurology-perspectives on the therapeutic potential of rTMS and tDCS. *Nature Clinical Practice Neurology*, 3(7):383–393, 2007.